Review Article

Nano Research
2023, 16(7): 8542–8569

ISSN 1998-0124 CN 11-5974/O4
https://doi.org/10.1007/s12274-022-5234-1

Recent advances in 2D semiconductor nanomaterials for photocatalytic CO_2 reduction

Tong Li[1], Hongwei Huang[1] (✉), Shuobo Wang[2] (✉), Yan Mi[3] (✉), and Yihe Zhang[1]

[1] *Beijing Key Laboratory of Materials Utilization of Nonmetallic Minerals and Solid Wastes, National Laboratory of Mineral Materials, School of Materials Science and Technology, China University of Geosciences (Beijing), Beijing 100083, China*
[2] *Goods and Material Department of CASIC Tertiary Research Institute, China Aerospace Science and Industrial Corporation, Beijing 100074, China*
[3] *Key Laboratory of Chemistry and Engineering of Forest Products, State Ethnic Affairs Commission, Guangxi Key Laboratory of Chemistry and Engineering of Forest Products, Guangxi Collaborative Innovation Center for Chemistry and Engineering of Forest Products, Guangxi Minzu University, Nanning 530006, China*

Received: 12 August 2022 / **Revised:** 16 October 2022 / **Accepted:** 22 October 2022

ABSTRACT

For decades, global warming and energy shortages have been two urgent problems in human society. The solar-driven photocatalytic conversion of carbon dioxide (CO_2) into hydrocarbon fuels is expected to become a technology to solve these problems. Two-dimensional (2D) materials shine in the field of photocatalytic CO_2 due to their layered structure, larger specific surface area, more active sites, and larger charge transfer efficiency. This article reviews the progress of CO_2 reduction by several types of 2D materials in recent years. Generally, the reduction of CO_2 is difficult in terms of kinetics and thermodynamics, but it is found through theoretical calculations and experiments that 2D materials have certain advantages in the reduction of CO_2. Then the preparation methods of 2D materials are summarized and a variety of 2D materials are discussed and classified. Finally, an outlook on the development trend of 2D materials is made. This review aims to provide systematic and concise guidance for the design of 2D nanomaterials for photocatalytic CO_2 reduction.

KEYWORDS

two-dimensional (2D) materials, photocatalysis, CO_2 reduction, charge separation, reactive sites

1 Introduction

In recent decades, ultraviolet (UV) rays on the surface of the earth have increased by about 30%, which has caused global warming and the rise in sea level resulting from the melting of glaciers [1]. Studies have shown that this phenomenon is caused by excessive CO_2 in the atmosphere, leading to the greenhouse effect and severely disrupting the balance between carbon input and output [2]. As we all know, CO_2 is mainly produced by burning fossil fuels such as coal, oil, and natural gas. In addition, the rapid development of the current society has led to a gradual increase in human dependence on fossil fuels [3]. Therefore, how to reduce the content of CO_2 in the atmosphere is a major problem that we are facing. Fossil fuel is still the most used energy in the world today, and it is not realistic to replace it with new energy sources (wind energy, geothermal energy, tidal energy, etc.) at once. Inspired by the photosynthesis of plants, photocatalytic technology can convert CO_2 into hydrocarbon fuel by exposure to light [4], which is one of the most promising methods to relieve the pressure of the energy crisis and reduce the impact of the greenhouse effect due to its environmental friendliness, mild reaction conditions, and low cost. After decades of development by researchers, the conversion of CO_2 into CO and hydrocarbon fuels (CH_4, CH_3OH, HCHO, HCOOH, etc.) by photocatalysis is becoming a research hotspot [5–8].

CO_2 is an extremely stable molecule thermodynamically due to its linear molecular structure. The energy of the C=O double bond is about 750 kJ·mol^{-1}, which is more than twice that of the ordinary C–C single bond (336 kJ·mol^{-1}). Herein, considerable energy is needed to break the C=O bond and form a new C–H bond when CO_2 reduction to fuels occurs via photocatalytic reaction [9]. Semiconductor photocatalytic CO_2 reduction usually involves three steps: (1) Photocatalyst with a suitable band gap is exposed to light to generate electron–hole pairs, and the photo-generated electrons are excited to transfer to the conduction band (CB) of the semiconductor, and simultaneously the photo-generated holes are left in the valence band (VB); (2) the photo-generated electron–hole pairs separate in the bulk and migrate to the surface of the photocatalyst; and (3) the electrons on the surface of photocatalyst participate in CO_2 reduction reaction to produce value-added chemical fuels, and the electrons reduce H^+ in water into H_2 called the hydrogen evolution reaction (HER) [10]. Among the three steps, steps (1) and (2) have been intensively studied in the past decades, and step (3) has been increasingly emphasized recently. A variety of intermediates can be generated in step (3), which is decided by the surface state and redox abilities of the photocatalyst. According to the reducing ability of photocatalysts, final products include CH_4, CO, CH_3OH, C_2H_5OH, etc. [11]. However, when CO_2 is reduced by photocatalysts, the HER needs photoelectrons to occur. Due to the

Address correspondence to Hongwei Huang, hhw@cugb.edu.cn; Shuobo Wang, shuobowang@hotmail.com; Yan Mi, miyan@gxmzu.edu.cn

strong competition, it affects the selectivity and efficiency of CO_2 reduction. Therefore, it is necessary to suppress the competitive reaction of HER while enhancing the activity of CO_2 reduction, which is difficult especially in reaction kinetics and thermodynamics [12].

During the photocatalytic reduction of CO_2, the adsorption of CO_2 molecules on the surface of the photocatalyst is vitally important to the selectivity of reaction products. The adsorption and activation processes are critical to the subsequent reduction steps and the suppression of competitive HER. When CO_2 is adsorbed on the surface, these CO_2 molecules can be activated by photoelectrons to generate various intermediates and then converted into different final products. Generally, there are three kinds of CO_2 adsorption modes on the surface of the photocatalyst. (1) CO_2 gets electrons to form the first structure (Fig. 1(a)) [13], due to the repulsion between the two lone electron pairs on the oxygen atom and the unpaired electron on the carbon atom, and (2) CO_2 can act as an electron acceptor to form the second structure (Fig. 1(b)). In addition, (3) CO_2 serves as both an electron donor and acceptor (Fig. 1(c)). Because the adsorbing process tends to bend this linear CO_2 in its geometric shape, the CO_2 molecule no longer keeps linear symmetry and the reaction barrier will decrease [13]. The redox potentials of various final products were summarized in Table 1. However, two-dimensional (2D) materials exhibit stronger adsorption of CO_2 due to their larger specific surface area and more active sites. For instance, ultrathin graphitic carbon nitride (g-C_3N_4) exhibits strong CO_2 adsorption due to its higher specific surface area and porosity than bulk-phase g-C_3N_4, and this strong adsorption increases the photoreduction activity of CO_2 in ultrathin g-C_3N_4 nanosheets (NSs) by about ten times [14]. Furthermore, Zou et al. reported that the 2D covalent organic frameworks (COF) nanosheets have effective CO_2 adsorption characteristics [15].

There are two proposed mechanisms for the photocatalytic reduction of CO_2. The first one is the single-electron transfer to form $CO_2^{\cdot-}$, but this process requires a very negative reduction potential (−1.9 V versus normal hydrogen electrode (NHE)), so the single electron transfer mechanism is executed thermodynamically tougher [16]. The second one is proton-assisted multi-electrons transfer. When electrons and protons are transferred to CO_2 simultaneously, the reaction barrier of the reduction process can be reduced, and thus this process is feasible in both kinetics and thermodynamics [11]. Two reduction pathways of CO_2 are generally recognized, namely the formaldehyde pathway (rapid hydrogenation pathway) and the carbene pathway (rapid deoxygenation pathway) (Fig. 2). The methane generation in the formaldehyde pathway is characterized by simultaneous deoxygenation and hydrogenation reactions. The route is roughly $CO_2^{\cdot-} \rightarrow HCOOH \rightarrow HCHO \rightarrow CH_3OH \rightarrow CH_4$.

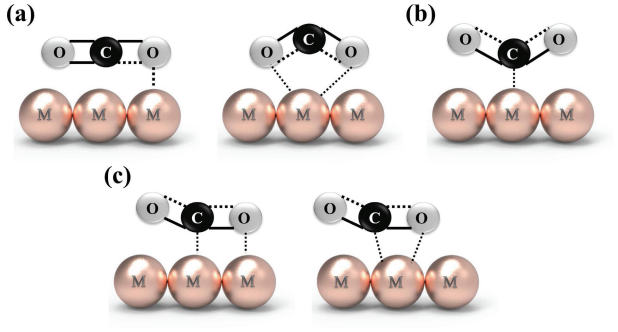

Figure 1 Different CO_2 adsorption modes on the surface of photocatalysts: (a) oxygen coordination; (b) carbon coordination; and (c) mixed coordination. Reproduced with permission from Ref. [13], © The Royal Society of Chemistry 2016.

Table 1 Photocatalytic CO_2 reduction into different products and corresponding redox potentials (vs. NHE at pH 7)

Product	Reaction	E^0 redox (V vs. NHE)
Carbon monoxide	$CO_2 + 2H^+ + 2e^- \rightarrow CO + H_2O$	−0.53
Formic acid	$CO_2 + 2H^+ + 2e^- \rightarrow HCOOH$	−0.61
Formaldehyde	$CO_2 + 4H^+ + 4e^- \rightarrow HCHO + H_2O$	−0.48
Methanol	$CO_2 + 6H^+ + 6e^- \rightarrow CH_3OH + H_2O$	−0.38
Methane	$CO_2 + 8H^+ + 8e^- \rightarrow CH_4 + 2H_2O$	−0.24
Acetaldehyde	$2CO_2 + 10H^+ + 10e^- \rightarrow CH_3CHO + 3H_2O$	−0.36
Ethylene	$2CO_2 + 12H^+ + 12e^- \rightarrow C_2H_4 + 4H_2O$	−0.34
Ethanol	$2CO_2 + 12H^+ + 12e^- \rightarrow C_2H_5OH + 3H_2O$	−0.33
Ethane	$2CO_2 + 14H^+ + 14e^- \rightarrow C_2H_6 + 4H_2O$	−0.27
Oxygen	$H_2O \rightarrow 1/2O_2 + 2H^+ + 2e^-$	+0.81
Hydrogen	$2H^+ + 2e^- \rightarrow H_2$	−0.42

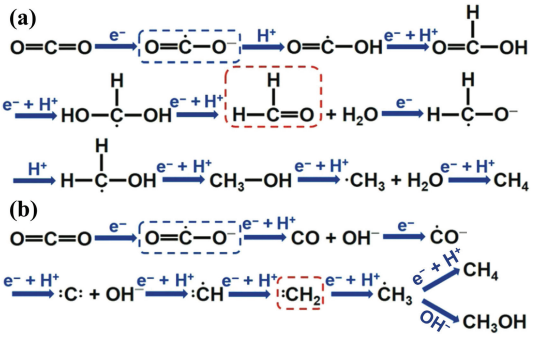

Figure 2 Two proposed mechanisms for the reduction of CO_2 to methane: formaldehyde and carbene pathways. Reproduced with permission from Ref. [17], © The Royal Society of Chemistry 2020.

The carbene pathway follows the route $CO_2^{\cdot-} \rightarrow CO \rightarrow C\cdot \rightarrow CH_3\cdot \rightarrow CH_3OH/CH_4$, which is characterized by first deoxygenation reaction and then hydrogenation reaction. However, the current research on the mechanism of CO_2 reduction is still not very thorough.

Since Inoue [18] first discovered in 1979 that CO_2 can be converted into CH_3OH and CH_2O by photocatalysis, many photocatalytic materials have been investigated for CO_2 conversions, such as metal oxides, metal sulfides, graphene oxide (GO), graphite-like phase carbon nitrides, transition metal disulfides, layered double hydrides, and layered Bi-based compounds. However, most semiconductor photocatalysts still suffer the problems of poor selectivity and low efficiency. In addition, the recombination of photo-generated electrons and holes seriously reduces the efficiency of charge separation, and the small specific surface area lacks enough active sites to effectively adsorb CO_2 on the surface of the photocatalyst, resulting in poor reaction activity and selectivity. Remarkably, the 2D ultrathin materials not only provide plenty of active sites due to their open and largely exposed surface but also shorten the diffusion path of charge carriers. Thus, 2D materials provide new opportunities and hopes for photocatalytic CO_2 reduction.

2 Properties and preparation of 2D photocatalytic nanomaterials

2.1 Advantages and properties of 2D materials

Compared with other structures, the 2D nanosheet structure has many advantageous characteristics. (1) 2D nanosheets have a

larger specific surface area, which provides more active sites for CO_2 adsorption and activation; (2) due to the thin layer property of nanosheets, the migration distance of photo-generated carriers is reduced; (3) 2D nanosheets have a high proportion of exposed atoms on the surface, which are easy to form vacancies or defects. The suitable vacancies and defects can trap electrons and facilitate the reduction of CO_2; and (4) the surface of nanosheets has unsaturated atoms and dangling bonds that can be compounded with other photocatalysts to ameliorate the reaction activity of materials.

For example, Yue et al. successfully fabricated 2D/2D $BiVO_4$/$CsPbBr_3$ S-scheme heterojunction via *in situ* growth approach. An intimate heterointerface between $BiVO_4$ and $CsPbBr_3$ was obtained, largely boosting charge transfer across the interfacial. And the author further introduced the oxygen vacancy into $BiVO_4$, yielding an enhanced interfacial electric field over $BiVO_4$ and $CsPbBr_3$ heterojunction. Hence, the CO yield of optimal sample reaches as high as 103.5 μmol·g^{-1} under visible light irradiationa [19]. Moreover, Xue et al. exploited an atomically thin $Li_{1.81}H_{0.19}Ti_2O_5{\cdot}2H_2O$ (LHTO) nanosheets for selective photocatalytic CO_2 reduction to CO with a selectivity of 93%. The high reaction activity benefited from more sites for CO_2 adsorption and faster photoelectrons transfer rate for atomically ultrathin 2D structure [20]. In addition, Li et al. synthesized orthorhombic regular Bi_4TaO_8Cl square nanoplates, which had exposed {001} crystal facets for promoting the reduction reaction. The dominantly exposed {001} crystal facets allowed more active surfaces and inhibited charge recombination [21]. Besides, our group developed a series $Bi_2O_2(NO_3)(OH)$/g-C_3N_4 (BON/CN) Z-scheme junction, and the optimal samples exhibited a CO evolution rate of 14.84 μmol·g^{-1}·h^{-1}, which was about 15 and 3.5 times higher than pure BON and CN, respectively. The face-to-face contact between BON nanosheet and CN nanosheet resulted in faster carrier transport and a higher rate of interfacical charge separation [22]. Likewise, our group also prepared $Sr_2Bi_2Nb_2TiO_{12}$ nanosheets and introduced oxygen vacancies (OVs). Compared with the bulk sample, the photocatalytic CO_2 reduction performance of $Sr_2Bi_2Nb_2TiO_{12}$ nanosheets with moderate OVs was enhanced by 58 times [23]. In summary, the photocatalysts with 2D structure show remarkable electronic and optical properties, boding for the great prospects of advanced technology applications, and thus receiving more and more attention in recent years [24].

2.2 Preparation of 2D photocatalytic nanomaterials

For 2D photocatalytic nanomaterials, their preparation methods can be roughly divided into top-down and bottom-up routes (Fig. 3), which are summarized in Table 2.

2.2.1 *Top-down method*

For top-down route, mechanical or chemical methods are used to weaken or break the force between the layers in bulk material, such as micromechanical peeling and liquid phase peeling, to obtain a 2D nanosheet or nanoplate structure [25–27]. Among them, the most commonly used is micromechanical peeling. In 2004, Novoselov and Geim [28] used a tape to destroy the weak van der Waals force between the massive graphite to obtain a single layer of graphene. The discovery of graphene also provided a new hotspot material that could be applied to a variety of fields. However, the mechanical peeling method is not suitable for the production of large-size materials and industrial-scale production. In contrast, liquid phase peeling can realize mass production. After treating the bulk material with surfactant or ultrasonication, the 2D nanomaterial can be obtained by destroying the interlayer forces. For instance, Michael Naguib et al. reported the preparation of 2D MXene nanosheet, composed of Ti_3C_2 layers, by the room temperature exfoliation of Ti_3AlC_2 in hydrofluoric acid [29]. Moreover, Zhang et al. prepared ReS_2 nanosheets by stripping commercial bulk ReS_2 via ultrasonication in deionized (DI) water and further obtained ReS_2/CdS heterostructure composite by self-assembly. The as-prepared sample exhibited significantly boosted CO_2 reduction [30]. However, the biggest drawback of the top-down method is that it cannot precisely control the growth direction and dimensions of the material, which also restricts its applications.

2.2.2 *Bottom-up method*

Bottom-up method includes chemical vapor deposition (CVD), wet chemical synthesis [31], hydrothermal methods [32], solvothermal methods, self-assembly [33], molecular beam epitaxy, and so on. The wet chemical method refers to a method in which the precursor chemically reacts to produce a product in a liquid phase environment, and its operation is simple and can be produced on a large scale. CVD [34] is a method of forming a thin film by chemically reacting with one or more gas-phase elements or compounds on the surface of the substrate, which can be used to deposit metals, carbides, nitrides, oxides, borides, etc. Most of the products have good crystallinity, high purity, and high yield. In theory, almost all 2D materials can be prepared by a bottom-up method. For example, Anne Meier et al. used the CVD method to successfully synthesize the MoS_2 nanoflower composed of nanosheets [35]. Sangbaek Park et al. successfully synthesized 2D

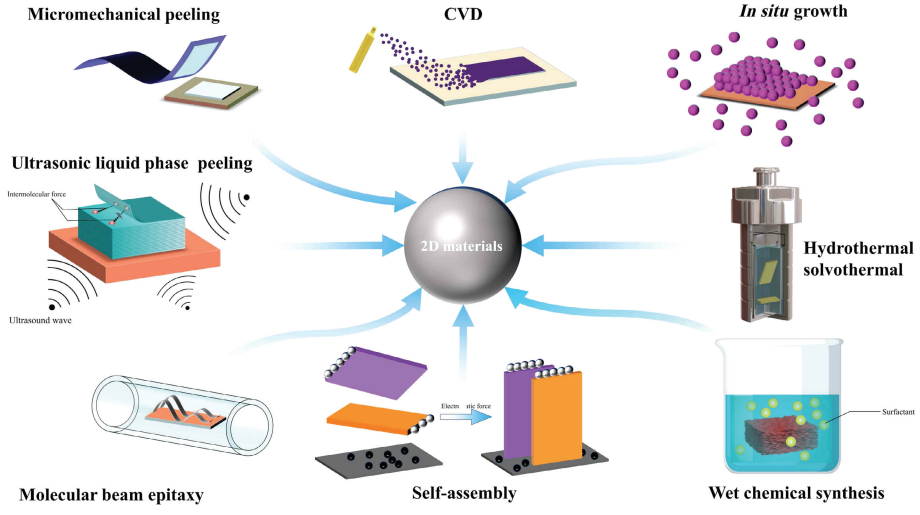

Figure 3 Schematic illustration for the synthesis of different 2D materials.

Table 2 The synthesis methods of the 2D photocatalyst

Synthesis	Process	Materials	Advantage and disadvantage
Micromechanical peeling	Using scotch tape to destroy the van der Waals force between crystal layers to obtain sheet material.	Graphene [28]	High-purity crystalline materials can be prepared, but the thickness of the product cannot be controlled.
Ultrasonic liquid phase peeling	The shear stress generated by the energy provided by the ultrasonic wave separates the material.	WSe_2-graphen [37] Black phosphorus [38]	Simple operation and low cost, but low stripping efficiency.
CVD	Method for synthesizing coating or nanomaterial by chemical gas or steam reacting on a substrate surface.	MoS_2 [35]	Highly crystalline and high-purity materials can be prepared, and the synthetic material scale is controllable.
Wet chemical	Method for preparing material by surface-active agent-assisted liquid phase reaction.	Ag/2H-MoS_2 [39]	The synthesis process is simple and easy to operate, the yield is high, and other substances can be added for modification during the reaction process. However, the controllability of the reaction is poor, and it is difficult to obtain a uniform single-layer nanosheet.
Hydrothermal/solvothermal	In a closed container or autoclave, the reaction is carried out with water or other solvents as the medium.	CoAl-LDHs [40] La-doped BiOBr nanosheet [41]	High yield and low cost, but high temperature and high-pressure operation are more dangerous and the product is easy to agglomerate.
Self-assembly	Nanocrystals spontaneously organize or aggregate to form 2D materials under the interaction of non-covalent bonds.	g-C_3N_4/LDH [42] Bi_2WO_6/BiOI [43]	The reaction process is mild, stable, and orderly, but the obtained material size is small.
Molecular beam epitaxy	A method of growing thin films layer by layer along the crystal axis of the substrate material under appropriate substrates and conditions.	Zinc silicate nanosheets [44]	The film composition and doping concentration can be adjusted quickly with the change of the source, but the film growth rate is slow and it is difficult to commercialize production.
In situ growth	The spontaneous phase (also the second phase) in the reaction process to prepare 2D materials.	Cu_2O-loaded Zn-Cr LDHs [45] BiOBr/pCN [46]	The process is simple and the cost is low, but the response is not very controllable.

ultrathin $Ba_5Nb_4O_{15}$ nanosheets with an average thickness of ~ 6 nm via the hydrothermal method [36]. And our group reported a $Bi_2O_2(OH)(NO_3)$ (BON) nanosheet and *in situ* grafting of halogen ions (Cl^-, Br^-, and I^-) via a simple hydrothermal method. The atomic force microscopy (AFM) image revealed that the as-prepared sample was layered with a single nanosheet thickness of only 3.5 nm [47]. Furthermore, Yasuo Izumi et al. prepared $[Zn_3Ga(OH)_8]_2CO_3{\cdot}mH_2O$ layered double hydroxide ($Zn_3Ga|CO_3$ LDH) by self-assembly method and loading Ag or Au nanoparticles on LDHs via the ion-exchange method. Under irradiation by UV–visible (UV–vis) light, Au-$Zn_3Ga|CO_3$ LDH showed the best performance for CO_2 reduction for CO production (231 nmol·g^{-1}·h^{-1}) [48].

3 2D semiconductor materials for photocatalytic CO_2 reduction

In recent research, there are so many types of 2D photocatalysts that have been applied to conversion CO_2. And according to the composition and type of crystal structure, they can be divided into layered Bi-based materials, 2D layered perovskites, transition metal chalcogenide (TMDs), LDH, and other types of 2D materials (MXene, black phosphorus (BP), and COF). Under solar irradiation, CO_2 is converted into high-value-added hydrocarbon products such as CO, CH_4, CH_3OH, C_2H_4, and CHOH, mainly in the gas–solid reaction system or liquid phase reaction system. The above 2D materials will be described in detail in the following (Table 3).

3.1 Layered Bi-based photocatalysts

Layered Bi-based photocatalysts have a layered structure composed of $[Bi_2O_2]^{2+}$ slices and staggered anions or anionic groups. Due to the unique layered crystal structures and diverse compositions, they are widely studied in photocatalytic reactions. In general, layered Bi-based photocatalysts include Sillén-structured BiOX (X = Cl, Br, and I), bismuth-rich Sillén-structured $Bi_xO_yX_z$, Aurivillius-structured Bi_2WO_6, Bi_2MoO_6 (MBO), $Bi_4Ti_3O_{12}$, and others ($BiOIO_3$, Sillén-related structured $Bi_2O_2(OH)(NO_3)$, etc.).

3.1.1 *Bismuth oxyhalides (BiOX, X = Cl, Br, and I)*

The crystal structure of BiOX is PbFCl type and belongs to the tetragonal crystal system. For instance, the crystal structure of BiOCl is formed by stacking $[Bi_2O_2]^{2+}$ units and double Cl atom layers in the [001] axis direction [49] (Fig. 4(a)). The BiOX layer has a strong covalent bonding within the $[Bi_2O_2]^{2+}$ slices and the weak van der Waals force between these layers [50]. In each [X-Bi-O-Bi-X] layer, one bismuth atom is surrounded by four oxygen atoms and four halogen atoms, resulting in an asymmetric structure [51]. Such interwoven anisotropic structure and asymmetric center of BiOX cause a strong built-in electric field, which thereby effectively separates the photo-generated electron–hole pairs for high photocatalytic performance. Bismuth oxyhalides have an eye-catching development trend in the field of photocatalytic reduction of CO_2 in recent years, such as BiOCl [52] (band gap about 3.22 eV), BiOBr [53] (band gap about 2.64 eV), and BiOI [54] (band gap about 1.77 eV).

Crystal facet control and surface defect construction are commonly used for the modification of BiOX. Jin et al. used a controlled injection technique to prepare BiOCl nanosheets with different exposing percentages of {001} facets, and found that the photocatalytic CO_2 conversion performance increased (the yield of CH_4 reached 41.48 μmol·g^{-1} within 8 h) as the thickness of the nanosheets decreased and the exposed surface increased, which was attributed to the good dispersibility and crystallinity of BiOCl nanosheets, large specific surface area, and highly exposed {001} facets [55]. To further improve the photocatalytic activity of BiOCl nanosheets, Wu et al. deposited bismuth metal on OVs-rich BiOCl nanosheets for CO_2 photoreduction [56]. Bi/BiOCl with rich OVs exhibited better photocatalytic activity than single BiOCl nanosheets and nanodisks. From the result of the fluorescence spectrum, the charge recombination of BiOCl nanosheets was

Table 3 Summary of 2D photocatalysts for CO_2 photoreduction

	Photocatalyst	Synthesis method	Light source	Mass (mg)	Reaction system solvent	Product	Yield	Sacrificial agent or photosensitizer	References
Layered Bi-based photocatalysts	Thickness-tunable BiOCl nanosheets	Facial hot-injection	300 W Xe lamp (250 nm < λ < 380 nm)	20	Liquid phase 30 mL H_2O	CH_4	5.18 μmol·g^{-1}·h^{-1}	—	[55]
	Bi/BiOCl nanosheets	Hydrothermal	300 W Xe lamp	20	Gas–solid phase	CO CH_4 H_2	4.75 μmol·g^{-1}·h^{-1} 0.45 μmol·g^{-1}·h^{-1} 0.23 μmol·g^{-1}·h^{-1}	—	[56]
	OV-BiOCl nanosheets	Solvothermal	300 W Xe lamp	50	Gas–solid phase	CO	8.75 μmol·g^{-1}·h^{-1}	—	[52]
	Bi_3O_4Cl/g-C_3N_4	Physical mixture in ethanol at room temperature	300 W Xe lamp	50	Liquid phase 5 mL H_2O	CO CH_4	6.60 μmol·g^{-1}·h^{-1} 1.90 μmol·g^{-1}·h^{-1}	—	[60]
	CPDs/$Bi_{12}O_{17}Cl_2$ nanosheets	Mechanical stirring	300 W Xe lamp (λ > 400 nm)	30	Liquid phase 1 mL H_2O	CO	3.21 μmol·g^{-1}·h^{-1}	—	[62]
	Ultrathin OV-BiOBr nanosheets	Solvothermal	300 W Xe lamp (λ > 400 nm)	—	Gas–solid phase	CH_4	4.86 μmol·g^{-1}·h^{-1}	—	[53]
	OV-BiOBr nanosheets	Hydrothermal	500W Xe lamp (λ > 400 nm)	30	Gas–solid phase	CH_4	2.15 μmol·g^{-1}·h^{-1}	—	[57]
	V_{Bi}-BiOBr nanosheets	Long carbon chain ionic liquid assisted synthesis at room temperature	300 W Xe lamp	30	Liquid phase 50 mL H_2O	CO	20.10 μmol·g^{-1}·h^{-1}	—	[58]
	Gd^{3+} decorated BiOBr	Hydrothermal	300 W Xe lamp (λ > 420 nm)	100	Liquid phase 60 mL H_2O	CH_3OH	41.23 μmol·g^{-1}·h^{-1}	—	[59]
	La-doped BiOBr nanosheets	Hydrothermal	300 W Xe lamp (λ > 420 nm)	100	Liquid phase 60ml H_2O	CH_3OH	22.77 μmol·g^{-1}·h^{-1}	—	[41]
	Ultrathin $Bi_4O_5Br_2$ nanosheets	Hydrothermal and hydrolytic	300 W Xe lamp	150	Gas–solid phase	CO CH_4	2.73 μmol·g^{-1}·h^{-1} 2.04 μmol·g^{-1}·h^{-1}	—	[85]
	Co-Bi_3O_4Br atomic layer	Hydrothermal	300 W Xe lamp	30	Liquid phase 50 mL H_2O	CO	107.10 μmol·g^{-1}·h^{-1}	—	[64]
	BiOI nanosheets	Hydrothermal	300 W Xe lamp	50	Gas–solid phase	CO CH_4	0.26 μmol·g^{-1}·h^{-1} 0.089 μmol·g^{-1}·h^{-1}	—	[54]
	Bi_2WO_6/BiOI	Self-assembly	500 W Xe lamp (λ < 400 nm)	—	Gas–solid phase	CH_4	18.32 μmol·g^{-1}	—	[43]
	Bi/$Bi_4O_5I_2$ composite	Molecular precursor hydrolytic	300 W Xe lamp	50	Gas–solid phase	CO CH_4	40.02 μmol·g^{-1}·h^{-1} 7.19 μmol·g^{-1}·h^{-1}	—	[66]
	Ultrathin Bi_2WO_6 nanosheets	*In situ* topotactic transformation	300 W Xe lamp (λ > 400 nm)	—	Gas–solid phase	CH_4	1.00 μmol·g^{-1}·h^{-1}	—	[69]
	Ultrathin C-doped Bi_2WO_6 nanosheet	Hydrothermal	300 W Xe lamp	100	Gas–solid phase	CH_3OH C_2H_5OH	1.15 μmol·g^{-1}·h^{-1} 0.65 μmol·g^{-1}·h^{-1}	—	[71]
	Chloride modified Bi_2WO_6 nanosheets	Hydrothermal	300 W Xe lamp	20	Gas–solid phase	CH_4	4.97 μmol·g^{-1}	—	[72]
	2D/2D $CsPbBr_3$/Bi_2WO_6	Self-assembly	150 W Xe lamp	5	Liquid phase 8 mL ethyl acetate	CO CH_4	527.30 μmol·g^{-1}·h^{-1}	2 mL isopropyl alcohol	[73]
	Bi_2MoO_6 nanosheets	Hydrothermal	300 W Xe lamp	10	Gas–solid phase	CO	14.38 μmol·g^{-1}·h^{-1}	—	[75]
	Layered $BiOIO_3$ single crystals	Hydrothermal	300 W Xe lamp	50	Gas–solid phase	CO	5.42 μmol·g^{-1}·h^{-1}	—	[80]
	OV-$BiOIO_3$ single crystals	Hydrothermal	300 W Xe lamp	20	Gas–solid phase	CO	17.33 μmol·g^{-1}·h^{-1}	—	[81]
	Ultrathin OV-$Bi_4Ti_3O_{12}$ nanosheets	Combined hydrothermal and postreduction process	300 W Xe lamp	20	Gas–solid phase	CO	11.70 μmol·g^{-1}·h^{-1}	—	[76]
	Corona poling and I-grafting $Bi_4Ti_3O_{12}$	Hydrothermal	300 W Xe lamp	20	Gas–solid phase	CO	15.10 μmol·g^{-1}·h^{-1}	—	[77]
	$BiVO_4$/$Bi_4Ti_3O_{12}$ heterojunction	*In situ* hydrothermal	300 W Xe lamp	10	Gas–solid phase	CH_3OH CO	16.60 μmol·g^{-1}·h^{-1} 13.29 μmol·g^{-1}·h^{-1}	—	[78]

(Continued)

	Photocatalyst	Synthesis method	Light source	Mass (mg)	Reaction system solvent	Product	Yield	Sacrificial agent or photosensitizer	References
Layered Bi-based photocatalysts	2D/2D Bi_4NbO_8Cl/g-C_3N_4 heterojunction	High-energy ball-milling	300 W Xe lamp	50	Gas–solid phase	CO	2.26 μmol·g^{-1}·h^{-1}	—	[84]
	g-C_3N_4/$Bi_2O_2[BO_2(OH)]$	High-energy ball milling	300 W Xe lamp	20	Gas–solid phase	CO	6.09 μmol·g^{-1}·h^{-1}	—	[83]
	Surface halogen ions decorated $Bi_2O_2(OH)(NO_3)$ nanosheet	Hydrothermal	300 W Xe lamp	10	Gas–solid phase	CO	8.12 μmol·g^{-1}·h^{-1}	—	[47]
	Z-scheme $Bi_2O_2(NO_3)(OH)$/g-C_3N_4	Self-assembly	300 W Xe lamp	20	Gas–solid phase	CO	14.84 μmol·g^{-1}·h^{-1}	—	[22]
	Z-scheme g-C_3N_4/$BiVO_4$ ultrathin nanosheets	Hydrothermal	300 W Xe lamp	80	Gas–solid phase	CH_4 CO	4.57 μmol·g^{-1}·h^{-1} 5.19 μmol·g^{-1}·h^{-1}	—	[86]
	$(Bi_6O_{(4+x)}(OH)_{(4-x)}(NO_3)_{(6-x)})\cdot nH_2O$ (x = 0–2, n = 0–3) and niobium pentoxide nanocomposites	Hydrothermal	TUV Philips 18 W mercury lamp, 254 nm	10	Gas–solid phase	CO C_2H_4	2.80 μmol·g^{-1}·h^{-1} 0.10 μmol·g^{-1}·h^{-1}	—	[87]
	Ultrathin Bi_2O_3 nanosheet/Bi_2WO_6 network heterostructure	Covalently bonded epitaxial growth	300 W Xe lamp (λ > 400 nm)	50	Gas–solid phase	CO	17.39 μmol·g^{-1}·h^{-1}	—	[88]
	Z-scheme $Bi_2O_2CO_3$/Bi/NiAl-LDH nanosheet	Hydrothermal	300 W Xe lamp (λ > 400 nm)	50	Gas–solid phase	CH_4	56.64 μmol·g^{-1}	—	[89]
	OV-Bi_2WO_6 ultrathin nanosheets	Hydrothermal	300 W Xe lamp	10	Liquid phase 4 mL DI water 6 mL CH_3CN	CO	40.60 μmol·g^{-1}·h^{-1}	2 mL TEOA	[70]
	Z-scheme $Bi_4TaO_8Cl/W_{18}O_{49}$	Self-assembly	Hayashi UV410 (λ < 780 nm)	20	Gas–solid phase	CO	19.60 μmol·g^{-1}·h^{-1}	—	[90]
	CQDs/Bi_2WO_6 nanosheet	Hydrothermal	500 W Xe lamp (λ > 400 nm)	—	Gas–solid phase	CH_4	7.19 μmol·g^{-1}	—	[91]
	Undoped layered $Li_2LaTa_2O_6N$	Precursor decomposition	High-pressure mercury lamp (λ > 400 nm)	—	Liquid phase	HCOOH	97% selectivity	Binuclear Ru(II) complex	[92]
	OV-$Sr_2Bi_2Nb_2TiO_{12}$	Softchemical	300 W Xe lamp	50	Gas–solid phase	CO	17.11 μmol·g^{-1}·h^{-1}	—	[23]
	$CoTiO_3$/g-C_3N_4	*In situ* growth	300 W Xe lamp	30	Liquid phase	CO H_2	263.2 μmol·g^{-1}·h^{-1} 75.2 μmol·g^{-1}·h^{-1}	2 mL TEOA 5 mg $[Ru(bpy)_3]Cl_2\cdot 6H_2O$	[93]
Layered perovskite	2D/2D WO_3/$LaTiO_2N$	Hydrothermal	300 W Xe lamp	10	Gas–solid phase	CO CH_4	2.21 μmol·g^{-1}·h^{-1} 0.36 μmol·g^{-1}·h^{-1}	—	[94]
	$SrBi_4Ti_4O_{15}$ nanosheet	Softchemical	300 W Xe lamp	100	Gas–solid phase	CH_4	19.80 μmol·g^{-1}·h^{-1}	—	[95]
	layered Sr_2TiO_4	Sol-gel	6 W UV-lamp	10	Gas–solid phase	CH_4	3431.77 μmol·g^{-1}	—	[96]
	Ag/$H_2SrTa_2O_7$ layered perovskite	Polymerizable complex and ion-exchange	300 W Xe lamp (λ > 200 nm)	300	Gas–solid phase	CO	60.9% selectivity	—	[97]
	Cu/Pt-$HCa_2Ta_3O_{10}$ perovskite nanosheets	Ion exchange	150 W Xe lamp	—	Gas–solid phase	CH_3OH C_2H_5OH	7.40 μmol·g^{-1}·h^{-1} 113.20 μmol·g^{-1}·h^{-1}	—	[98]
	Bi selectively doped $SrTiO_{3-x}$ nanosheets	Hydrothermal	300 W Xe lamp (λ > 420 nm)	50	Gas–solid phase	CO CH_4	5.58 μmol·g^{-1}·h^{-1} 0.36 μmol·g^{-1}·h^{-1}	—	[99]
	Ag/2H-MoS_2	Wet chemistry	250 W high-pressure mercury lamp	20	Liquid phase	CH_3OH	365.08 μmol·g^{-1}·h^{-1}	20 mL isopropanol	[100]
TMDs	2D/1D MoS_2/TiO_2	Hydrothermal	350 W Xe lamp	50	Gas–solid phase	CH_4	2.86 μmol·g^{-1}·h^{-1}	—	[101]
	2D/2D MoS_2/TiO_2	Hydrothermal	300 W Xe lamp	50	Liquid phase 100 mL DI water	CO CH_4	268.97 μmol·g^{-1} 49.93 μmol·g^{-1}	—	[102]
	h-BN/MoS_2 heterostructure	Hydrothermal	20 W white LED	100	Liquid phase	CH_3OH	5994 μmol·g^{-1}	TEA	[103]
	$CsPbBr_3$/MoS_2 heterostructures	Self-assembly	300 W Xe lamp	5	Liquid phase 5 mL ethylcetate 20 μL DI water	CO CH_4	25.00 μmol·g^{-1}·h^{-1} 12.80 μmol·g^{-1}·h^{-1}	—	[104]

(Continued)

	Photocatalyst	Synthesis method	Light source	Mass (mg)	Reaction system solvent	Product	Yield	Sacrificial agent or photosensitizer	References
	α-Fe_2O_3/MoS_2 composite	*In situ* growth	300 W Xe lamp (λ > 420 nm)	50	Liquid phase 15 mL DI water	CH_4 CH_3OH	121 μmol·g^{-1}·h^{-1} 41μmol·g^{-1}·h^{-1}	—	[105]
	C-doped SnS_2 nanosheet	Hydrothermal	300 W Xe lamp	50	Gas–solid phase	CH_3CHO	125.66 μmol·g^{-1}	—	[106]
	2D/2D SnS_2/TiO_2	Hydrothermal	300 W Xe lamp	100	Liquid phase 2 mL water	CH_4	23 μmol·g^{-1}	—	[107]
	Cs_2SnI_6 nanocrystal/SnS_2 nanosheet heterojunction	Stirring at room temperature	λ > 400 nm	—	Liquid phase 5 μL water	CH_4	6.09 μmol·g^{-1}	5 μL CH_3OH	[108]
	SnS_2/Au/g-C_3N_4 embedded structure	Hydrothermal	300 W Xe lamp	20	Liquid phase 100 mL water	CO CH_4	93.81 μmol·g^{-1}·h^{-1} 74.98 μmol·g^{-1}·h^{-1}	TEOA	[109]
TMDs	2D MoS_2 nanoflowers	CVD	400 nm < λ < 700 nm	150	Liquid phase 100 μL water	CO	-	—	[35]
	SnS_2 nanosheets	Hydrothermal	300 W Xe lamp (λ > 420 nm)	100	Liquid phase 100 mL water	CH_4	97.50 μmol·g^{-1}	—	[110]
	SnS_2	Hydrothermal	500 W Xe lamp	50	Gas–solid phase	CO	200 ppm	—	[111]
	CoAl-LDH/MoS_2 nanocomposite	Self-assembly	300 W Xe lamp (λ > 400 nm)	30	Liquid phase 2 mL water 6 mL CH_3CN	H_2:CO	9:1	2 mL TEOA 3.3 mg $[Ru(bpy)_3]Cl_2$·$6H_2O$	[112]
	MoS_2/MoO_{3-x} heterostructure	*In situ* partial oxidation	500 W Xe lamp	2	Gas–solid phase	CO	32.40 μmol·g^{-1}·h^{-1}	—	[113]
	ReS_2/CdS nanosheets	*In situ* growth	300 W Xe lamp (λ > 420 nm)	50	Gas–solid phase	CO	7.10 μmol·g^{-1}	—	[30]
	Fe_3O_4/Mg-Al LDH	Co-precipitation	Ultraviolet light	50	Liquid phase 5 mL CH_3CN 70 mL NaOH	CO CH_4	442.20 μmol·g^{-1}·h^{-1} 223.90 μmol·g^{-1}·h^{-1}	—	[114]
	Ultrathin MAl-LDH	Titration	300 W Xe lamp (400 nm < λ < 800 nm)	—	Liquid phase 2 mL water 6 mL CH_3CN	CO	43.73 μmol·g^{-1}·h^{-1}	2 mL TEOA 3.3 mg $[Ru(bpy)_3]Cl_2$·$6H_2O$	[115]
	Ag-ultrathin LDH	Titration method and self-redox	300 W Xe lamp	10	Liquid phase 2 mL water 6 mL CH_3CN	CO	757 μmol·g^{-1}·h^{-1}	2 mL TEOA 3.3 mg $[Ru(bpy)_3]Cl_2$·$6H_2O$	[116]
	Defect-rich ultrathin ZnAl-LDH nanosheet	Reverse micelle	300 W Xe lamp	100	Gas–solid phase	CO	7.60 μmol·g^{-1}·h^{-1}	—	[32]
	Ultrathin TiMgAl-LDH/RGO composite	Self-assembly	300 W Xe lamp (λ > 420 nm)	200	Gas–solid phase	CO CH_4	4.60 μmol·g^{-1}·h^{-1} 3.80 μmol·g^{-1}·h^{-1}	—	[117]
	Ultrathin Pd/CoAl-LDH	Co-precipitation	300 W Xe lamp (400 nm < λ < 800 nm)	10	Liquid phase 2 mL water 6 mL CH_3CN	CO:H_2	1:3	2 mL TEOA 3.3 mg $[Ru(bpy)_3]Cl_2$·$6H_2O$	[118]
LDHs	Monolayer NiAl-LDH	*In situ* growth	300 W Xe lamp (λ > 600 nm)	10	Liquid phase 2 mL water 6 mL CH_3CN	CH_4	70.3% selectivity	2 mL TEOA 3.3 mg $[Ru(bpy)_3]Cl_2$·$6H_2O$	[119]
	Monolayer CoAl-LDH	Separate nucleation and aging steps	300 W Xe lamp (λ > 400 nm)	10	Liquid phase 2 mL water 6 mL CH_3CN	CH_4	81.75% selectivity	2 mL TEOA 3.3 mg $[Ru(bpy)_3]Cl_2$·$6H_2O$	[120]
	Ni sites on CoFe-LDH nanosheets	Co-precipitation	300 W Xe lamp (400 nm < λ < 800 nm)	10	Liquid phase 2 mL water 6 mL CH_3CN	CH_4	78.9% selectivity	2 mL TEOA 3.3 mg $[Ru(bpy)_3]Cl_2$·$6H_2O$	[121]
	ZnTi-LDH ZnFe-LDH, ZnCo-LDH ZnGa-LDH, ZnAl-LDH	Co-precipitation	300 W Xe lamp (200 nm < λ < 800 nm)	100	Gas–solid phase	CH_4 H_2 CO	68% selectivity 100% selectivity 78%, 90% selectivity	—	[122]
	Ultrafine CeO_2-decorated LDH	Hydrothermal	300 W Xe lamp	10	Liquid phase 2 mL water 6 mL CH_3CN	CO:H_2	From 1:7.7 to 1:1.3	2 mL TEOA 3.3 mg $[Ru(bpy)_3]Cl_2$·$6H_2O$	[123]

(Continued)

	Photocatalyst	Synthesis method	Light source	Mass (mg)	Reaction system solvent	Product	Yield	Sacrificial agent or photosensitizer	References
LDHs	Co-Co-LDH/$Ti_3C_2T_x$ nanosheets	*In situ* MOF-derived	5W LED lamp	500	Liquid phase 2 mL water 3 mL CH_3CN	CO	1.25×10^4 μmol·g^{-1}·h^{-1}	1 mL TEOA 7.5 mg $[Ru(bpy)_3]Cl_2 \cdot 6H_2O$	[124]
	Ultrathin NiAl-LDH grew on 2D $Ti_3C_2T_x$	*In situ* growth	300 W Xe lamp (λ > 420 nm)	7.5	Liquid phase 4 mL water 6 mL CH_3CN	CO	2,128.46 μmol·g^{-1}·h^{-1}	2 mL TEOA 7.5 mg $[Ru(bpy)_3]Cl_2 \cdot 6H_2O$	[125]
	2D/2D CoAlLa-LDH/$Ti_3C_2T_x$ MXene	Hydrothermal	35 W Xe lamp	100	Gas–solid phase	CO CH_4	46.32 μmol·g^{-1}·h^{-1} 31.02 μmol·g^{-1}·h^{-1}	—	[126]
	Pt-loaded ex-LDH	Self-assembly	300 W Xe lamp	20	Gas–solid phase	CO	2.64 μmol·g^{-1}·h^{-1}	—	[127]
	N-doped C dot/CoAl-LDH/g-C_3N_4 heterojunction	Hydrothermal	300 W Xe lamp	50	Gas–solid phase	CH_4	25.69 μmol·g^{-1}·h^{-1}	—	[128]
	Stacking BiOCl nanoplates/Zn-Cr LDH nanosheets	Self-assembly	300 W Xe lamp	100	Gas–solid phase	CH_4	0.86 μmol·g^{-1}	—	[33]
	CoAl-LDH nanosheets	Co-precipitation	500 W Xe lamp	30	Gas–solid phase	CH_4	4.30 μmol·g^{-1}·h^{-1}	—	[129]
	Pt-Mg-Al-LDH/C_3N_4	Self-assembly	500 W Xe lamp	—	Liquid phase	CH_4	3.70 μmol	—	[42]
	NO_3^--NiAl-LDH CO_3^{2-}-NiAl-LDH	Hydrothermal	300 W Xe lamp (λ > 420 nm)	50	Liquid phase H_2O:CH_3CN = 1:3	CH_4 CO	Selectivity from 6.1% to 84.6% 0.5% to 61.1%	TEOA 3.3 mg $[Ru(bpy)_3]Cl_2 \cdot 6H_2O$	[130]
	$Cu_{2-x}S$/Ni-Al-LDH heterostructures	Hydrothermal	300 W Xe lamp	50	Liquid phase 100 mL DI water	CO CH_4	5.30 μmol·g^{-1}·h^{-1} 14.20 μmol·g^{-1}·h^{-1}	—	[131]
	Tetra porphyrin sensitized ZnTi-LDH	Hydrothermal	300 W Xe lamp	20	Liquid phase	CO CH_4	1.72 μmol·g^{-1} 8.65 μmol·g^{-1}	20 mL isopropanol	[132]
	1D/2D COF-5/CoAl-LDH	*In situ* growth	300 W Xe lamp (λ > 420 nm)	10	Liquid phase 2 mL water 20 mL CH_3CN	CO	265.40 μmol·g^{-1}	—	[133]
	2D/2D heterojunction g-C_3N_4/NiFe-LDH	*In situ* growth	300 W Xe lamp	50	Liquid phase 19 mL DI water	CO CH_4	55.79 μmol·g^{-1} 20.45 μmol·g^{-1}	1 mL TEOA	[134]
	Ultrathin 2D Ti_3C_2 anchored on porous g-C_3N_4	Self-assembly	300 W Xe lamp (λ > 420 nm)	15	Liquid phase 15 mL DI water	CH_4	0.99 μmol·g^{-1}·h^{-1}	—	[135]
	2D/2D heterojunction ultrathin MXene/Bi_2WO_6 nanosheets	*In situ* growth	300 W Xe lamp	100	Gas–solid phase	CH_4 CH_3OH	1.78 μmol·g^{-1}·h^{-1} 0.44 μmol·g^{-1}·h^{-1}	—	[136]
	TiO_2/Ti_3C_2 composite	Sol-gel	500 W Hg lamp	200	Liquid phase	CO CH_4	120.83 μmol·g^{-1} 15.91 μmol·g^{-1}	TEOA	[137]
	Few-layer g-C_3N_4 and monolayer $Ti_3C_2T_x$ MXene	Self-assembly	300 W Xe lamp	—	Gas–solid phase	CO CH_4	25.96 μmol·g^{-1} 3.70 μmol·g^{-1}	—	[138]
	2D/2D Ti_3C_2/g-C_3N_4 nanosheets	Calcination	300 W Xe lamp (λ > 420 nm)	20	Liquid phase 15 mL water	CO CH_4	5.19 μmol·g^{-1}·h^{-1} 0.044 μmol·g^{-1}·h^{-1}	—	[139]
Other 2D photocatalysts	B-doped g-C_3N_4/few-layer Ti_3C_2	Self-assembly	300 W Xe lamp (λ > 420 nm)	40	Gas–solid phase	CO CH_4	14.40 μmol·g^{-1} 35.20 μmol·g^{-1}	—	[140]
	2D/2D heterostructure black phosphorus/Bi_2WO_6	Self-assembly	300 W Xe lamp	10	Liquid phase 4 mL DI water 6 mL CH_3CN	CO H_2	20.50 μmol·g^{-1}·h^{-1} 16.80 μmol·g^{-1}·h^{-1}	2 mL TEOA	[141]
	2D/2D black phosphorus/g-C_3N_4 heterostructure	Freeze-drying treatment	300 W Xe lamp	10	Liquid phase 4 mL H_2O 6 mL CH_3CN	CO	187.70 μmol·g^{-1}·h^{-1}	2 mL TEOA	[142]
	Monolayer black phosphorus	Exfoliation method assisted by liquid nitrogen	300 W Xe lamp (λ > 420 nm)	10	Liquid phase 4 mL H_2O 6 mL CH_3CN	CO	112.60 μmol·g^{-1}·h^{-1}	2 mL TEOA	[38]
	Metal phosphide (M-P: Co_2P, Ni-P, and Cu-P)/black phosphorus nanosheet	*In situ* growth	300 W Xe lamp	10	Liquid phase 40 mL ethyl acetate	CO	255.10 μmol·g^{-1}·h^{-1}	—	[143]

(Continued)

	Photocatalyst	Synthesis method	Light source	Mass (mg)	Reaction system solvent	Product	Yield	Sacrificial agent or photosensitizer	References
Other 2D photocatalysts	COF-367-Co nanosheets	Imine-exchange	300 W Xe lamp (λ > 420 nm)	5	Liquid phase 20 mL $KHCO_3$ 352 mg ascorbic acid	CO	10,162 μmol·g^{-1}·h^{-1}	19 mg $[Ru(bpy)_3]Cl_2·6H_2O$	[144]
	2D Re-covalent organic frameworks	Precursor decmposition	225W Xe lamp (λ > 420 nm)	0.9	Liquid phase 3 mL CH_3CN	CO	98% selectivity	0.2 mL TEOA	[145]

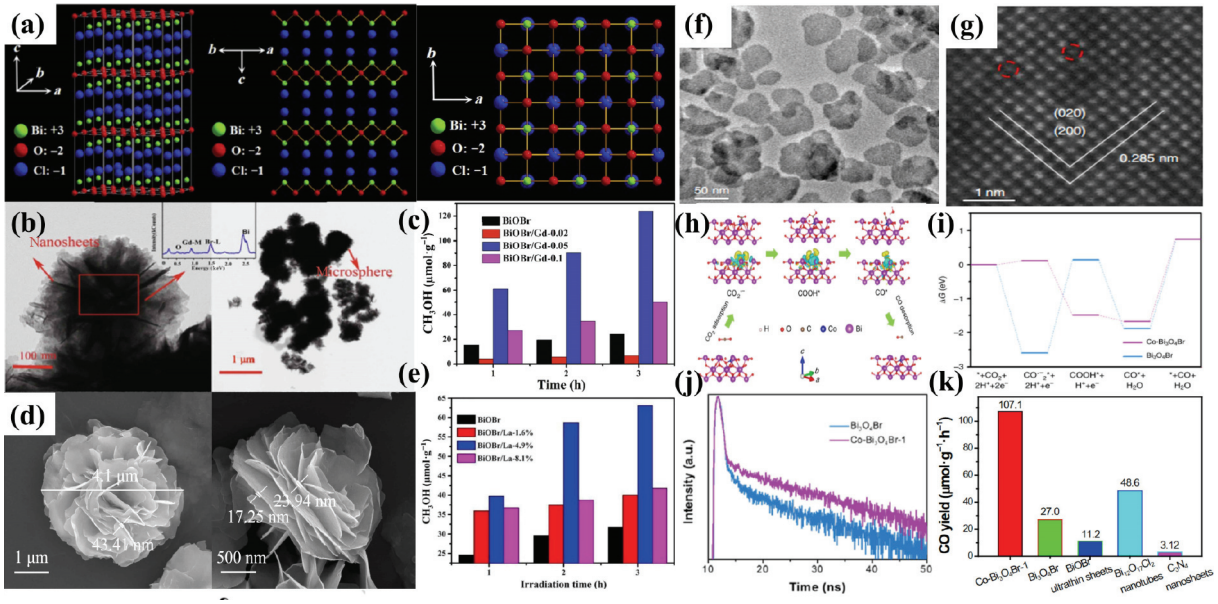

Figure 4 (a) The structure model illustration of BiOCl crystals: three-dimensional projection. Reproduced with permission from Ref. [49], © Elsevier B.V. 2016. (b) Transmission electron microscopy (TEM) images of BiOBr/Gd0.05. (c) CO_2 photoreduction for pure BiOBr and BiOBr/Gd composites. Reproduced with permission from Ref. [59], © Elsevier B.V. 2020. (d) Scanning electron microscopy (SEM) images of BiOBr and BiOBr/La-4.9%. (e) The yields of CH_3OH for BiOBr and BiOBr/La catalysts. Reproduced with permission from Ref. [41], © Elsevier B.V. 2021. (f) TEM surface morphology of Co-Bi_3O_4Br. (g) Atomic resolution high-angle annular dark-field scanning transmission electron microscopy (HAADF-STEM) images on the Co-Bi_3O_4Br. (h) Schematic representation of CO_2 photoreduction mechanism on the Co-Bi_3O_4Br. (i) Free energy diagrams of CO_2 photoreduction to CO for the Bi_3O_4Br and Co-Bi_3O_4Br. (j) Time-resolved transient photoluminescence (PL) decay. (k) Performance comparison of several ultrathin materials under the same testing conditions. Reproduced with permission from Ref. [64], © Di, J. et al. 2019.

significantly inhibited by Bi metal. The loaded Bi acted as electron traps to reduce the resistance loss in the charge transfer process.

BiOBr has a moderate bandgap, which is narrower than that of BiOCl and larger than that of BiOI, thus affording it visible light adsorption and relatively stronger reduction ability (E_{CB} = −0.81 V versus NHE). Kong et al. found that the as-synthesized ultrathin BiOBr nanosheets had a high density of oxygen atoms on the exposed (001) crystal planes. After the CO_2 reduction reaction, OVs would still be generated on the exposed surface. Vacancies would continue to be formed and updated, which also made the ultrathin BiOBr nanosheets with exposed (001) crystal planes more reactive and more efficient than bulk BiOBr nanosheets. The BiOBr nanosheets with exposed (001) crystal planes showed a CH_4 yield of 2.15 μmol·g^{-1}·h^{-1}, which was 3.3 times higher than that of bulk BiOBr [57]. Similarly, Di et al. prepared ultrathin BiOBr nanosheets with bismuth vacancies (V_{Bi}) assisted by long carbon chain ionic liquid at room temperature. Without any promoter or sacrificial agent, V_{Bi}-BiOBr nanosheets could selectively reduce CO_2 to CO with a yield rate of 20.1 μmol·g^{-1}·h^{-1}, which was similar to OVs modified samples. It was attributed to the adjusted electronic structure of BiOBr, strengthened adsorption, and activation of CO_2 [58]. In addition, Xie's research group doped different rare earth elements (Gd^{3+} [59], La [41], etc.) during the synthesis of BiOBr nanosheets to improve the performance of photocatalytic CO_2 reduction. Among them, the BiOBr nanosheets doped with Gd^{3+} also showed a hierarchical structure of microspheres (Fig. 4(b)). The doped Gd^{3+} caused the crystal plane spacing of BiOBr to be slightly reduced and widened its visible light absorption range to obtain a suitable energy band structure. Within 3 h, BiOBr with a Gd^{3+} doping ratio of 0.05 achieved a methanol yield of 123.71 μmol·g^{-1} (Fig. 4(c)), which was 5.2 times higher than that of bulk BiOBr. And the BiOBr nanosheets doped with La (Figs. 4(d) and 4(e)) also showed good photocatalytic performance for CO_2 reduction. Moreover, the incorporation of La not only caused a change in the charge density but also produced OVs in BiOBr, as confirmed by the electron paramagnetic resonance. The appearance of OVs promoted the formation of defect levels and improved the efficiency of charge transfer. In summary, the doping of La reduced the band gap and improved the visible light adsorption capacity of BiOBr, finally allowing BiOBr considerable photocatalytic activity and stability.

BiOI has also attracted much attention due to its special layered structure and narrow band gap. The study found that different facets of BiOI nanocrystals have various physicochemical properties due to anisotropy. By controlling the different exposure ratios of crystal facets, a synergistic effect was produced between the crystal facets to improve the photocatalytic reaction activity. Therefore, Ye et al. synthesized BiOI nanosheets with controllable (001) (BiOI-001) and (100) (BiOI-100) crystal planes by controlling the hydrothermal reaction time. The photocatalytic results showed that BiOI-001 exhibited better CO_2 reduction activity than BiOI-100. The controllable synthesis of BiOI-001 nanosheets had better bulk carrier separation efficiency and more CO_2 adsorption sites [54]. These factors promoted the

performance of BiOI-100 for CO_2 conversion. So far, the research only stayed on controlling the growth of the crystal plane of the semiconductor. But in a recent study, Kong et al. formed a p-n junction coupling structure by selectively chemically assembling Bi_2WO_6 nanosheets with rich OVs on BiOI nanosheets. The synergistic effect of OVs and p-n junction endowed Bi_2WO_6/BiOI with excellent performance, and the CH_4 yield reached 18.32 μmol·g^{-1}. Because the Fermi level (E_f) of the Bi_2WO_6 with OVs was higher than that of BiOI, the E_f difference between BiOI and Bi_2WO_6 allowed electrons to migrate from Bi_2WO_6 to BiOI when they were tightly contacted. In this way, a built-in electric field that quickly transferred charges across the interface was created in Bi_2WO_6/BiOI, which effectively improved the efficiency of charge separation [43].

3.1.2 *Bismuth-rich oxyhalides ($Bi_xO_yX_z$)*

In addition to BiOX (X = Cl, Br, and I), a series of non-stoichiometric bismuth-rich oxyhalides $Bi_xO_yX_z$ (X = Cl, Br, and I) have also been extensively studied in recent years. Similar to BiOX, $Bi_xO_yX_z$ also has a layered structure with strong interlayer bonding and van der Waals force interaction. The typical 2D layered structure and the narrow band gap enable $Bi_xO_yX_z$ strong potential for CO_2 photocatalytic reduction.

Bi_3O_4Cl has a layered crystal structure with a relatively small band gap of 2.79 eV. Ye's research group combined Bi_3O_4Cl with g-C_3N_4 to form a heterojunction, and uncovered that the Bi_3O_4Cl/g-C_3N_4 heterojunction photocatalyst realized the conversion of CO_2 to CO and CH_4, and the generation rates were 6.6 and 1.9 μmol·g^{-1}·h^{-1}, respectively [60]. Besides, Ye et al. [61] also demonstrated that another bismuth-rich oxyhalide ($Bi_{24}O_{31}Cl_{10}$) had good photocatalytic activity for CO_2 reduction. They introduced OVs on the surface of $Bi_{24}O_{31}Cl_{10}$, which significantly reduced the formation barrier of CO_2 reduction intermediate COOH· and improved the conversion rate. Moreover, Quan et al. synthesized $Bi_{12}O_{17}Cl_2$ and combined it with carbonized polymer quantum dots [62]. The experimental results manifested that the good photocatalytic performance benefited from effective CO_2 adsorption and activation, broad light absorption range, and efficient photo-generated electron–hole separation as well as the increased specific surface area.

Bi-O-Br system also contains a variety of bismuth-rich photocatalysts, such as $Bi_4O_5Br_2$, which has an obvious uneven charge distribution between [Bi-O] layers and Br atoms, forming a local polarization field for promoting the separation of electrons and holes. Ye et al. used the precursor method to synthesize ultrathin $Bi_4O_5Br_2$ nanosheets, and the yield of CO within 2 h was as high as 63.13 μmol·g^{-1} [63]. Apart from $Bi_4O_5Br_2$, Di et al. synthesized bismuth oxybromide (Bi_3O_4Br) nanosheet (Figs. 4(f) and 4(g)) and creatively improved the activity for photocatalytic CO_2 conversion by anchoring the cobalt single atom on the Bi_3O_4Br atomic layer (Fig. 4(k)), and thus the yield of CO was as high as 107.1 μmol·g^{-1}·h^{-1}. Furthermore, time-resolved fluorescence emission decay spectroscopy (Fig. 4(j)) and surface photovoltage showed that the average fluorescence lifetime of cobalt-doped Bi_3O_4Br was much higher than that of bulk Bi_3O_4Br nanosheets. It was further proved that cobalt atoms can be used as charge separation centers to capture photo-generated electrons and improve the utilization efficiency of carriers. Through the density functional theory (DFT) calculation (Figs. 4(h) and 4(i)), it was found that the CO_2 reduction intermediate COOH* was the key limiting step. Stabilizing the COOH* and transferring the limiting step from the formation of adsorbed COOH* to CO* desorption could lower the CO_2 activation energy barrier, which indirectly increased the activity of the reaction [64].

$Bi_xO_yI_z$ photocatalysts have also received research attention in recent years. Ding et al. used different molecular precursor methods to process the same precursor to obtain two different bismuth-rich bismuth iodide oxides $Bi_4O_5I_2$ and Bi_5O_7I. $Bi_4O_5I_2$ was prepared by simple hydrolysis and Bi_5O_7I was obtained by sintering the precursor at a high temperature of 400 °C. Under the irradiation of 420 nm monochromatic light, both catalysts could selectively reduce CO_2 to CO [65]. Further, Bai prepared the semi-metal Bi/$Bi_4O_5I_2$ through hydrolysis of the above precursors. When the ratio of Bi/I was 1.95/1, Bi/$Bi_4O_5I_2$ showed the best photocatalytic activity for CO_2 conversion with a CO yield rate of 40.02 μmol·g^{-1}·h^{-1} [66].

Compared with BiOX, $Bi_xO_yX_z$ with a tunable composition generally has a more suitable energy band structure for covering the partial visible light region and meeting the requirements for CO_2 reduction. Thus, $Bi_xO_yX_z$ demonstrates the large potential for photocatalytic reduction of CO_2.

3.1.3 *Bismuth layered perovskites*

Bi_2WO_6 is a typical Aurvillius layered perovskite semiconductor, which has attracted extensive attention due to its non-toxicity and moderate band gap for visible light irradiation. Moreover, the presence of $[Bi_2O_2]^{2+}$ and fluorite-like $[WO_4]^{2-}$ octahedral structural units in Bi_2WO_6 is conducive to the construction of the ultrathin structure (Fig. 5(a)), which allows photo-generated electron–hole pairs to more easily migrate to the surface for photocatalytic reactions. Besides, most layered perovskites, such as Bi_2WO_6, Bi_2MoO_6, and $Bi_4Ti_3O_{12}$, are ferroelectric materials that originate from lattice distortion in the perovskite structure [67].

Ribeiro et al. used a hydrothermal method to successfully synthesize Bi_2WO_6 with different morphologies by adding different amounts of polyvinylpyrrolidone (PVP) [68]. The difference in reaction time and PVP concentration affected the morphology of Bi_2WO_6. The existence of PVP could stabilize Bi_2WO_6 by adsorbing its long chain. As the concentration of PVP increased, the nanosheets were assembled to form spheres and the Bi_2WO_6 nanosheets were agglomerated to form dense particles at a higher concentration of PVP. When the reaction time was 8 h and the amount of PVP was 10 wt.%, the as-prepared Bi_2WO_6 nanosheets exhibited the best photocatalytic activity with an ethanol yield of 68.9 μmol·g^{-1}·h^{-1}. In addition, Kong et al. used a simple *in situ* topological transformation method to convert BiOBr with exposed {001} facet into Bi_2WO_6. The obtained Bi_2WO_6 not only retained the exposed {001} crystal facet but also showed a narrower band gap compared with the samples synthesized by the traditional hydrothermal method. Thus, the CH_4 output from CO_2 reduction over Bi_2WO_6 with {001} facet was 2.6 and 9.3 times higher than that of BiOBr nanosheets and bulk Bi_2WO_6, respectively [69]. In addition to the regulation of crystal planes, the construction of vacancy defects was also widely studied in Bi_2WO_6. Li et al. introduced OVs on the surface of Bi_2WO_6, which not only increased light absorption but also promoted the separation of photo-generated electron–hole pairs, allowing more photo-generated electrons to participate in the reaction [70]. Cao et al. prepared carbon-doped (C-doped) ultrathin (~ 4.1 nm) Bi_2WO_6 nanosheets by hydrothermal treatment and calcination to improve the photocatalytic activity, which not only shortened the carrier diffusion distance but also provided more active sites [71]. Due to carbon doping, the absorption edge of Bi_2WO_6 exhibited a significant red shift along with the generation of an intermediate energy state, which demonstrated that C doping reduced the band gap of Bi_2WO_6 nanosheets and enhanced light absorption. The energy band potential comparison also revealed that the CB of C-doped Bi_2WO_6 was more negative and therefore had a stronger reducing ability, which can provide a sufficient driving force for CO_2

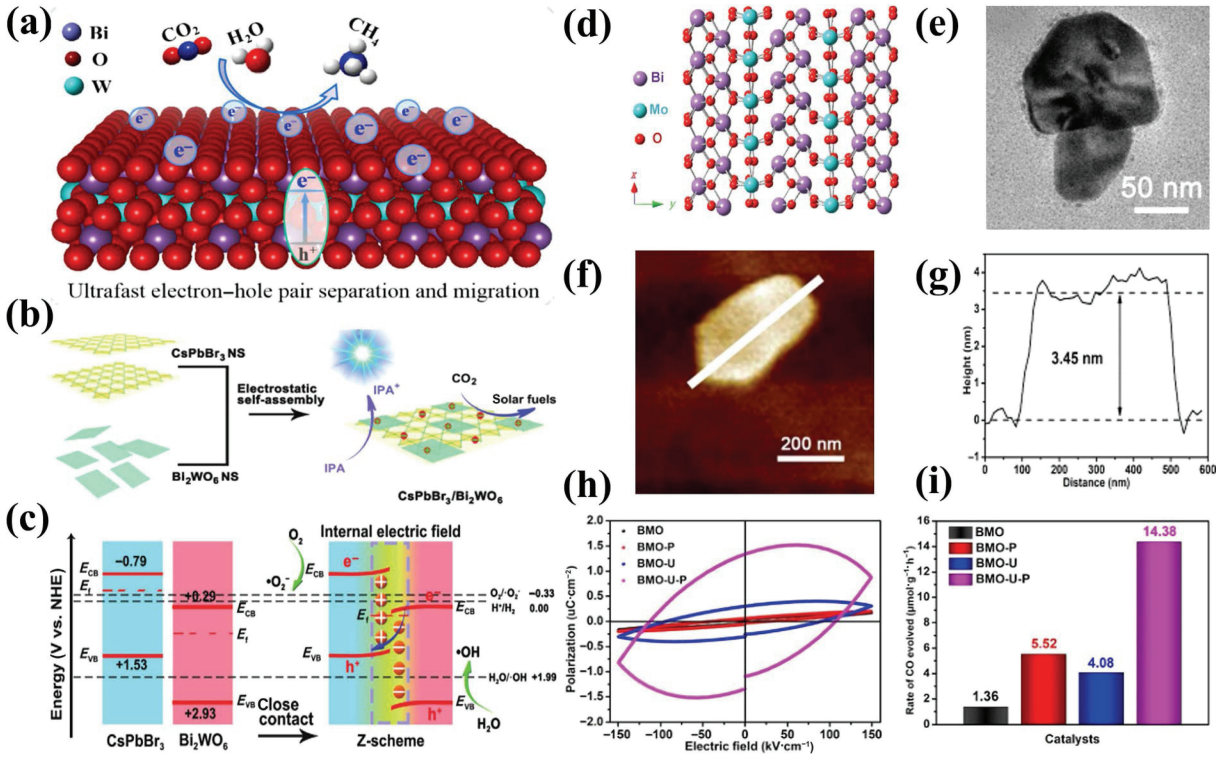

Figure 5 (a) The proposed CO_2 photoreduction mechanism over the as developed Bi_2WO_6. Reproduced with permission from Ref. [69], © American Chemical Society 2020. (b) Schematic diagram of 2D/2D $CsPbBr_3/Bi_2WO_6$ heterojunction prepared via an electrostatic self-assembly process. (c) Energy band diagram. Reproduced with permission from Ref. [73], © Wiley-VCH GmbH 2020. (d) Schematic diagram of orthorhombic Bi_2MoO_6 crystal structure. Reproduced with permission from Ref. [74], © WILEY-VCH Verlag GmbH & Co. KGaA, Weinheim 2017. (e) TEM image of BMO-U. (f) AFM image of BMO-U and (g) the corresponding height profile. (h) Electric hysteresis loop. (i) Production rate of the BMO, BMO-P, BMO-U, and BMO-U-P samples under simulated sunlight. Reproduced with permission from Ref. [75], © The Royal Society of Chemistry 2020.

reduction. Compared with the bulk Bi_2WO_6 and Bi_2WO_6 nanosheets, the CO_2 photoreduction activity has been further improved in C-doped Bi_2WO_6. The corresponding CH_3OH and C_2H_5OH generation rates were 1.15 and 0.65 μmol·g^{-1}·h^{-1}, respectively. Furthermore, Li et al. grafted chloride on the surface of Bi_2WO_6 nanosheets to improve the photocatalytic activity for CO_2 reduction. By adjusting the loading of chloride, the selectivity to CH_4 over Bi_2WO_6 was increased from 51.29% to 94.98%. The yield was also about 10 times higher than that of unmodified Bi_2WO_6 [72]. Besides, heterojunction was considered a valid technique to modify Bi_2WO_6. Jiang et al. used the electrostatic assembly method to assemble the ultrathin Bi_2WO_6 nanosheets on the surface of $CsPbBr_3$. The tight interface in $CsPbBr_3/Bi_2WO_6$ heterojunction (Fig. 5(b)) enabled the effective separation and transport of charges (Fig. 5(c)). The production yield of CO and CH_4 reached 1,582.0 μmol·g^{-1} in 30 h, which was 12.2 times higher than that of Bi_2WO_6 nanosheets [73].

Bismuth molybdate (Bi_2MoO_6) is also a typical Aurivillius layered perovskite ferroelectric semiconductor with a suitable energy band width and unique layered structure. The crystal structure of Bi_2MoO_6 is composed of alternate $[Bi_2O_2]^{2+}$ structural units and perovskite $[MoO_4]^{2-}$ slices, and oxygen atoms are shared between layers (Fig. 5(d)). In recent years, the photocatalytic performance for CO_2 reduction of Bi_2MoO_6 is studied [74].

To explore the effect of ferroelectricity on photocatalysis of Bi_2MoO_6, our group found that 2D ultrathin structure and corona poling collaboratively promoted the ferroelectricity of Bi_2MoO_6. Firstly, the fabrication of the 2D ultrathin Bi_2MoO_6 (BMO-U) structure (Fig. 5(e)) was beneficial in increasing the active sites and shortening the carrier migration path to promote the photo-generated electron–hole separation. AFM testified that the thickness decreased from 40 nm for bulk Bi_2MoO_6 to 3 nm for BMO-U nanosheets (Figs. 5(f) and 5(g)). And then BMO-U was post-treated by corona poling (BMO-U-P) for strengthening the ferroelectricity to build the internal electric field. According to the Kelvin probe force microscopy (KPFM) image, it was manifested that a larger polarization electric field was generated on Bi_2MoO_6 nanosheets after corona poling. The hysteresis loop indicated (Fig. 5(h)) that the saturation polarization and residual polarization of BMO-U-P nanosheets after corona polarization treatment were also stronger than all other samples. It was believed that the corona poling may cause the alignment of ferroelectric domains, thereby increasing the ferroelectricity. The photocatalytic results uncovered that ultrathin structure and corona polarization synergistically promoted the photocatalytic CO_2 reduction activity of Bi_2MoO_6 with a CO yield of 14.38 μmol·g^{-1}·h^{-1}, ~ 10 times more than the bulk Bi_2MoO_6 (Fig. 5(i)) [75].

$Bi_4Ti_3O_{12}$ is composed of $[Bi_2O_2]^{2+}$ slices and perovskite-type TiO_6 octahedral layers (Fig. 6(a)). As a ferroelectric material, $Bi_4Ti_3O_{12}$ exhibits an internal spontaneous polarization to an extent as a result of the distortion of its polyhedral $[TiO_6]$ octahedron. However, due to its relatively large forbidden bandgap (about 2.9 eV), it has limited photocatalytic activity and fast electron–hole pair recombination as well. Our group described an impressive case of ultrathin 2D $Bi_4Ti_3O_{12}$ nanosheets which were introduced OVs by the low-temperature hydrothermal method (Figs. 6(b)–6(d)). In comparison with bulk $Bi_4Ti_3O_{12}$, the ultrathin structure allowed shortening the migration distance of carriers from bulk to the surface, and OVs enhanced photoabsorption and adsorption of CO_2 molecules (Fig. 6(e)). The photocatalytic experiments showed that $Bi_4Ti_3O_{12}$ nanosheets with OVs manifested a superior CO evolution rate of 11.7 μmol·g^{-1}·h^{-1} via a synergistic effect [76]. This kind of cooperative tactic was also reflected in another work from our group. $Bi_4Ti_3O_{12}$ was treated by corona poling and I-grafting to obtain a modified $Bi_4Ti_3O_{12}$ (BTO-P-I), enabling $Bi_4Ti_3O_{12}$ efficient photocatalytic activity. Attributing to the ferroelectric properties of $Bi_4Ti_3O_{12}$, after the

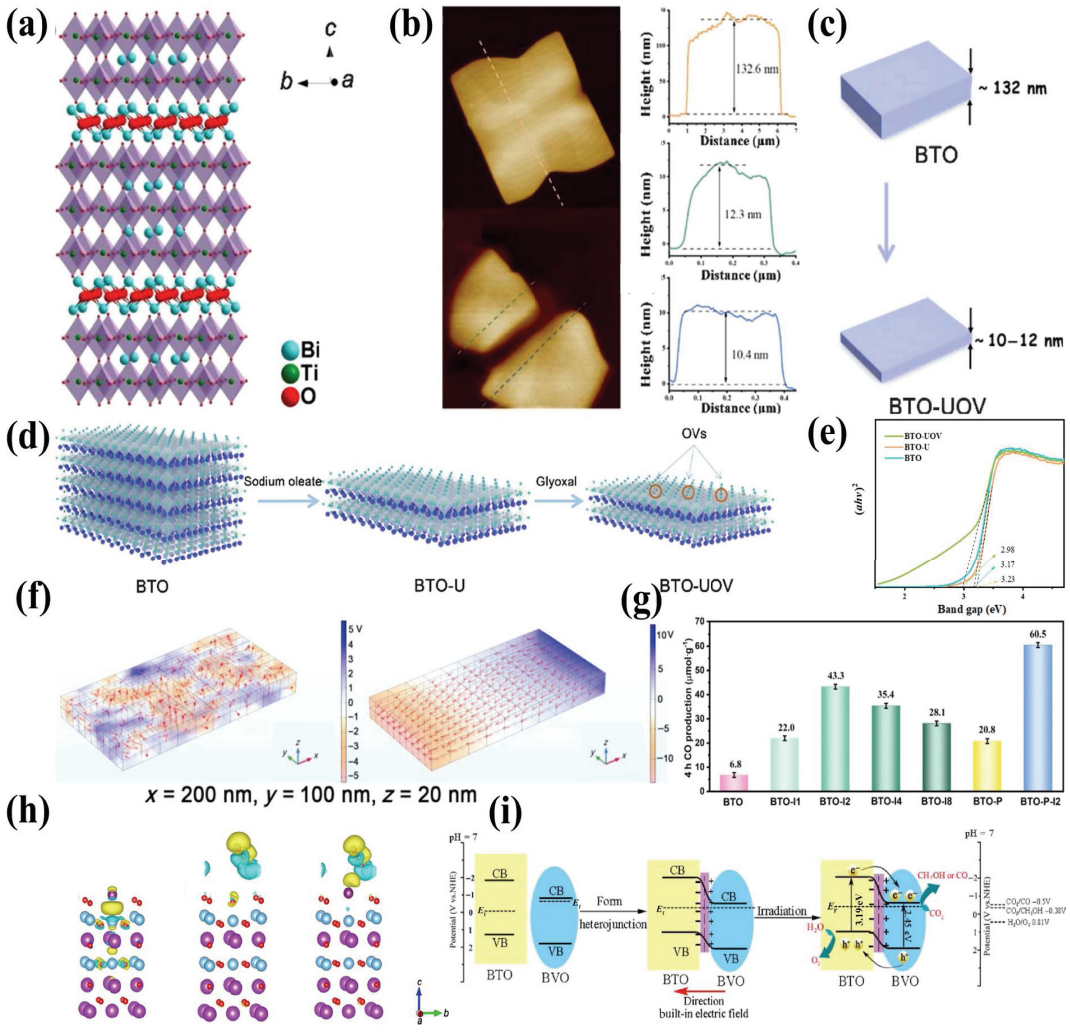

Figure 6 (a) Crystal structure of BTO. (b) AFM images and height distribution curve of BTO and BTO-UOV. (c) The scheme for the thickness evolution from BTO to BTO-UOV. (d) Schematic illustration for the formation of BTO-UOV. (e) Band gap of BTO, BTO-U and BTO-UOV. Reproduced with permission from Ref. [76], © Science China Press 2020. (f) Finite element method simulation for the potential distribution of BTO with the external electric field of 0 V·cm^{-1} and 10 kV·cm^{-1}. (g) Apparent rate of CO yields by the photoreduction of CO_2 over BTO, BTO-I*X* (*X* = 1, 2, 4, and 8), BTO-P and BTO-P-I2 samples under simulated solar light irradiation. (h) Charge difference of BTO-I, and CO_2 absorbed BTO and BTO-I. Reproduced with permission from Ref. [77], © Wiley-VCH 2021. (i) Band alignment and electron structure of $BiVO_4/Bi_4Ti_3O_{12}$ heterojunction. Reproduced with permission from Ref. [78], © Elsevier B.V. 2020.

corona poling (BTO-P), the more chaotic and disordered electric domains inside $Bi_4Ti_3O_{12}$ turned unanimous (Fig. 6(f)), and then an internal electric field was formed along the polarization direction which greatly facilitated the charge migration in the opposite direction. It is also uncovered that the I-grafting $Bi_4Ti_3O_{12}$ (BTO-I) formed a surface local electric field to further separate carriers and emerge plentiful active sites to promote CO_2 adsorption by theoretical calculation (Fig. 6(h)). Significantly, the synchronous promotion was realized by corona poling and I-grafting, resulting in 9 times enhanced CO production rate compared to the unmodified $Bi_4Ti_3O_{12}$ (Fig. 6(g)) [77]. Moreover, similar to corona poling, the construction of heterojunction composite semiconductors was also an effective strategy to form the built-in field. Wang et al. obtained the type II heterojunction via growing $BiVO_4$ on the surface of $Bi_4Ti_3O_{12}$ nanosheets by an *in situ* hydrothermal method without adding any sacrificial agent and co-catalyst. Driven by the built-in electric field (Fig. 6(i)), the photo-generated holes and electrons were separated in different locations, which fulfilled the water oxidation and CO_2 reduction reactions on $Bi_4Ti_3O_{12}$ and $BiVO_4$, respectively, resulting in the production of CH_3OH and CO [78].

3.1.4 *Other Bi-based photocatalysts*

$BiOIO_3$ is founded as a nonlinear optical material with a non-centrosymmetric (NCS) crystal structure, which also has a layered crystal structure consisting of $[Bi_2O_2]$ layers and IO_3 polyhedra [79]. Recently, it is widely investigated as an efficient UV light-responsive photocatalyst. Our group prepared a series of thickness-tunable $BiOIO_3$ nanoplate photocatalysts (Figs. 7(a) and 7(d)) by controlling the acidity of the reaction solution via the hydrothermal method [80]. Previous studies demonstrated that the reduction in the thickness of the photocatalysts can shorten the migration path of photo-generated carriers to increase photocatalytic activity. However, in this work $BiOIO_3$-b3 with a moderate thickness displayed more excellent bulk separation and interfacial charge transfer than the thinnest $BiOIO_3$-b4. Theoretical calculations and photodeposition experiment results revealed that the photo-generated electrons tended to migrate to the {010} facet (Figs. 7(e) and 7(f)) and holes were accumulated on the {100} facet (Fig. 7(g)). The tuning of nanoplate thickness controlled the ratio of the top {010} facet to the lateral {100} facet, and thus the $BiOIO_3$-b3 with exposing 77.4% {010} facet showed the best photocatalytic CO_2 reduction activity. In addition, $BiOIO_3$ as a NCS material derived from the polar IO_3 units can generate a large polarization electric field along the *c* axis, which largely facilitates the separation and migration of charges [81]. Our group disclosed that the oriented growth of $BiOIO_3$ single-crystal nanostrips along the [001] direction allowed additive dipole

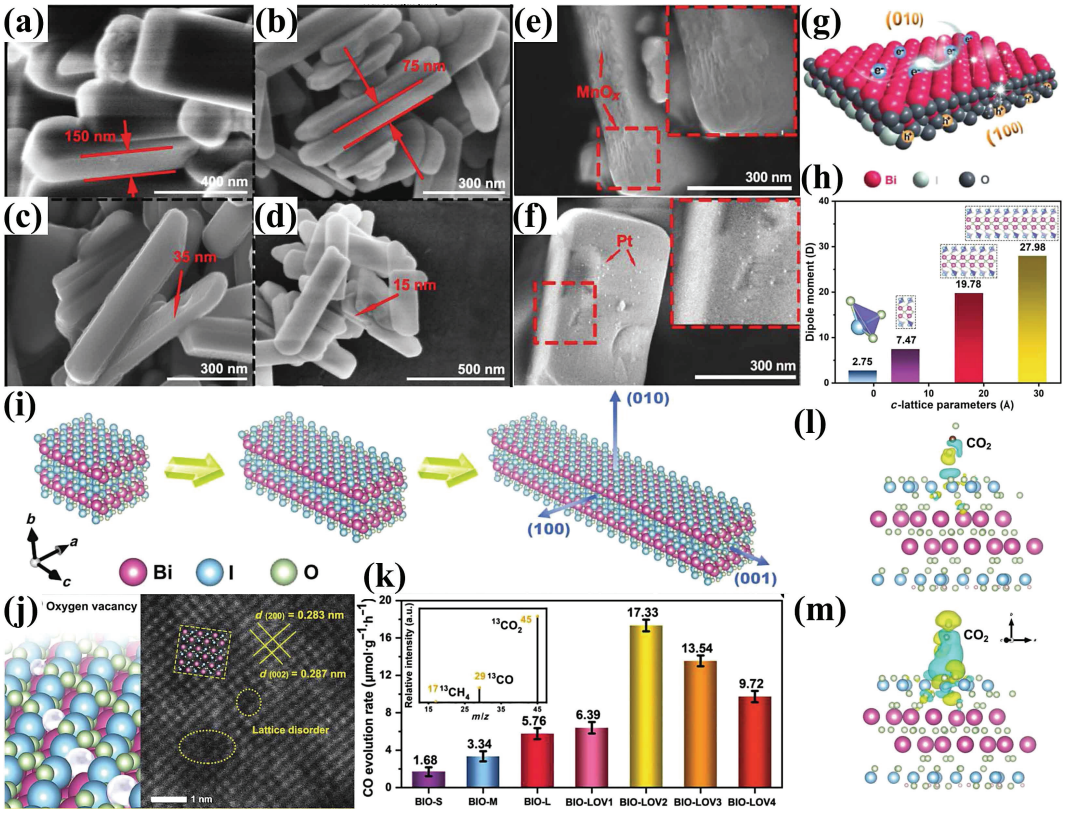

Figure 7 (a)–(d) SEM images of $BiOIO_3$. (e) and (f) SEM images of $BiOIO_3$-b3 with photodeposited Pt and MnO_x. (g) Crystal structure model with photo-generated electrons and holes of $BiOIO_3$-b3. Reproduced with permission from Ref. [80], © WILEY-VCH Verlag GmbH & Co. KGaA, Weinheim 2018. (h) The dipole moment of IO_3 polyhedra and the $BiOIO_3$ unit cells with different *c*-lattice lengths. (i) Schematic illustration for the morphology evolution for $BiOIO_3$. (j) Atomic-resolution HAADF-STEM image of $BiOIO_3$. (k) The production rates of CO generated in the CO_2 reduction. (l) and (m) Charge difference of CO_2 adsorbed on $BiOIO_3$ and $BiOIO_3$ with OVs. Reproduced with permission from Ref. [81], © WILEY-VCH Verlag GmbH & Co. KGaA, Weinheim 2020.

moments of the IO_3 polyhedrons that resulted in strengthened the macroscopic polarization along this direction, and the introduction of OVs created a local electric field (Figs. 7(h)–7(j)), leading to more effective charge transfer and enhanced adsorption of CO_2 (Figs. 7(l) and 7(m)). As a result, coupling macroscopic spontaneous polarization and surface oxygen vacancies of $BiOIO_3$ nanostrips manifested the highest CO evolution rate (17.33 $\mu mol \cdot g^{-1} \cdot h^{-1}$) from CO_2 photoreduction (Fig. 7(k)). Furthermore, in a recent study, Zou et al. used a hydrothermal method to prepare $Fe_2O_3/BiOIO_3$ composite photocatalyst. Compounding with Fe_2O_3 can effectively solve the problem of the large band gap of $BiOIO_3$. So these heterojunction photocatalysts effectively transferred photo-generated electrons and selectively reduced CO_2 to CO [82].

In addition, our group synthesized Bi_4NbO_8Cl nanosheets with {001} exposing facets through the molten salt method, and then prepared Bi_4NbO_8Cl/g-C_3N_4 2D/2D heterojunctions through high-energy ball milling and post-sintering. The formation of type-II heterojunction was confirmed through selective photodeposition of Pt and MnO_x. The strong interfacial interaction of Bi_4NbO_8Cl/g-C_3N_4 greatly promoted charge separation and photocatalytic activity [83]. Similarly, high-energy ball milling was used to prepare the g-C_3N_4/Bi_2O_2 [BO_2(OH)] Z-scheme junction, which has strong redox ability and high charge separation efficiency, thus showing a high photocatalytic CO_2 reduction activity with a CO production rate of 6.09 $\mu mol \cdot g^{-1} \cdot h^{-1}$ [84].

In summary, various layered Bi-based materials with 2D structures are very suitable for photocatalytic CO_2 reduction. Though the above layered Bi-based photocatalysts have made considerable progress, the exploration for new Bi-based materials with a broad light response range and efficient charge separation for high-performance CO_2 photoreduction is highly expected.

3.2 Layered perovskites

In the past few decades, binary metal oxides such as TiO_2 [146], WO_3 [147], Co_3O_4 [148], and ZnO [149] have been widely studied as photocatalysts in the light-driven conversion of CO_2. Beyond these metal oxides, the perovskites, e.g., $SrTiO_3$, attract considerable attention for photocatalytic hydrogen production [150], degradation of dye wastewater [151], and photovoltaic cells [152], due to their high catalytic activity, good stability, and long charge diffusion length. Recently, they show good performance in photocatalytic CO_2 reduction.

Perovskites have larger lattice distortion than binary oxides, which can effectively separate carriers, so they have gradually become a type of promising semiconductor photocatalyst [153]. The general formula of typical perovskite is ABO_3, where A and B are two cations of dissimilar bulks, O is the anion that bonds A to B. Usually, O is the oxygen atom, while it can also be halogen, sulfur, and nitrogen. As the simplest perovskite, Nb-based photocatalysts have been extensively studied in ABO_3. For example, Shao et al. synthesized the ZnO quantum dot/KNb_3O_8 nanosheet by a two-step hydrothermal method for photocatalytically reducing CO_2, and the photocatalytic efficiency for CH_3OH evolution was as high as 1,539.77 $\mu mol \cdot g^{-1} \cdot h^{-1}$, which was attributed to the heterojunction formed by ZnO quantum dots and KNb_3O_8 [154]. And D. Praveen Kumar et al. combined a few-layered 2D g-C_3N_4 with perovskite Ba_2NbFeO_6 nanosheets (Fig. 8(a)) for CO_2 photo-conversion. The optimized g-C_3N_4/Ba_2NbFeO_6 casts a prominent photocatalytic CO_2 reduction activity for CH_4 and CO evolution with a rate of 4.8 and 32 $\mu mol \cdot g^{-1} \cdot h^{-1}$, respectively [155]. Besides, researchers have unfolded that the Ti-based perovskite materials also show a better photocatalytic performance. Byeong Sub Kwak et al. exfoliated layered Sr_2TiO_4 perovskite to obtain nanosheets with a narrow band gap, high specific surface area, and high dispersibility. The

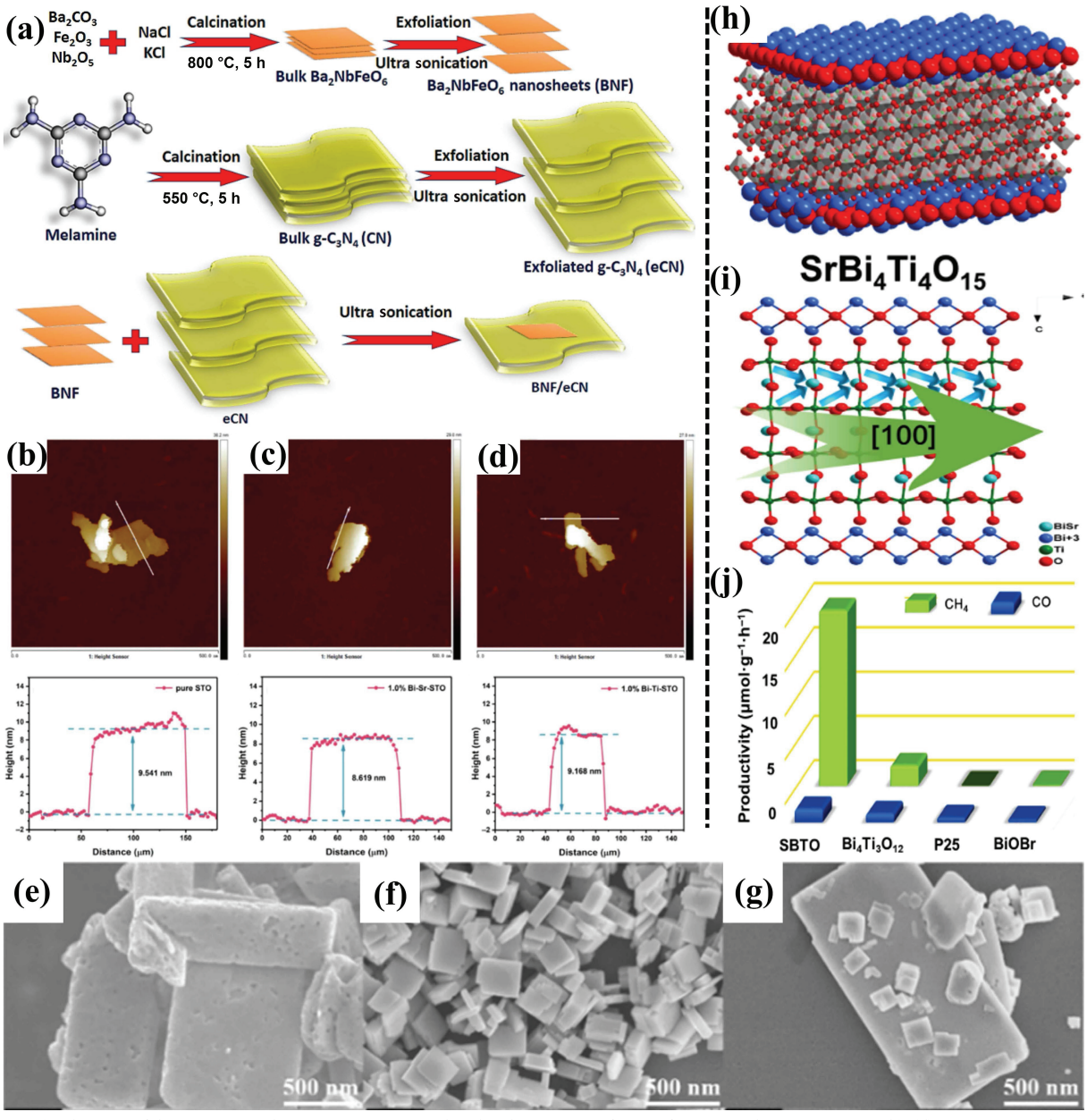

Figure 8 (a) Schematic of the g-C_3N_4/Ba_2NbFeO_6 processes. Reproduced with permission from Ref. [155], © Elsevier B.V. 2021. (b)–(d) AFM images of pure STO, 1.0% Bi-Sr-STO, and 1.0% Bi-Ti-STO samples. Reproduced with permission from Ref. [99], © Elsevier Inc. 2021. (e)–(g) SEM images of LTON, WO_3, and WO_3/LTON. Reproduced with permission from Ref. [94], © American Chemical Society, 2021. (h) $SrBi_4Ti_4O_{15}$ crystal structure. (i) Polarization direction along an axis in the crystal structure of $SrBi_4Ti_4O_{15}$. (j) The corresponding rates. Reproduced with permission from Ref. [95], © Elsevier Ltd. 2018.

exfoliated Sr_2TiO_4 nanosheets produced an excellent performance for photocatalytic reduction of CO_2. The CH_4 yield of Sr_2TiO_4 was 3,431.77 μmol·g^{-1} in 8 h [96]. Furthermore, Zhu et al. successfully synthesized 2D $SrTiO_{3-x}$ nanosheets with OVs. To enhance the photocatalytic performance, they doped Bi element in $SrTiO_{3-x}$ to prepare *X* Bi-Sr-STO and *X* Bi-Ti-STO samples with a thickness of ~ 9 nm (Figs. 8(b)–8(d)). Bi doping, OVs, and the Sr active site effectively suppressed the recombination of photo-generated electrons and holes and improved the light absorption efficiency, resulting in increased CO and CH_4 yield of Bi-Ti-STO by 1.79 and 1.57 times that of $SrTiO_{3-x}$ [99]. Besides, Su et al. loaded 2D WO_3 nanosheets on 2D $LaTiO_2N$ microplates to construct a direct Z-scheme photocatalytic system (Figs. 8(e)–8(g)), which realized the conversion of gas-phase CO_2 and H_2O without cocatalysts or sacrificial reagents under visible light. The optimal WO_3/$LaTiO_2N$ composite yielded CO and CH_4 rates of 2.21 and 0.36 μmol·g^{-1}·h^{-1}, respectively [94]. In addition, our group reported a ferroelectric layered perovskite $SrBi_4Ti_4O_{15}$ nanosheets as a powerful photocatalyst for efficient CO_2 reduction (Fig. 8(h)). It was mainly due to $SrBi_4Ti_4O_{15}$ nanosheets exhibiting strong ferroelectric spontaneous polarization along the [100] direction (Fig. 8(i)), which enabled efficient separation and photo-generated electrons and holes along the opposite direction [95]. In the gas–solid reaction system, $SrBi_4Ti_4O_{15}$ with the strongest ferroelectricity converted CO_2 to CH_4 (Fig. 8(j)) with a rate of 19.8 μmol·g^{-1}·h^{-1} without co-catalysts and sacrificial agents.

According to the reported research, the layered perovskite materials could be roughly divided into the following five types: Ruddlesden–Popper (RP) phase (Fig. 9(d)), Dion–Jacobson (DJ) phase (Fig. 9(e)), Aurivillius phase (Fig. 9(c)), (110) layered (Fig. 9(b)), and (111) layered (Fig. 9(a)) [152, 156]. Generally, the 2D layered perovskite materials show higher photocatalytic activity than the three-dimensional perovskites. For example, Takayoshi et al. successfully prepared 2D $Li_2LaTa_2O_6N$ (Fig. 9(f)) photocatalytic materials with a layered perovskite structure by using lithium-rich oxide precursors through high-temperature thermal ammonolysis [92]. They demonstrated that $Li_2LaTa_2O_6N$ was composed of double-layer $[LaTa_2O_6N]^{2-}$ perovskite slabs (Figs. 9(g) and 9(h))

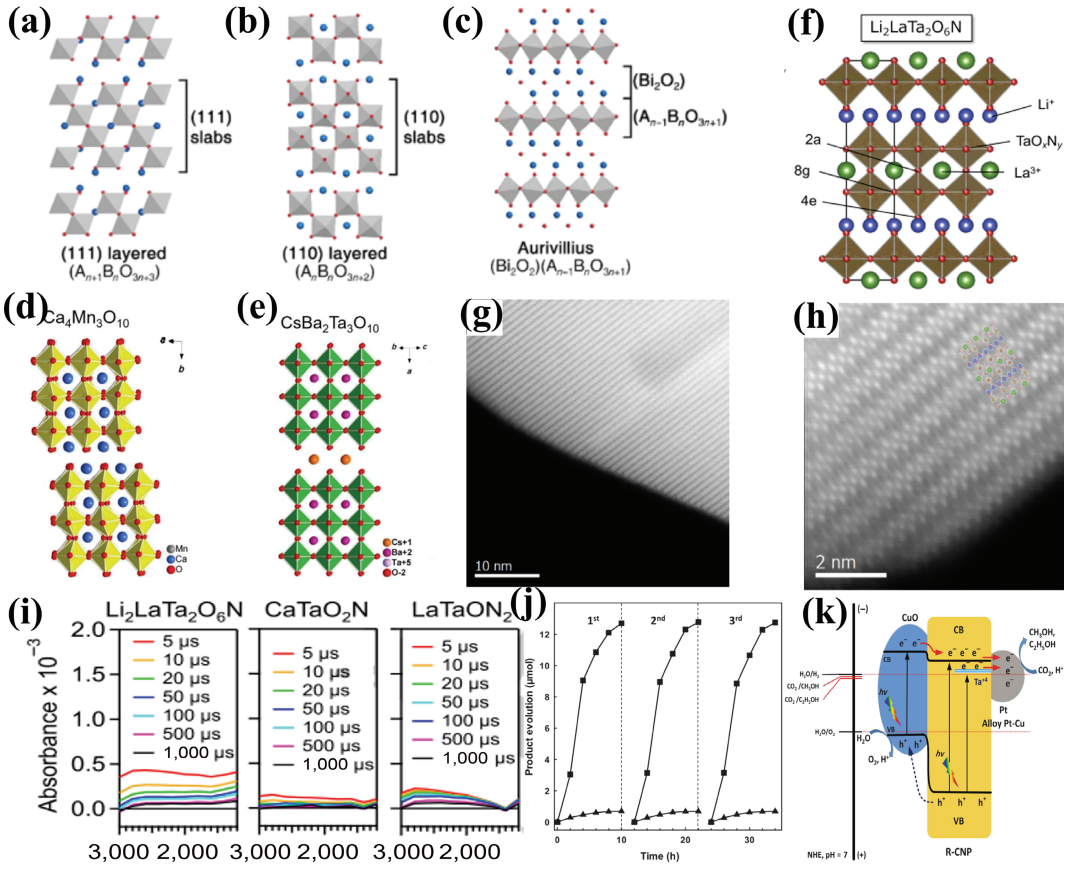

Figure 9 (a)–(c) Crystal structures of typical layered perovskite (111) layered, (110) layered, and Aurivillius phases. Reproduced with permission from Ref. [152], © WILEY-VCH Verlag GmbH & Co. KGaA, Weinheim 2017. (d) Ruddlesden–Popper phases and (e) Dion–Jacobson phases. Reproduced with permission from Ref. [156], © American Chemical Society 2018. (f) Crystal structures of $Li_2LaTa_2O_6N$. (g) HAADF-STEM image and (h) magnified HAADF-STEM image of $Li_2LaTa_2O_6N$. (i) Transient absorption spectra of these oxynirides after laser pulse excitation at 480 nm under vacuum. Reproduced with permission from Ref. [92], © Oshima, T. et al. 2018. (j) Product evolution of R-Pt/Cu-CNP catalyst for three cycles. (k) Schematic diagram of CO_2 photoreduction mechanism over R-Pt-CNP. Reproduced with permission from Ref. [98], © WILEY-VCH Verlag GmbH & Co. KGaA, Weinheim 2017.

through the typical high-angle annular dark-field image, and it was also clear that $Li_2LaTa_2O_6N$ was a highly crystalline material, which was very conducive to photocatalytic reaction. Compared with the three-dimensional $LaTaON_2$ and $CaTaO_2N$ materials under visible light irradiation, only $Li_2LaTa_2O_6N$ could convert CO_2 to formic acid stably with high selectivity (> 97%). According to the transient absorption spectroscopy (Fig. 9(i)), the high performance of $Li_2LaTa_2O_6N$ was mainly due to its 2D layered perovskite structure, which had a lower density of trap states and a higher density of reactive electrons.

$H_2SrTa_2O_7$ is an RP phase perovskite and it was found that the loading of Ag on its surface improved the selectivity of CO_2 reduction into CO to 60.9% [97]. In addition, Chen et al. revealed the effect of loading different metal particles on the surface of $H_2SrTa_2O_7$ for the photocatalytic reduction products of CO_2. It was found that Au-loaded $H_2SrTa_2O_7$ showed higher selectivity for H_2, and Cu_2O-loaded $H_2SrTa_2O_7$ exhibited higher activity for the evolution of CO. While Pd-loaded $H_2SrTa_2O_7$ uncovered high rates for both CO and H_2 evolution [157]. For DJ-phase perovskites ($AB_2Ta_3O_{10}$), due to the advantages of ion exchange, easy exfoliation, and high crystallinity, they are widely studied in photocatalysis. Nhu-Nang Vu synthesized DJ-phase layered perovskite Pt/Cu-$HCa_2Ta_3O_{10}$ nanosheets to obtain a larger surface area by exfoliation. The Pt/Cu-$HCa_2Ta_3O_{10}$ nanosheets had a higher sensitivity (Fig. 9(j)) than the bulk phase during photocatalytic reduction of CO_2. The CO_2 conversion efficiency reached 14% within 10 h under visible light irradiation, while the bulk catalyst could not even absorb visible light. The authors concluded that the high efficiency might be attributed to the higher specific surface area of the nanosheets providing more reactive sites, and the appearance of Ta^{4+} and OVs after stripping increased the light absorption. In addition, the loaded Pt particles and CuO (Fig. 9(k)) enhanced the separation rate of photo-generated electron–holes and CO_2 adsorption, resulting in the formation rates of ethanol and methanol of 113 and 7.4 μmol·g^{-1}·h^{-1}, respectively. By contrast, only methanol was obtained with a rate of 125.9 μmol·g^{-1}·h^{-1} in the absence of CuO nanoparticles [98]. (110) and (111) layered perovskites are homologous layered structures formed by the BO_6 octahedrons shared by A cations. Among the two structures, $ALa_4Ti_4O_{15}$ (A = Ca, Sr, and Ba) was the most extensively researched, owing to its anisotropic structure that could generate photo-generated electrons with a higher reduction potential [158]. Wang et al. found that the (110)-phase perovskite structure $La_2Ti_2O_7$ exhibited high activity for photocatalytic conversion of CO_2 to CO after Ag modification. The authors explained that the photocatalytic activity depended on the crystallinity and specific surface area of $La_2Ti_2O_7$, and experiments uncovered $La_2Ti_2O_7$ calcined at 1,373 K for 4 h had the highest rate of CO production [159]. The Aurivillius phase perovskite oxides for CO_2 reduction mainly include Bi_2WO_6, Bi_2MoO_6, and $Bi_4Ti_3O_{12}$ which have been discussed in the section on layered Bi-based photocatalyst.

In summary, most perovskite oxides have a poor response to visible light, which severely restricts the yield of photocatalytic reduction of CO_2. At present, doping and heterojunction formation are the most commonly used strategies for improving the photocatalytic activity of perovskite oxides, and ferroelectric properties as the characteristics of some perovskite oxides will be studied more and more to correlate with their photocatalytic activity.

3.3 TMDs

Due to the unique electronic structure, 2D transition metal chalcogenides with a large light absorption range are considered auspicious photocatalytic materials [160]. The MX_2 molecular layer (Fig. 10) is formed by sandwiching the M atomic layer between two hexagonal X atomic layers [161]. It's easy to find that the chalcogen element is saturated so that the reaction activity is not too high. Interestingly, the structure of TMDs is similar to graphene, which is connected by weak van der Waals forces between the layers. The unique layered structure allows it a strong quantum effect and surface effect [162]. TMDs nanosheets can quickly move carriers from the inside to the surface to promote photocatalytic reactions [163]. The suitable bandgap causes excellent photoluminescence properties and relatively high exciton binding energy [164], which makes it widely used in various fields such as photoelectric detectors [165], photocatalytic decomposition of water to produce hydrogen [166], treatment of heavy metal ions in water [167], and nitrogen reduction [168].

In recent years, 2D TMDs nanomaterials have been extensively researched in the photocatalytic reduction of CO_2, and the most popular TMDs are MoS_2 and SnS_2. For example, Li et al. synthesized nanoflower-like SnS_2 composed of nanosheets with a thickness of 10 nm through a simple one-step hydrothermal method. The sample exhibited vigorous photocatalytic activity for converting CO_2 into CO and CH_4, and the production of CH_4 rate could reach 97.5 μmol·g^{-1}, which was 5.7 times higher than that of sheet-like SnS_2. It was attributed that the flower-like structure was conducive to the accumulation of electrons, increasing the carrier utilization efficiency [110]. SnS_2 also has common defects, which are easily recombined by photo-generated holes resulting in restraining the activity of photocatalysis. It is necessary to adopt various modification methods such as compounding and adding sacrificial agents to inhibit this process.

MoS_2 has a narrow band gap of ~ 1.2 eV and adjustable CB position by changing the number of layers due to quantum confinement, so MoS_2 is regarded as a promising photocatalyst [169]. Ordinarily, MoS_2 displayed as 2H and 1T phases, respectively. Ouyang and co-researchers used functional density theory to simulate Ag/2H-MoS_2 composites and explained that Ag atoms could be used as an electron capture center to transfer photo-generated electrons from 2H-MoS_2's VB, which enhanced the photocatalytic performance of 2H-MoS_2 nanosheets. Calculations on the electronic band structure showed that the band gap of Ag/2H-MoS_2 was reduced and the CB bottom was also more negative, which was conducive to the photo-conversion of CO_2 to hydrocarbon fuel. And the photoabsorption edge was red-shifted to 680 nm to achieve enhanced utilization of visible light. And they revealed the route for photocatalytic reduction of CO_2 in this reaction was CO_2 → *COOH → *CO → *CHO → *CH_2O → *OCH_3 → *CH_3OH → CH_4 [100]. In addition, Yin's group successfully prepared the 2H phase exfoliated MoS_2 nanosheets in the presence of lithium ions by simple hydrothermal, realizing the 1T-to-2H phase conversion of MoS_2 (Fig. 11(a)) in o-dichlorobenzene solution. Compared with MoS_2 prepared by the traditional hydrothermal route, the liquid phase exfoliated 2H-MoS_2 had a larger specific surface area (Figs. 11(b) and 11(c)), which was beneficial to CO_2 photo-conversion. To further enhance the photocatalytic performance of 2H-MoS_2, they loaded Ag nanoparticles, which effectively restricted the recombination of photo-generated electrons and holes. The Ag/2H-MoS_2 with 20 wt.% Ag exhibited the highest photocatalytic activity for the reduction of CO_2 to produce CH_3OH with a rate as high as 365.08 μmol·g^{-1}·h^{-1} [39]. Besides, Bilawal Khan et al. also coupled MoS_2 and SnO_2 with Ag loaded to form a CB cascade to further enhance carrier separation and light absorption [170].

According to the literature, coupling semiconductors is an effective approach to improving the photocatalytic reactivity of MoS_2 as well. Yu et al. used hydrothermal synthesis to prepare a 1D/2D TiO_2/MoS_2 composite (Fig. 11(d)) photocatalyst with a hierarchical structure, in which MoS_2 nanosheets were vertically distributed on the TiO_2 fiber to form a hybrid nanostructure. The tight contact between TiO_2 and MoS_2 produced a rich porous structure that enhanced the adsorption of CO_2. According to the theoretical calculation, TiO_2 has a higher work function (Figs. 11(e) and 11(f)) than MoS_2, leading to the photoelectron transfer from MoS_2 to TiO_2, which promoted a more effective separation of charge carriers [101]. Likewise, Tu's group grew MoS_2 nanosheets *in situ* on TiO_2 nanosheets to form 2D/2D hybrid nanojunctions, which exhibited high selectivity in the photocatalytic conversion of CO_2 to CH_3OH. The Mo end edge of MoS_2 nanosheets showed metal properties and high d-electron density. In the reaction of CH_3OH formation, the negatively charged CH_xO_y accumulated around Mo cations due to the electrostatic effect of positive and negative charges. The electrical vacancies would remain in MoS_2, which was conducive to the

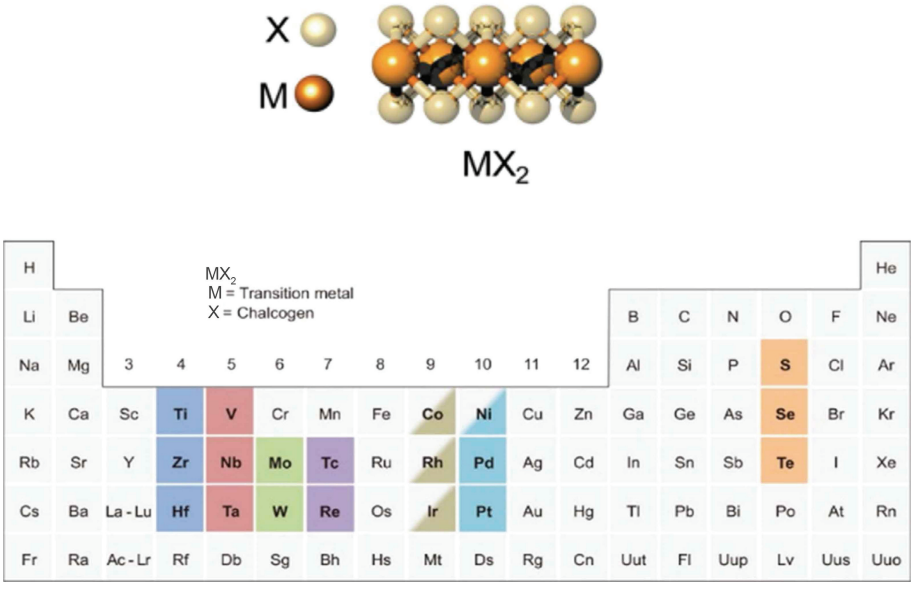

Figure 10 Transition metals and sulfur group elements constitute layered TMD. Reproduced with permission from Ref. [164], © The Royal Society of Chemistry 2018.

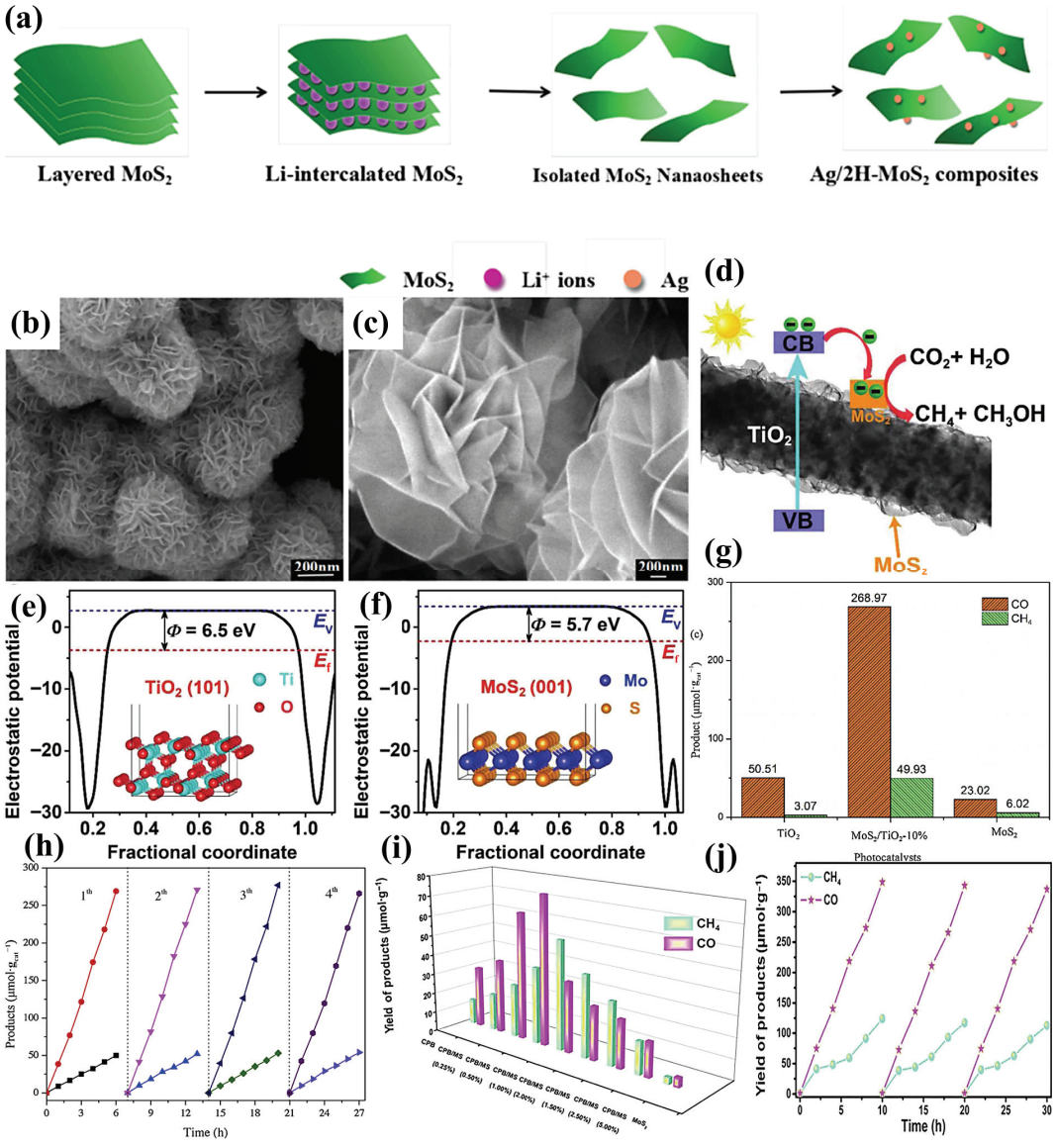

Figure 11 (a) Illustration of the synthesis of Ag/2H-MoS_2 composites. SEM images of (b) MoS_2 and (c) phase-converted 2H-MoS_2. Reproduced with permission from Ref. [39], © WILEY-VCH Verlag GmbH & Co. KGaA, Weinheim 2019. (d) Schematic of TiO_2 and MoS_2 heterojunction. (e) and (f) Electrostatic potentials of TiO_2 and MoS_2. Reproduced with permission from Ref. [101], © WILEY-VCH Verlag GmbH & Co. KGaA, Weinheim 2018. (g) The rate of CH_4 and CO generation. (h) The recyclability of different samples during the photoreduction of CO_2. Reproduced with permission from Ref. [102], © Elsevier B.V. 2019. (i) The effect of different ratios of MoS_2 loads on $CsPbBr_3$ for photocatalytic activity and (j) the stability test on CPB/MS photocatalytic CO_2 reduction. Reproduced with permission from Ref. [104], © Elsevier B.V. 2020.

stability of the CH_xO_y intermediate, thereby promoting the conversion of CO_2 to CH_3OH [171]. In a similar work, the experimental process and ratio of TiO_2/MoS_2 were optimized to increase the conversion efficiency of CO_2, and the 10 wt.% TiO_2/MoS_2 heterojunction photocatalyst produced the max CO and CH_4 yields of 268.97 and 49.93 μmol·g^{-1}, respectively, with a high stability (Figs. 11(g) and 11(h)) [102]. Moreover, Yang et al. designed a new COF/TMD heterojunction photocatalyst C_4N/MoS_2 and then used theoretical calculation to uncover its structural stability and electronic properties. By simulating the geometric structure of C_4N/MoS_2, they found between the C_4N layer and the MoS_2 layer was an interaction. The formation of the built-in electric field was conducive to the separation of photo-generated electrons and holes, generating more active sites, and improving the photocatalytic reaction activity [172]. The formation of intimate interaction at the interface of heterojunction photocatalyst always benefits the separation of photo-generated electron–hole pairs. Sangita Kumari et al. prepared hexagonal boron nitride (h-BN)/MoS_2 composite material with close contact. The change in the E_f caused a higher charge transfer efficiency in this heterojunction photocatalyst. With triethanolamine as a sacrificial agent, the yields of CH_3OH by BN/MoS_2 greatly reached 5,994 μmol·g^{-1}·h^{-1} within 24 h [103]. Besides, Li et al. created a large number of OVs in MoS_2/MoO_3-X to promote charge separation and induce surface plasmon resonance, resulting in the photocatalytic reduction of CO_2 for CO generation with a selectivity of 94% [113]. In addition, Zhu et al. anchored inorganic $CsPbBr_3$ perovskite crystals on monolayer MoS_2 nanosheets to prepare $CsPbBr_3$/MoS_2 photocatalysts for CO_2 reduction [104]. Compared with a single-component photocatalyst, an electric field was built in $CsPbBr_3$/MoS_2 to effectively separate charges and generate more active sites to promote the activation of CO_2, which gave rise to the CH_4 and CO evolution rate of 12.8 and 25.0 μmol·g^{-1}·h^{-1}, respectively (Fig. 11(i)), with high cycling stability (Fig. 11(j)).

SnS_2 is an n-type semiconductor with an energy bandgap of ~ 2.48 eV, and its average carrier diffusion length is about 0.19 μm. Nevertheless, it has a similar disadvantage to MoS_2, which is the fast recombination of photo-generated electrons and holes caused by the narrow bandgap. Therefore, effectively suppressing

the recombination of charge carriers has become the main problem for SnS_2 to overcome.

Indrajit Shown et al. used the L-cysteine-assisted hydrothermal method to prepare C doped SnS_2 (C-SnS_2). Because of the presence of L-cysteine, C-SnS_2 displayed a uniform nanosheets structure (about 30–60 nm) (Figs. 12(a) and 12(b)), which was smaller and thinner than bulk SnS_2 nanoplates, beneficial to the carrier diffusion process. The interstitial carbon doping induced microstrain in the SnS_2 lattice, resulting in enhanced photocatalytic properties as compared with undoped SnS_2. C-SnS_2 casts a prominent CH_3CHO evolution rate of 125.66 μmol·100 mg_{cat}^{-1} (Fig. 12(c)) which was 250 times than SnS_2. Meanwhile, C-SnS_2 retained a quantum efficiency of more than 0.7% parallel to bulk under 300 W halogen light (Fig. 12(d)). DFT calculations showed that the introduction of interstitial C atoms promoted the adsorption and dissociation potential of CO_2 molecules on the surface of C-SnS_2, which significantly increased the photocatalytic performance of CO_2 reduction [106].

In addition, the construction of heterojunction is usually used to facilitate the photocatalytic activity of SnS_2. For example, She et al. prepared SnS_2/TiO_2 2D/2D heterojunction photocatalysts via the hydrothermal method. Attributed to a stronger contact interface, the yield of CH_4 over SnS_2/TiO_2 reached 23 μmol·g^{-1}·h^{-1}, approximately 9 times higher than SnS_2 [107]. Likewise, Wang et al. assembled Cs_2SnI_6 nanocrystals uniformly on SnS_2 nanosheets to obtain a Cs_2SnI_6/SnS_2 heterojunction by a simple *in situ* crystallization method (Figs. 12(e), 12(g), and 12(h)). KPFM showed that the surface photovoltage of Cs_2SnI_6/SnS_2 was much larger than that of pristine SnS_2, indicating promoted separation of photo-generated electron–hole pairs. Thus, Cs_2SnI_6/SnS_2 exhibited a 5.4 time in photocatalytic CO_2 reduction compared to SnS_2 (Fig. 12(f)) [108]. Furthermore, Yin's group prepared the 2D face-to-face SnS_2/Au/g-C_3N_4 ternary photocatalyst with a well-distribution of Au nanoparticles (Figs. 12(i) and 12(j)) [109]. Au nanoparticles acted as an electronic transport bridge to accelerate electron transport, resulting in the CO and CH_4 rates of 93.81 and 74.98 μmol·g^{-1}·h^{-1}, respectively. Besides MoS_2 and SnS_2, some other TMDs compounds also showed good performance in photocatalytic CO_2 reduction, such as WS_2 [173], WSe_2 [37], and ReS_2 [30].

In summary, although 2D TMDs have been widely used for photocatalytic reduction of CO_2, their high cost, instability, and moderate photocatalytic activity are still needed to be solved. TMDs contain two phase states, namely 2H (semiconductor phase) and 1T (metal phase). But there are currently few studies on phase engineering for CO_2 reduction. In addition, the active sites studied in most of the reported are concentrated on the edge of the TMDs and the large specific surface area of the 2D TMDs was not effectively utilized.

3.4 LDHs

LDHs is a type of low-cost clay with a layered structure and high porosity [40], which comprises $M(OH)_6$ octahedrons and embeds anions in the matrix layer (Fig. 13).

Its general formula is $[M_{1-x}^{2+}M_x^{3+}(OH)_2]^{x+}(An)_{x/n}\cdot mH_2O$, in which M^{2+} and M^{3+} are divalent and trivalent cations (e.g., Mg^{2+}, Fe^{2+}, Co^{2+}, Ni^{2+}, Zn^{2+}, Al^{3+}, Cr^{3+}, and Fe^{3+}), respectively. An is an interlayer anion (e.g., NO_3^-, CO_3^{2-}, and SO_4^{2-}), in which metal atoms are highly ordered and dispersed on the laminate [174]. LDHs show a series of fascinating physical and chemical properties, such as positively charged flakes, flexibility in composition, large specific surface area, and adjustable energy band from 2.0 to 5.4 eV [175, 176]. Particularly, the inherent layered structure of LDHs can be reduced to ultrathin nanosheets along the *c*-axis and produce coordinated unsaturated sites [177], which makes them a promising photocatalyst. However, LDHs still exhibit inefficient photocatalytic performance due to the rapid recombination of the generated electrons and holes [178].

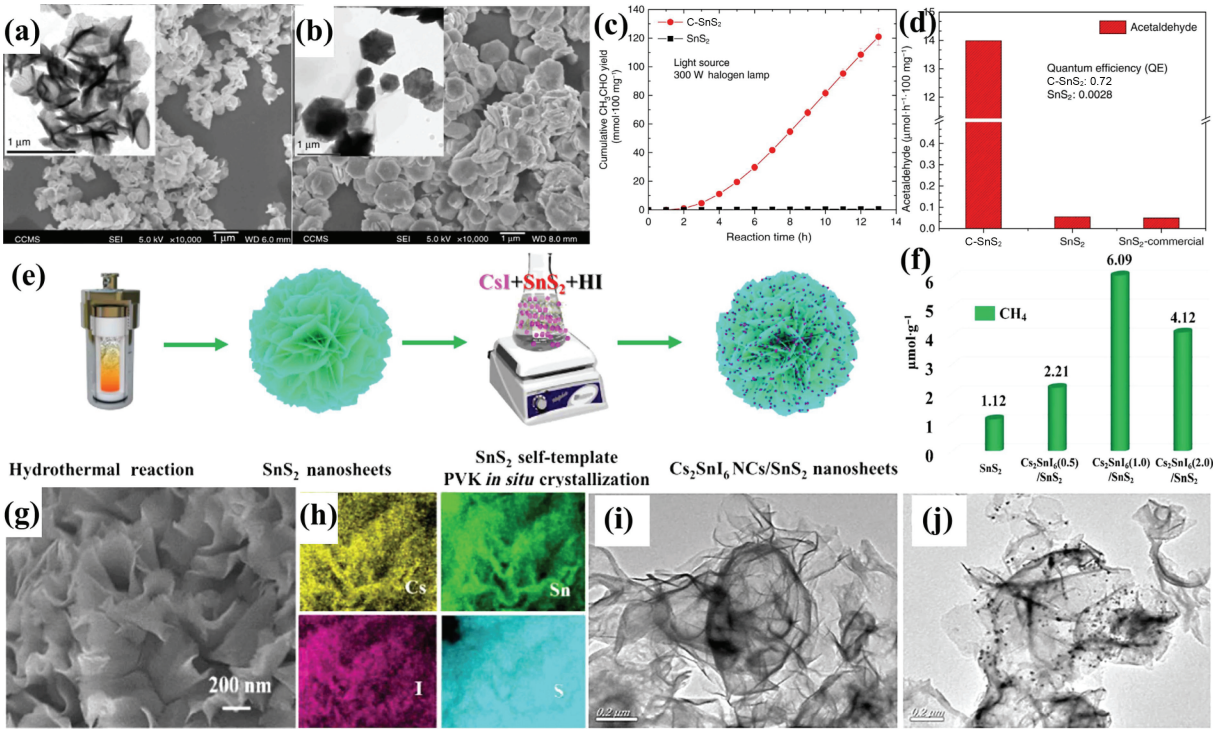

Figure 12 (a) and (b) SEM and high-resolution TEM (HRTEM) images of C-SnS_2 and SnS_2. (c) Cumulative acetaldehyde formation yield of C-SnS_2 and SnS_2. (d) Comparative solar fuel formation rate and quantum efficiency of C-SnS_2, SnS_2, and commercial SnS_2 under a visible light source. Reproduced with permission from Ref. [106], © Shown, I. et al. 2018. (e) Schematic of the synthesis for the Cs_2SnI_6/SnS_2 heterostructure. (f) Comparison of photocatalytic CO_2 reduction activities of SnS_2, Cs_2SnI_6(0.5)/SnS_2, Cs_2SnI_6(1.0)/SnS_2, and Cs_2SnI_6(2.0)/SnS_2. (g) and (h) SEM and energy-dispersive X-ray (EDX) elemental mapping images of Cs_2SnI_6/SnS_2. Reproduced with permission from Ref. [108], © American Chemical Society 2019. (i) TEM image of the SnS_2/g-C_3N_4 intercalation. (j) TEM image of the SnS_2/Au/g-C_3N_4 embedded heterostructure. Reproduced with permission from Ref. [109], © Elsevier B.V. 2020.

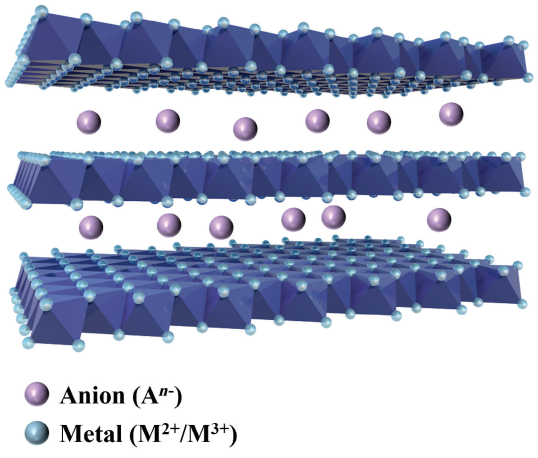

Figure 13 Structural illustration of layered double hydroxide.

LDHs have increased stacking structure allowing to easily obtain ultrathin nanosheets via stripped. For instance, Song's group prepared a variety of ultrathin MAl-LDH (u-MAl-LDH) (M = Mg^{2+}, Co^{2+}, Ni^{2+}, and Zn^{2+}). They found that the photocatalytic activity of u-CoAl-LDH synthesized with $[Ru(bpy)_3]Cl_2·6H_2O$ as the photoinitiator had the best performance, and the yield of CO under 600 nm light irradiation was 43.73 mmol·g^{-1}·h^{-1}. More importantly, according to the X-ray absorption fine structure (XAFS) characterization, the ultrathin structure made CoAl-LDH rich in OVs and metal vacancies (V_M), which reduced the band gap and increased the ability to adsorb H_2O and CO_2 [115]. Likewise, Liu et al. also successfully synthesized 2D ultrathin Mg-Al LDH via the co-precipitation method and modified it by Fe_3O_4.

The ultrathin structure allowed the fast migration of the photoelectron along the bulk photocatalyst, and Fe_3O_4 further enhanced the separation efficiency of charge carriers. The synergy of ultrathin Mg-Al LDH and Fe_3O_4 resulted in superior photocatalytic activity for CO_2 reduction. The as-prepared Fe_3O_4/Mg-Al LDH yielded CO and CH_4 with a rate of 442.2 and 223.9 μmol·g^{-1}·h^{-1}, respectively [114]. However, the loading of metal nanoparticles is also an effective way to enhance the photocatalytic activity of ultrathin LDHs. A self-redox strategy was developed to anchor Ag nanoparticles based on single-layer ultrathin LDHs (Ag-ultrathin LDH) (Fig. 14(a)). Compared with ultrathin LDH, Ag-ultrathin LDH showed much better photocatalytic CO_2 reduction into CO with a yield of 757 μmol·g^{-1}·h^{-1} and selectivity of 94.5% (Fig. 14(b)). The excellent performance was attributed to the strong interfacial bonding between Ag and LDH, which not only enhanced the separation ability of carriers but also effectively promoted the adsorption and activation of CO_2, reducing the formation energy of CO_2 reduction intermediate *COOH (Fig. 14(c)) [116]. Similarly, Song et al. introduced highly dispersed Pd on ultrathin CoAl-LDH, which could accurately adjust the CO/H_2 molar ratio from 1:0.74 to 1:3 under visible light irradiation. The loaded Pd significantly improved the charge transfer. At the same time, Pd atoms were also used to trap H atoms and reduce them to H_2. Syngas could still be generated even under light irradiation greater than 600 nm, which provided a reference for infrared photocatalytic CO_2 reduction [118]. Moreover, Zhang et al. synthesized ultrathin Zn-containing LDH nanosheets by using a simple templated hydrothermal route. The transverse dimensions of Zn-containing LDH nanosheets could be turned from 5 μm to 40 nm, and the thickness was about 2.7 nm (Figs. 14(d)–14(f)). It was founded that OVs and unsaturated Zn were generated as the thickness of the Zn-containing LDH nanosheet decreased, which could serve as the active sites for capturing CO_2 and H_2O, improving the photocatalytic activity for CO_2 reduction [32]. And Wang et al. used the electrostatic assembly method to obtain a tight composite consisting of GO and ultrathin Ti-based LDH [117]. The unsaturated coordination of LDHs and GO gave rise to the generation of Ti^{3+}-OVs and electron-rich carbon defects, which promoted visible light absorption and the adsorption and activation of CO_2.

Due to the flexible interlayer cation composition characteristics of LDHs, Zhang's group achieved control of product selectivity by changing the trivalent or tetravalent metal ions（M = Ti^{4+}, Fe^{3+}, Co^{3+}, Ga^{3+}, and Al^{3+}）in a series of zinc-based LDH photocatalysts. The main CO_2 photoreduction product of ZnTi-LDH was CH_4; ZnFe-LDH and ZnCo-LDH mainly produced H_2 from water splitting, and ZnGa-LDH and ZnAl-LDH primarily generated CO (Fig. 15(a)). And they used the d-band center theory to reasonably explain the adsorption of CO_2 and H_2O and the photocatalytic activity affected by M^{4+} and M^{3+} cations. Firstly, the closer the d-band center (E_d) to E_f, the greater influence on the molecules adsorbed on the photocatalyst's surface. Because electrons were more easily accepted by molecules adsorbed on the surface to react [179]. The E_d of ZnTi-LDH was the closest to the E_f, so its main product was CH_4. The E_d of ZnGa-LDH and ZnAl-LDH was relatively far away from the E_f, while for ZnFe-LDH and ZnCo-LDH their E_d was farther away from the E_f, so they could not adsorb and activate CO_2 (Fig. 15(b)) [122]. This study provided new perspectives for improving the selectivity of CO_2 reduction products. Besides, Song's group prepared a series of single-layer NiAl-LDH with a thickness of 27 (b-NiAl-LDH), 5 (f-NiAl-LDH), and 1 nm (m-NiAl-LDH) (Figs. 14(g)–14(i))). It was found that the by-product H_2 of CO_2 reduction gradually decreased as the layer thickness decreased, and correspondingly the selectivity of CH_4 increased from 0.1% to 2.4% to 16.5% under light irradiation > 400 nm (Fig. 14(j)). Furthermore, under irradiation of light greater than 600 nm, H_2 was wholly suppressed. After the precise adjustment of the irradiation wavelength, the selectivity of CH_4 could reach 70.3% (Fig. 14(k)) [119]. And Song's research group improved the reaction vessel by adding a small amount of layer growth inhibitor formamide and using separate nucleation and aging steps to obtain single-layer LDH with a thickness of 1 nm (Fig. 14(l)). Because of the uniform lateral size and abundant defects, the electron transport capacity was effectively improved in single-layer LDH, thus enabling a CH_4 production selectivity of 81.75% from CO_2 reduction (Fig. 14(m)) [120]. In addition, Tan et al. also used the hydrothermally synthesized cerium oxide-modified LDHs (LDHs, Ce-*x*) in different proportions based on the cation-adjustable characteristics of LDHs between layers [123]. The ratio of CO/H_2 could be changed from 1/7.1 (LDH) to 1/1.30 (Ce-0.15), achieving the highest CO yield of 85 μmol·g^{-1}·h^{-1}. LDH-Ce-0.15 still could reduce CO_2, even under the light irradiation of 600 nm. To improve the photocatalytic performance of binary LDHs, Hao et al. synthesized a NiCoFe-LDH ternary nanosheet by introducing Ni sites. Interestingly, under the irradiation of visible light above 400 nm, NiCoFe-LDH showed an increased selectivity of CH_4 from 0% to 56.6% compared with CoFe-LDH. Under above 500 nm, the selectivity of CH_4 could be increased to 78.9%, and that of H_2 production was suppressed to 1.7%. Experimental and theoretical results revealed that the main reason was that the introduction of Ni sites reduced the bandgap of NiCoFe-LDH and improved the charge separation efficiency [121].

Besides the above-mentioned strategies, the thin layered structure of LDHs also made it easy to combine with other catalysts to achieve better catalytic performance. For example, NiFe-LDH was combined with g-C_3N_4 to form a 2D/2D heterojunction [134]. The perfect band matching between NiFe-

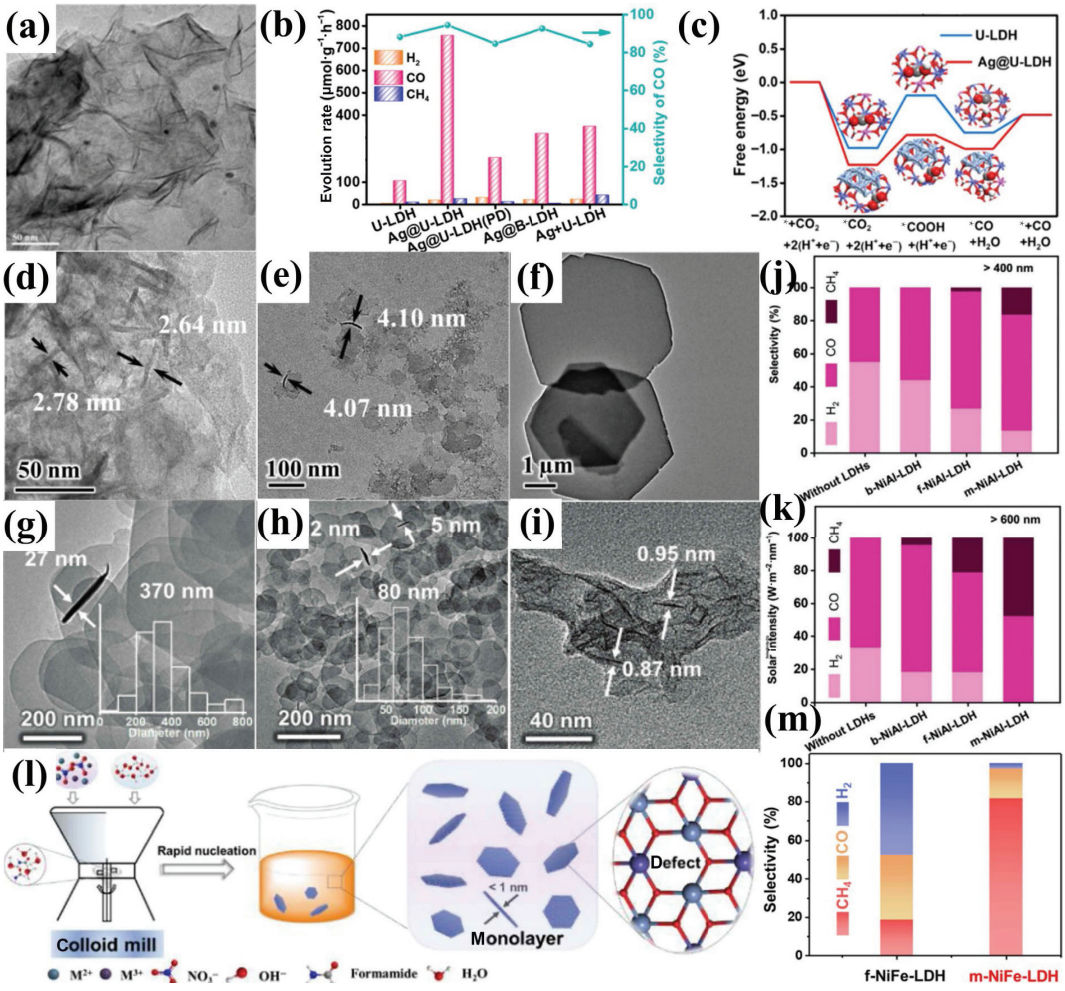

Figure 14 (a) HRTEM image of Ag-ultrathin LDH. (b) Catalytic evaluation of CO_2 photoreduction under light irradiation on various catalysts in the atmosphere of CO_2. (c) Free energy diagrams of CO_2 reduction to CO on U-LDH and Ag-ultrathin LDH. Reproduced with permission from Ref. [116], © American Chemical Society 2021. (d)–(f) TEM images for ZnAl-1, ZnAl-2, and ZnAl-3. Reproduced with permission from Ref. [32], © WILEY-VCH Verlag GmbH & Co. KGaA, Weinheim 2015. (g) and (h) TEM images of b-NiAl-LDH and f-NiAl-LDH. (i) HRTEM image of m-NiAl-LDH. (j) Selectivity yield of CH_4, CO, and H_2 in CO_2 on NiAl-LDH under irradiation above 400 nm. (k) NiAl-LDH under irradiation above 600 nm. Reproduced with permission from Ref. [119], © WILEY-VCH Verlag GmbH & Co. KGaA, Weinheim 2019. (l) Schematic illustration of the synthetic strategy for monolayer LDHs nanosheets. (m) CO_2 photoreduction performance. Reproduced with permission from Ref. [120], © Elsevier B.V. 2021.

LDH and g-C_3N_4 increased the separation efficiency of photogenerated electron and hole transfer between them. At the same time, the introduction of g-C_3N_4 changed the morphology of NiFe-LDH and reduced its agglomeration. It also improved the specific surface area of NiFe-LDH and provided more active sites for CO_2 reduction. The efficiency of NiFe-LDH/g-C_3N_4 to reduce CO_2 to produce CO and CH_4 was 3.57 and 4.25 times higher than that of NiFe-LDH, respectively. Zhao et al. synthesized a 2D/2D NiAl-LDH/$Ti_3C_2T_x$ core–shell like structure (Figs. 15(c)–15(e)), which promoted the transfer of electrons (Fig. 15(g)). The optimized sample showed a photocatalytic CO_2 reduction into CO with a rate of 2,128.46 μmol·g^{-1}·h^{-1} (Fig. 15(f)) [125].

In summary, LDHs have many advantages, such as unique layered structure, adjustable composition, the thickness of nanosheets, and various unsaturated active sites (such as metal vacancies and hydroxyl vacancies), which makes them one of the most promising photocatalytic materials in recent years.

3.5 Other 2D photocatalysts

MXene is a type of 2D inorganic layered material, which is composed of transition metal carbides, nitrides, or carbonitrides with several atomic layer thicknesses [180]. MXene can be obtained by etching the MAX phase, where A represents an element of the third or fourth main group, X is a carbon/nitrogen element, and M is a transition metal. Since the first discovery of MXene in 2011, it has attracted more and more attention. Until now, MXene has been widely studied in ion batteries [181] and supercapacitors [182, 183]. MXene has excellent photothermal properties, electrical conductivity, surface hydrophilicity, and abundant active sites on its surface, thus enabling a promising prospect in the field of photocatalysis [184].

As an excellent electron accepter center, MXene can effectively capture the electrons generated by the semiconductor and transfer them to nearby active sites for reductive reactions. For example, Yu's group ultrasonically peeled off 2D ultrathin Ti_3C_2 nanosheets (Fig. 16(a)) after etching Ti_3AlC_2, and then grew Bi_2WO_6 nanosheets *in situ* on the surface of Ti_3C_2 nanosheets to successfully fabricate a new type of 2D/2D heterojunction. The large specific surface area of Ti_3C_2/Bi_2WO_6 composite led to strong CO_2 adsorption, and the excellent electrical conductivity of Ti_3C_2 contributed to good charge separation in the bulk phase and surface charge separation of Ti_3C_2/Bi_2WO_6 composite. The photocatalytic results showed (Fig. 16(b)) that the CH_4 and CH_3OH total yield of Ti_3C_2/Bi_2WO_6 composite was 4.6 times that of pure Bi_2WO_6 nanosheets [136]. Que et al. explored the preparation of 2D $FAPbBr_3$ nanoplate combined with 2D Ti_3C_2 nanosheet to form a 2D/2D $FAPbBr_3/Ti_3C_2$ Schottky heterojunction. The introduction of Ti_3C_2 nanosheets provided

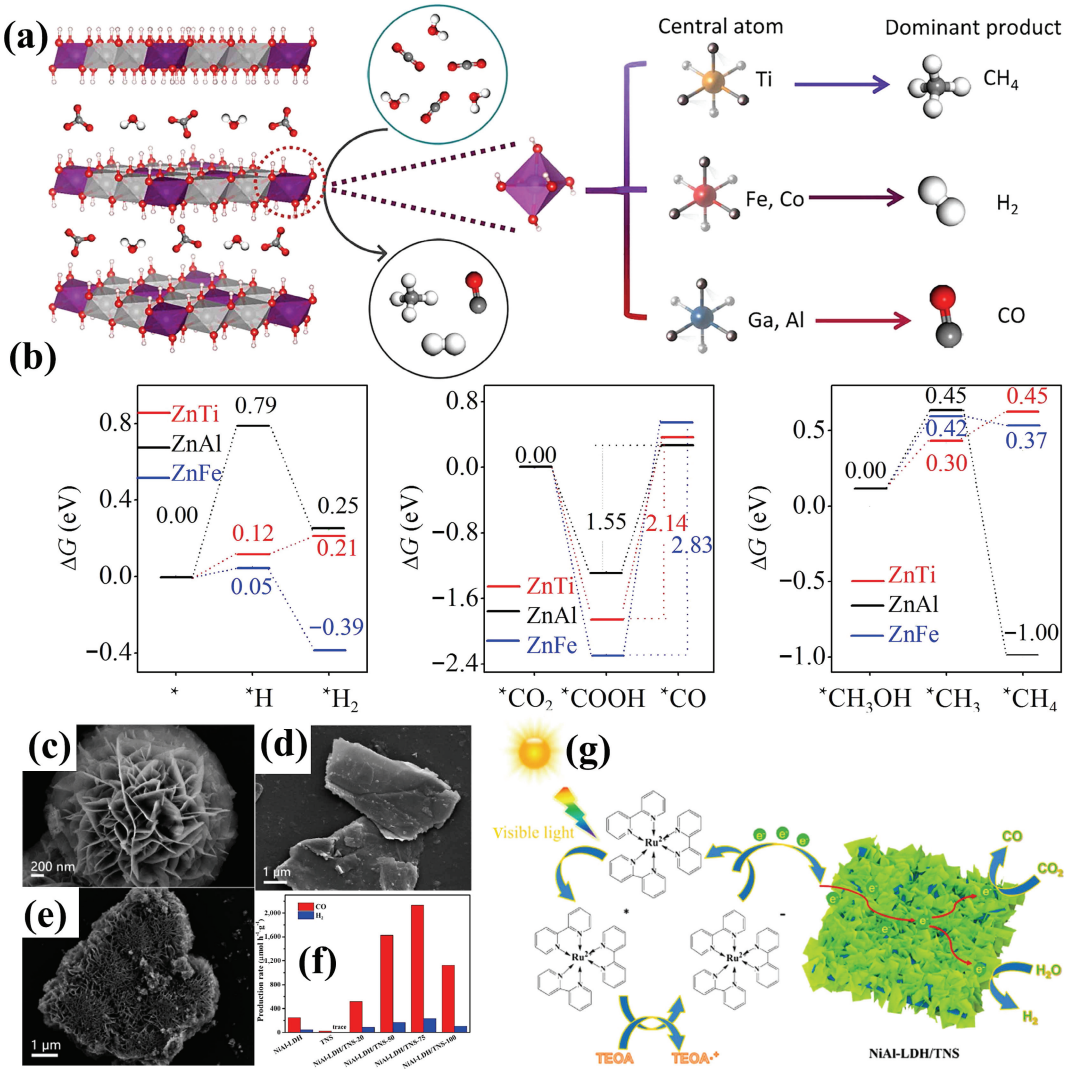

Figure 15 (a) Scheme showing CO_2 and H_2O photoreduction on the different ZnM-LDH photocatalysts. (b) Mechanism exploration of the CO_2 reduction selectivity over ZnM-LDHs. H_2 evolution, CO_2 reduction to CO, and CO_2 reduction to CH_4 involving a methanol intermediate over ZnTi-LDH, ZnAl-LDH, and ZnFe-LDH. Reproduced with permission from Ref. [122], © Science China Press 2020. (c)–(e) SEM images of pure NiAl-LDH, $Ti_3C_2T_x$ nanosheets, and NiAl-LDH/ $Ti_3C_2T_x$. (f) Photoreduction performance of NiAl-LDH/TNS composites with different TNS content in the samples. (g) Proposed mechanism of NiAl-LDH/TNS composite for the photocatalytic CO_2 reduction under visible-light irradiation. Reproduced with permission from Ref. [125], © American Chemical Society 2021.

the $FAPbBr_3/Ti_3C_2$ Schottky heterojunction with strong visible light absorption and more active sites. Meanwhile, large interfacial contact the composite material afforded sufficient channels for the transfer of photogenerated carriers. With ethyl acetate/deionization water as a sacrificial reagent, $FAPbBr_3/Ti_3C_2$ heterojunction showed a CO yield of 93.82 μmol·g^{-1}·h^{-1} [185]. In recent research, two kinds of Ti_3C_2-based heterojunctions (TiO_2/Ti_3C_2 [137] and Cu_2O/Ti_3C_2 [186]) were prepared, both of which exhibited a better photocatalytic CO_2 conversion performance than pristine TiO_2 and Cu_2O. Meanwhile, theoretical calculations also show that MXene is very suitable for energy conversion due to its unique photothermal properties. Attention is expected to be paid to the field of photocatalysis shortly.

As an emerging 2D semiconductor material, BP has stimulated people's research interest in recent years owing to adjustable bandgap (0.3–2.0 eV) and extremely high carrier mobility (~ 1,000 cm^2·V^{-1}·s^{-1}), as well as the rich reserves of P elements on the earth [187]. Xu's group successfully prepared a stable monolayer BP (Figs. 16(c) and 16(d)) with hydroxyl modification by liquid nitrogen-assisted stripping for the first time. The photocatalytic CO production rate of monolayer BP under visible light irradiation reached 112.6 μmol·g^{-1}·h^{-1}. Even under a 30-day cycle test under humid air conditions (at 90% humidity), the single layer of black phosphorus remained high catalytic activity. The authors concluded that the excellent durability of single-layer BP might be due to the introduction of hydroxyl groups occupying the position of a unique pair of electrons, which inhibited the oxidation of BP, thus keeping BP stable (Fig. 16(e)) [38]. Furthermore, this group had also prepared a BP/g-C_3N_4 heterojunction by combining g-C_3N_4, in which the 2D BP greatly promoted the separation of photo-generated holes and electrons. The CO generation rate of BP/g-C_3N_4 reached 187.7 μmol·g^{-1}·h^{-1}, which was much higher than that of monolayer BP [142]. However, the current preparation of single-layer BP was mainly obtained by liquid-phase stripping. The yield of BP synthesized by this method was low, and the dimensionality cannot be well controlled. Therefore, accurate and controllable preparation would be the future development direction for BP.

COFs as a new type of 2D material are generally a class of crystalline porous polymers that are covalently bound together by light elements (H, B, C, N, and O), which have a large specific surface area, and good thermal and chemical stability [188]. Due to their different organic structural units and adjustable pore size, they have attracted widespread attention in the field of catalysis [189, 190]. Liu et al. synthesized ultrathin imine-based 2D COFs nanosheets (Fig. 16(f)) by solvothermal method for photocatalytic

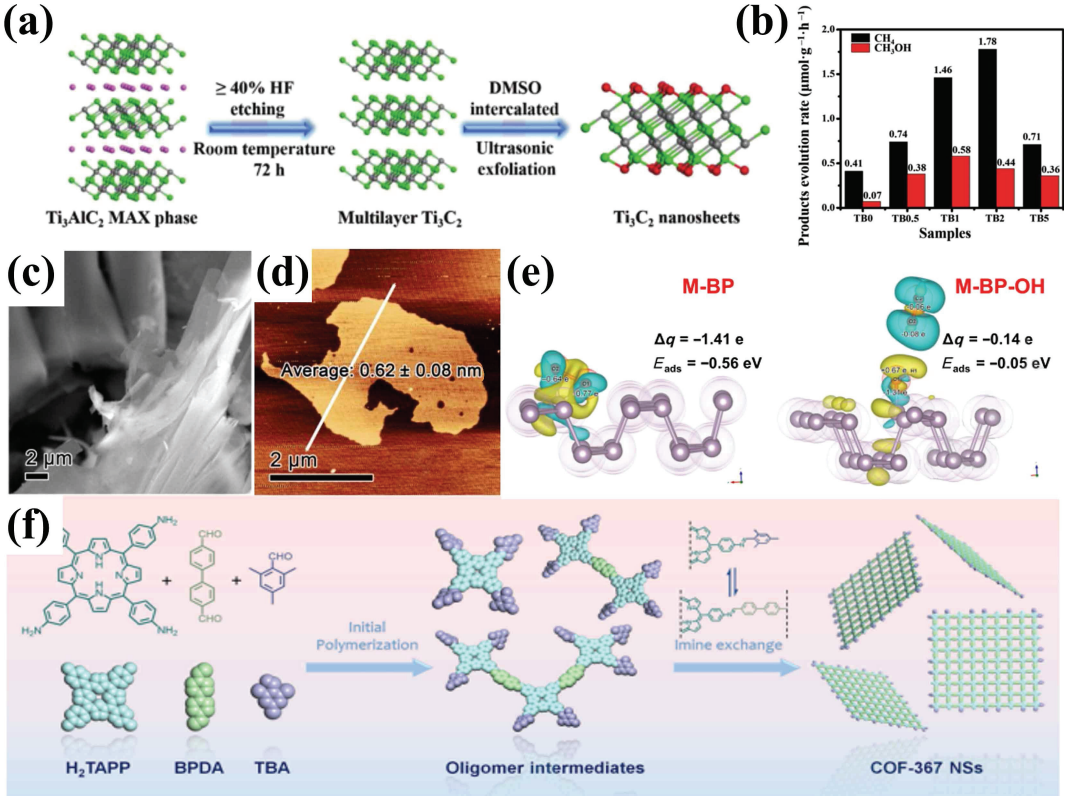

Figure 16 (a) Schematic illustration of the synthetic process of 2D ultrathin Ti_3C_2. (b) Photocatalytic activity of TB0, TB0.5, TB1, TB2, and TB5. Reproduced with permission from Ref. [136], © WILEY-VCH Verlag GmbH & Co. KGaA, Weinheim 2018. (c) SEM image of M-BP and (d) AFM image of M-BP. (e) Charge difference between O_2 adsorbed on the M-BP slab and the M-BP-OH slab. Reproduced with permission from Ref. [38], © Elsevier B.V. 2020. (f) Schematic Illustration of synthesis of the COF-367 NSs. Reproduced with permission from Ref. [144], © American Chemical Society 2019.

reduction of CO_2. The CO yield reached 10,162 μmol·g^{-1}·h^{-1} with a selectivity of ~ 100% [144]. In addition, Yang et al. reported a newly designed 2D COF with incorporated Re complex with enhanced light absorption and charge separation properties, enabling efficient CO yield with a selectivity of 98% under visible light [145]. These works not only demonstrated the potential of COFs in photocatalysis but also provided insight into the mechanistic origins of light-driven CO_2 reduction. So far, the research on COF photocatalytic reduction of CO_2 is still limited and only a few research papers have been reported. Therefore, COF is a material with great prospects and development space.

4 Conclusions and outlook

Photocatalytic CO_2 conversion into hydrocarbons can effectively solve energy shortages and weaken the greenhouse gas effect, which can further realize a globalized green life and promote the development of rational use of new energy technologies. In this review, we focus on the latest developments in the design and preparation of 2D materials (layered Bi-based photocatalysts, layered perovskites, TMDs, LDHs, MXene, BP, and COFs) for photocatalytic reduction of CO_2 in recent years.

Above all, the C=O bond energy is very high (about 750 kJ·mol^{-1}), which is hard to be broken. Thus, an efficient catalyst for photocatalytic conversion of CO_2 that can efficiently adsorb and activate CO_2 molecules to reduce its potential reduction barrier is needed. Meanwhile, only strong adsorption is not enough because the product needs to be desorbed in time after the product is formed. As CO_2 can theoretically be reduced to various carbon-containing products, the understanding of controlling the factors that affect the reduction selectivity should be furthered [191]. In Zhang's research [122], the controllable nature of cations between LDH layers has been used to obtain a conclusion that the incorporation of different cations is selective for specific products. However, most of the products of CO_2 are the two-electron product CO and the eight-electron product CH_4, which are relatively easy to obtain in kinetics. Other multi-electron products, such as CH_3OH, CH_3CH_2OH, CH_3CH_2CHO, and other hydrocarbons, are still relatively difficult to be obtained.

Due to their ultrathin structure and substantial specific surface area, 2D materials have been extensively researched in photocatalytic reduction of CO_2. The 2D structure design is suitable for bulk carriers to flow to the catalyst's surface to participate in the reaction. Early work on 2D materials has primarily concentrated on surface engineering, elemental (atomic) doping, heterojunction engineering, etc. (1) The most widely used techniques in surface engineering are the use of surface defects and surface ion grafting. Some typical examples include the development of oxygen vacancies on ultrathin $Bi_4Ti_3O_{12}$ nanosheets [77] and the surface halide ion modification of $Bi_2O_2(OH)NO_3$ [47] nanosheets reported by our group. As photogenerated electron or hole traps, vacancies on the surface and grafted ions will prolong the carrier lifetime and thereby increase the active sites. (2) When elements or atoms are doped into a photocatalyst, the energy band structure is altered, which stimulates more photogenerated electrons and holes. For examples, the C doped SnS_2 nanosheet [106] exhibits good visible light absorption and excellent photocatalytic properties. (3) The 2D materials are always in closer contact during the construction of heterojunction composites, increasing the interfacial carrier transport efficiency. Photocatalysis by heterojunctions generally produces strong oxidative and reductive electron–holes pairs, such as 2D/2D CoAlLa-LDH/ MXene [126] and 2D/2D black phosphorus/g-C_3N_4 [142]. In conclusion, these modification techniques aim to increase the separation and migration efficiency of carriers, resulting in a greater number of active sites.

2D photocatalytic materials require continuous time and effort

to optimize for the best performance and structure. However, to improve the efficiency of the experiment and to gain a deeper understanding, many researches use theoretical calculations to simulate materials' structures and evaluate their properties at present [192]. For instance, Chen et al. used calculations to reveal that oxygen vacancies can trap photogenerated charges on the surface of atomic layer thickness Bi_2O_3. The surface adsorption of CO_2 was promoted by the outlying electrons around the oxygen vacancies, which greatly enhanced the photocatalytic activity [193]. Additionally, our team has used comsol simulations to uncover that the dipole domains' direction in the ferroelectric Bi_3TiNbO_9 nanosheets gradually converges from the initial chaotic disorder after corona poling. Enhancement of spontaneous polarization generates a strong electric field to encourage carrier separation and migration [194]. And theoretical simulations are also able to analyze the Gibbs free energy of intermediates during the reduction of CO_2 on 2D materials [116, 122]. In general, theoretical calculations enable the analysis of material intrinsic structure, electronic structure, band gap, reaction energy potential, etc. And the combination of experiments and theory significantly advances our comprehension of the microscopic mechanisms underlying photocatalytic processes.

Considering the practical application of photocatalytic materials, it is impossible to bypass the realization of large-scale and high-quality production of 2D photocatalytic materials. At present, most photocatalysts are still in the essential research stage of the laboratory. If this problem cannot be solved to achieve industrial application, it will be nonsense to solve the energy shortage and create a green life. Thus, an efficient synthetic method should be developed. Besides, the long-term stability and recycling of photocatalysts is also a problem worthy of in-depth consideration, which should be paid more attention to in future work.

In short, developing efficient, stable, and low-cost 2D photocatalysts with ideal selectivity is the ultimate objective for actual application for photocatalytic CO_2 reduction. In addition to using a wealth of experiments to explore, more can still borrow theoretical calculations to simulate a new type of high-efficiency photocatalyst and then prove through experiments that this will shorten the time, workforce, and financial resources. With the development of science and technology, the design and application of 2D will become more and more mature (Fig. 17).

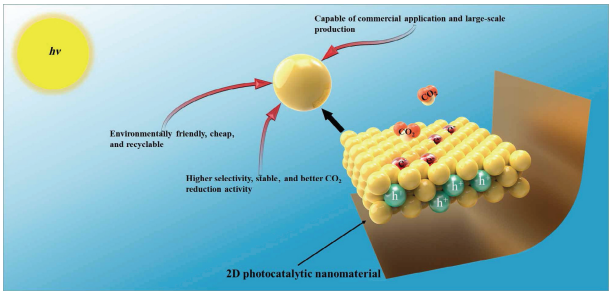

Figure 17 Schematic illustration for the future development of 2D materials.

Acknowledgments

This work was jointly supported by the National Natural Science Foundations of China (Nos. 52272244 and 51972288) and the Fundamental Research Funds for the Central Universities (No. 2652022202).

References

[1] Almeida, R. M.; Shi, Q. R.; Gomes-Selman, J. M.; Wu, X. J.; Xue, Y. X.; Angarita, H.; Barros, N.; Forsberg, B. R.; García-Villacorta, R.; Hamilton, S. K. et al. Reducing greenhouse gas emissions of Amazon hydropower with strategic dam planning. *Nat. Commun.* **2019**, *10*, 4281.

[2] Tyrrell, T. Chance played a role in determining whether Earth stayed habitable. *Commun. Earth Environ.* **2020**, *1*, 61.

[3] Sorrell, S.; Gatersleben, B.; Druckman, A. The limits of energy sufficiency: A review of the evidence for rebound effects and negative spillovers from behavioural change. *Energy Res. Soc. Sci.* **2020**, *64*, 101439.

[4] Centi, G.; Perathoner, S. Towards solar fuels from water and CO_2. *ChemSusChem* **2010**, *3*, 195–208.

[5] Fu, J. W.; Zhu, B. C.; Jiang, C. J.; Cheng, B.; You, W.; Yu, J. G. Hierarchical porous O-doped g-C_3N_4 with enhanced photocatalytic CO_2 reduction activity. *Small* **2017**, *13*, 1603938.

[6] Jin, J. R.; He, T. Facile synthesis of Bi_2S_3 nanoribbons for photocatalytic reduction of CO_2 into CH_3OH. *Appl. Surf. Sci.* **2017**, *394*, 364–370.

[7] Mao, J.; Li, K.; Peng, T. Y. Recent advances in the photocatalytic CO_2 reduction over semiconductors. *Catal. Sci. Technol.* **2013**, *3*, 2481–2498.

[8] Yin, G. H.; Bi, Q. Y.; Zhao, W.; Xu, J. J.; Lin, T. Q.; Huang, F. Q. Efficient conversion of CO_2 to methane photocatalyzed by conductive black titania. *ChemCatChem* **2017**, *9*, 4389–4396.

[9] Álvarez, A.; Borges, M.; Corral-Pérez, J. J.; Olcina, J. G.; Hu, L. J.; Cornu, D.; Huang, R.; Stoian, D.; Urakawa, A. CO_2 activation over catalytic surfaces. *ChemPhysChem* **2017**, *18*, 3135–3141.

[10] White, J. L.; Baruch, M. F.; Pander, J. E.; Hu, Y.; Fortmeyer, I. C.; Park, J. E.; Zhang, T.; Liao, K.; Gu, J.; Yan, Y. et al. Light-driven heterogeneous reduction of carbon dioxide: Photocatalysts and photoelectrodes. *Chem. Rev.* **2015**, *115*, 12888–12935.

[11] Sun, Z. Y.; Talreja, N.; Tao, H. C.; Texter, J.; Muhler, M.; Strunk, J.; Chen, J. F. Catalysis of carbon dioxide photoreduction on nanosheets: Fundamentals and challenges. *Angew. Chem., Int. Ed.* **2018**, *57*, 7610–7627.

[12] He, J.; Wang, X. D.; Jin, S. B.; Liu, Z. Q.; Zhu, M. S. 2D metal-free heterostructure of covalent triazine framework/g-C_3N_4 for enhanced photocatalytic CO_2 reduction with high selectivity. *Chin. J. Catal.* **2022**, *43*, 1306–1315.

[13] Chang, X. X.; Wang, T.; Gong, J. L. CO_2 photo-reduction: Insights into CO_2 activation and reaction on surfaces of photocatalysts. *Energy Environ. Sci.* **2016**, *9*, 2177–2196.

[14] Xia, P. F.; Zhu, B. C.; Yu, J. G.; Cao, S. W.; Jaroniec, M. Ultra-thin nanosheet assemblies of graphitic carbon nitride for enhanced photocatalytic CO_2 reduction. *J. Mater. Chem. A* **2017**, *5*, 3230–3238.

[15] Zou, C. C.; Li, Q. Q.; Hua, Y. Y.; Zhou, B. H.; Duan, J. G.; Jin, W. Q. Mechanical synthesis of COF nanosheet cluster and its mixed matrix membrane for efficient CO_2 removal. *ACS Appl. Mater. Interfaces* **2017**, *9*, 29093–29100.

[16] Habisreutinger, S. N.; Schmidt-Mende, L.; Stolarczyk, J. K. Photocatalytic reduction of CO_2 on TiO_2 and other semiconductors. *Angew. Chem., Int. Ed.* **2013**, *52*, 7372–7408.

[17] Kong, T. T.; Jiang, Y. W.; Xiong, Y. J. Photocatalytic CO_2 conversion: What can we learn from conventional CO_x hydrogenation? *Chem. Soc. Rev.* **2020**, *49*, 6579–6591.

[18] Inoue, T.; Fujishima, A.; Konishi, S.; Honda, K. Photoelectrocatalytic reduction of carbon dioxide in aqueous suspensions of semiconductor powders. *Nature* **1979**, *277*, 637–638.

[19] Yue, X. Y.; Cheng, L.; Fan, J. J.; Xiang, Q. J. 2D/2D $BiVO_4$/$CsPbBr_3$ S-scheme heterojunction for photocatalytic CO_2 reduction: Insights into structure regulation and fermi level modulation. *Appl. Catal. B* **2022**, *304*, 120979.

[20] Xue, J. Y.; Yu, Y.; Yang, C.; Zhang, K. F.; Zhan, X. W.; Song, J. M.; Gui, J. J.; Li, Y. K.; Jin, X.; Gao, S. et al. Developing atomically thin $Li_{1.81}H_{0.19}Ti_2O_5{\cdot}2H_2O$ nanosheets for selective photocatalytic CO_2 reduction to CO. *Langmuir* **2022**, *38*, 523–530.

[21] Li, L.; Han, Q. T.; Tang, L. Q.; Zhang, Y.; Li, P.; Zhou, Y.; Zou, Z. G. Flux synthesis of regular Bi_4TaO_8Cl square nanoplates exhibiting dominant exposure surfaces of {001} crystal facets for

photocatalytic reduction of CO_2 to methane. *Nanoscale* **2018**, *10*, 1905–1911.

[22] Liu, T. Y.; Hao, L.; Bai, L. Q.; Liu, J. G.; Zhang, Y. H.; Tian, N.; Huang, H. W. Z-scheme junction $Bi_2O_2(NO_3)(OH)$/g-C_3N_4 for promoting CO_2 photoreduction. *Chem. Eng. J.* **2022**, *429*, 132268.

[23] Yu, H. J.; Li, J. Y.; Zhang, Y. H.; Yang, S. Q.; Han, K. L.; Dong, F.; Ma, T. Y.; Huang, H. W. Three-in-one oxygen vacancies: Whole visible-spectrum absorption, efficient charge separation, and surface site activation for robust CO_2 photoreduction. *Angew. Chem., Int. Ed.* **2019**, *58*, 3880–3884.

[24] Si, J. J.; Yu, J. Q.; Shen, Y.; Zeng, M. Q.; Fu, L. Elemental 2D materials: Progress and perspectives toward unconventional structures. *Small Struct.* **2020**, *2*, 2000101.

[25] Cai, X. K.; Luo, Y. T.; Liu, B. L.; Cheng, H. M. Preparation of 2D material dispersions and their applications. *Chem. Soc. Rev.* **2018**, *47*, 6224–6266.

[26] Zhao, W. F.; Wu, F. R.; Wu, H.; Chen, G. H. Preparation of colloidal dispersions of graphene sheets in organic solvents by using ball milling. *J. Nanomater.* **2010**, *2010*, 528235.

[27] Xue, T. T.; Zhang, X. C.; Zhang, C. M.; Li, R.; Liu, J. X.; Wang, Y. F.; Wang, Y. W.; Fan, C. M. *In-situ* electrochemical-ion-exchange synthesis of novel $Bi_{12}SiO_{20}$/BiOBr composite film from Bi plate for enhanced photocatalytic CO_2 reduction activity. *Mater. Lett.* **2020**, *274*, 127990.

[28] Geim, A. K.; Novoselov, K. S. The rise of graphene. *Nat. Mater.* **2007**, *6*, 183–191.

[29] Naguib, M.; Kurtoglu, M.; Presser, V.; Lu, J.; Niu, J. J.; Heon, M.; Hultman, L.; Gogotsi, Y.; Barsoum, M. W. Two-dimensional nanocrystals produced by exfoliation of Ti_3AlC_2. *Adv. Mater.* **2011**, *23*, 4248–4253.

[30] Zhang, Y. Z.; Yao, D. Z.; Xia, B. Q.; Xu, H. L.; Tang, Y. H.; Davey, K.; Ran, J. R.; Qiao, S. Z. ReS_2 nanosheets with *in situ* formed sulfur vacancies for efficient and highly selective photocatalytic CO_2 reduction. *Small Sci.* **2021**, *1*, 2000052.

[31] Dong, R. H.; Zhang, T.; Feng, X. L. Interface-assisted synthesis of 2D materials: Trend and challenges. *Chem. Rev.* **2018**, *118*, 6189–6235.

[32] Zhao, Y. F.; Chen, G. B.; Bian, T.; Zhou, C.; Waterhouse, G. I. N.; Wu, L. Z.; Tung, C. H.; Smith, L. J.; O'Hare, D.; Zhang, T. R. Defect-rich ultrathin ZnAl-layered double hydroxide nanosheets for efficient photoreduction of CO_2 to CO with water. *Adv. Mater.* **2015**, *27*, 7824–7831.

[33] Tang, L. Q.; Chen, R. T.; Meng, X. G.; Lv, B. H.; Fan, F. T.; Ye, J. H.; Wang, X. Y.; Zhou, Y.; Li, C.; Zou, Z. G. Unique homo-heterojunction synergistic system consisting of stacked BiOCl nanoplate/Zn-Cr layered double hydroxide nanosheets promoting photocatalytic conversion of CO_2 into solar fuels. *Chem. Commun.* **2018**, *54*, 5126–5129.

[34] Duan, X. Y.; Chen, G. D.; Guo, L. A.; Zhu, Y. Z.; Ye, H. G.; Wu, Y. L. A template-free CVD route to synthesize hierarchical porous ZnO films. *Superlattices Microstruct.* **2015**, *88*, 501–507.

[35] Meier, A. J.; Garg, A.; Sutter, B.; Kuhn, J. N.; Bhethanabotla, V. R. MoS_2 nanoflowers as a gateway for solar-driven CO_2 photoreduction. *ACS Sustain. Chem. Eng.* **2019**, *7*, 265–275.

[36] Park, S.; Song, H. J.; Lee, C. W.; Hwang, S. W.; Cho, I. S. Enhanced photocatalytic activity of ultrathin $Ba_5Nb_4O_{15}$ two-dimensional nanosheets. *ACS Appl. Mater. Interfaces* **2015**, *7*, 21860–21867.

[37] Ali, A.; Oh, W. C. Preparation of nanowire like WSe_2-graphene nanocomposite for photocatalytic reduction of CO_2 into CH_3OH with the presence of sacrificial agents. *Sci. Rep.* **2017**, *7*, 1867.

[38] Zhu, X. W.; Huang, S. Q.; Yu, Q.; She, Y. B.; Yang, J. M.; Zhou, G. L.; Li, Q. D.; She, X. J.; Deng, J. J.; Li, H. M. et al. *In-situ* hydroxyl modification of monolayer black phosphorus for stable photocatalytic carbon dioxide conversion. *Appl. Catal. B: Environ.* **2020**, *269*, 118760.

[39] Zheng, Y. N.; Yin, X. H.; Jiang, Y.; Bai, J. S.; Tang, Y.; Shen, Y. L.; Zhang, M. Nano Ag-decorated MoS_2 nanosheets from 1T to 2H phase conversion for photocatalytically reducing CO_2 to methanol. *Energy Technol.* **2019**, *7*, 1900582.

[40] Kumar, S.; Isaacs, M. A.; Trofimovaite, R.; Durndell, L.; Parlett, C. M. A.; Douthwaite, R. E.; Coulson, B.; Cockett, M. C. R.; Wilson, K.; Lee, A. F. P25@CoAl layered double hydroxide heterojunction nanocomposites for CO_2 photocatalytic reduction. *Appl. Catal. B: Environ.* **2017**, *209*, 394–404.

[41] Jiao, W. Y.; Xie, Y.; He, F.; Wang, K. Y.; Ling, Y.; Hu, Y. Y.; Wang, J. L.; Ye, H.; Wu, J.; Hou, Y. A visible light-response flower-like La-doped BiOBr nanosheets with enhanced performance for photoreducing CO_2 to CH_3OH. *Chem. Eng. J.* **2021**, *418*, 129286.

[42] Hong, J. D.; Zhang, W.; Wang, Y. B.; Zhou, T. H.; Xu, R. Photocatalytic reduction of carbon dioxide over self-assembled carbon nitride and layered double hydroxide: The role of carbon dioxide enrichment. *ChemCatChem* **2014**, *6*, 2315–2321.

[43] Kong, X. Y.; Lee, W. Q.; Mohamed, A. R.; Chai, S. P. Effective steering of charge flow through synergistic inducing oxygen vacancy defects and p-n heterojunctions in 2D/2D surface-engineered Bi_2WO_6/BiOI cascade: Towards superior photocatalytic CO_2 reduction activity. *Chem. Eng. J.* **2019**, *372*, 1183–1193.

[44] Wang, L.; Bahnemann, D. W.; Bian, L.; Dong, G. H.; Zhao, J.; Wang, C. Y. Two-dimensional layered zinc silicate nanosheets with excellent photocatalytic performance for organic pollutant degradation and CO_2 conversion. *Angew. Chem., Int. Ed.* **2019**, *58*, 8103–8108.

[45] Jiang, H. Y.; Katsumata, K. I.; Hong, J.; Yamaguchi, A.; Nakata, K.; Terashima, C.; Matsushita, N.; Miyauchi, M.; Fujishima, A. Photocatalytic reduction of CO_2 on Cu_2O-loaded Zn-Cr layered double hydroxides. *Appl. Catal. B: Environ.* **2018**, *224*, 783–790.

[46] Zhang, T.; Maihemllti, M.; Okitsu, K.; Talifur, D.; Tursun, Y.; Abulizi, A. *In situ* self-assembled S-scheme BiOBr/pCN hybrid with enhanced photocatalytic activity for organic pollutant degradation and CO_2 reduction. *Appl. Surf. Sci.* **2021**, *556*, 149828.

[47] Hao, L.; Kang, L.; Huang, H. W.; Ye, L. Q.; Han, K. L.; Yang, S. Q.; Yu, H. J.; Batmunkh, M.; Zhang, Y. H.; Ma, T. Y. Surface-halogenation-induced atomic-site activation and local charge separation for superb CO_2 photoreduction. *Adv. Mater.* **2019**, *31*, 1900546.

[48] Kawamura, S.; Puscasu, M. C.; Yoshida, Y.; Izumi, Y.; Carja, G. Tailoring assemblies of plasmonic silver/gold and zinc-gallium layered double hydroxides for photocatalytic conversion of carbon dioxide using UV–visible light. *Appl. Catal. A: Gen.* **2015**, *504*, 238–247.

[49] Li, K.; Liang, Y. J.; Yang, J.; Gao, Q.; Zhu, Y. L.; Liu, S. Q.; Xu, R.; Wu, X. Y. Controllable synthesis of {001} facet dependent foursquare BiOCl nanosheets: A high efficiency photocatalyst for degradation of methyl orange. *J. Alloys Compd.* **2017**, *695*, 238–249.

[50] Jiang, J.; Zhao, K.; Xiao, X. Y.; Zhang, L. Z. Synthesis and facet-dependent photoreactivity of BiOCl single-crystalline nanosheets. *J. Am. Chem. Soc.* **2012**, *134*, 4473–4476.

[51] Zhang, K. L.; Liu, C. M.; Huang, F. Q.; Zheng, C.; Wang, W. D. Study of the electronic structure and photocatalytic activity of the BiOCl photocatalyst. *Appl. Catal. B: Environ.* **2006**, *68*, 125–129.

[52] Ma, Z. Y.; Li, P. H.; Ye, L. Q.; Zhou, Y.; Su, F. Y.; Ding, C. H.; Xie, H. Q.; Bai, Y.; Wong, P. K. Oxygen vacancies induced exciton dissociation of flexible BiOCl nanosheets for effective photocatalytic CO_2 conversion. *J. Mater. Chem. A* **2017**, *5*, 24995–25004.

[53] Kong, X. Y.; Lee, W. P. C.; Ong, W. J.; Chai, S. P.; Mohamed, A. R. Oxygen-deficient BiOBr as a highly stable photocatalyst for efficient CO_2 reduction into renewable carbon-neutral fuels. *ChemCatChem* **2016**, *8*, 3074–3081.

[54] Ye, L. Q.; Jin, X. L.; Ji, X. X.; Liu, C.; Su, Y. R.; Xie, H. Q.; Liu, C. Facet-dependent photocatalytic reduction of CO_2 on BiOI nanosheets. *Chem. Eng. J.* **2016**, *291*, 39–46.

[55] Jin, J. R.; Wang, Y. J.; He, T. Preparation of thickness-tunable BiOCl nanosheets with high photocatalytic activity for photoreduction of CO_2. *RSC Adv.* **2015**, *5*, 100244–100250.

[56] Wu, S. Q.; Wang, J. B.; Li, Q. C.; Huang, Z. A.; Rao, Z. Q.; Zhou, Y. Bi/BiOCl nanosheets enriched with oxygen vacancies to enhance photocatalytic CO_2 reduction. *Trans. Tianjin Univ.* **2021**, *27*, 155–164.

[57] Kong, X. Y.; Ng, B. J.; Tan, K. H.; Chen, X. F.; Wang, H. T.; Mohamed, A. R.; Chai, S. P. Simultaneous generation of oxygen vacancies on ultrathin BiOBr nanosheets during visible-light-driven

CO_2 photoreduction evoked superior activity and long-term stability. *Catal. Today* **2018**, *314*, 20–27.

[58] Di, J.; Chen, C.; Zhu, C.; Song, P.; Xiong, J.; Ji, M. X.; Zhou, J. D.; Fu, Q. D.; Xu, M. Z.; Hao, W. et al. Bismuth vacancy-tuned bismuth oxybromide ultrathin nanosheets toward photocatalytic CO_2 reduction. *ACS Appl. Mater. Interfaces* **2019**, *11*, 30786–30792.

[59] Wu, J.; Xie, Y.; Ling, Y.; Si, J. C.; Li, X.; Wang, J. L.; Ye, H.; Zhao, J. S.; Li, S. Q.; Zhao, Q. D. et al. One-step synthesis and Gd^{3+} decoration of BiOBr microspheres consisting of nanosheets toward improving photocatalytic reduction of CO_2 into hydrocarbon fuel. *Chem. Eng. J.* **2020**, *400*, 125944.

[60] Xu, Y. X.; Jin, X. L.; Ge, T.; Xie, H. Q.; Sun, R. X.; Su, F. Y.; Li, X.; Ye, L. Q. Realizing efficient CO_2 photoreduction in Bi_3O_4Cl: Constructing van der Waals heterostructure with g-C_3N_4. *Chem. Eng. J.* **2021**, *409*, 128178.

[61] Jin, X. L.; Lv, C. D.; Zhou, X.; Ye, L. Q.; Xie, H. Q.; Liu, Y.; Su, H.; Zhang, B.; Chen, G. Oxygen vacancy engineering of $Bi_{24}O_{31}Cl_{10}$ for boosted photocatalytic CO_2 conversion. *ChemSusChem* **2019**, *12*, 2740–2747.

[62] Quan, Y.; Wang, B.; Liu, G. P.; Li, H. M.; Xia, J. X. Carbonized polymer dots modified ultrathin $Bi_{12}O_{17}Cl_2$ nanosheets Z-scheme heterojunction for robust CO_2 photoreduction. *Chem. Eng. Sci.* **2021**, *232*, 116338.

[63] Bai, Y.; Yang, P.; Wang, L.; Yang, B.; Xie, H. Q.; Zhou, Y.; Ye, L. Q. Ultrathin $Bi_4O_5Br_2$ nanosheets for selective photocatalytic CO_2 conversion into CO. *Chem. Eng. J.* **2019**, *360*, 473–482.

[64] Di, J.; Chen, C.; Yang, S. Z.; Chen, S. M.; Duan, M. L.; Xiong, J.; Zhu, C.; Long, R.; Hao, W.; Chi, Z. et al. Isolated single atom cobalt in Bi_3O_4Br atomic layers to trigger efficient CO_2 photoreduction. *Nat. Commun.* **2019**, *10*, 2840.

[65] Ding, C. H.; Ye, L. Q.; Zhao, Q.; Zhong, Z. G.; Liu, K. C.; Xie, H. Q.; Bao, K. Y.; Zhang, X. G.; Huang, Z. X. Synthesis of $Bi_xO_yI_z$ from molecular precursor and selective photoreduction of CO_2 into CO. *J. CO_2 Util.* **2016**, *14*, 135–142.

[66] Bai, Y.; Yang, P.; Wang, P. Q.; Xie, H. Q.; Dang, H. F.; Ye, L. Q. Semimetal bismuth mediated UV–vis–IR driven photo-thermocatalysis of $Bi_4O_5I_2$ for carbon dioxide to chemical energy. *J. CO_2 Util.* **2018**, *23*, 51–60.

[67] Tu, S. C.; Guo, Y. X.; Zhang, Y. H.; Hu, C.; Zhang, T. R.; Ma, T. Y.; Huang, H. W. Piezocatalysis and piezo-photocatalysis: Catalysts classification and modification strategy, reaction mechanism, and practical application. *Adv. Funct. Mater.* **2020**, *30*, 2005158.

[68] Ribeiro, C. S.; Lansarin, M. A. Enhanced photocatalytic activity of Bi_2WO_6 with PVP addition for CO_2 reduction into ethanol under visible light. *Environ. Sci. Pollut. Res. Int.* **2021**, *28*, 23667–23674.

[69] Kong, X. Y.; Tong, T.; Ng, B. J.; Low, J.; Zeng, T. H.; Mohamed, A. R.; Yu, J. G.; Chai, S. P. Topotactic transformation of bismuth oxybromide into bismuth tungstate: Bandgap modulation of single-crystalline {001}-faceted nanosheets for enhanced photocatalytic CO_2 reduction. *ACS Appl. Mater. Interfaces* **2020**, *12*, 26991–27000.

[70] Li, Q. D.; Zhu, X. W.; Yang, J. M.; Yu, Q.; Zhu, X. L.; Chu, J. Y.; Du, Y. S.; Wang, C. T.; Hua, Y. J.; Li, H. M. et al. Plasma treated Bi_2WO_6 ultrathin nanosheets with oxygen vacancies for improved photocatalytic CO_2 reduction. *Inorg. Chem. Front.* **2020**, *7*, 597–602.

[71] Li, H.; Zhang, J. C.; Yu, J. G.; Cao, S. W. Ultra-thin carbon-doped Bi_2WO_6 nanosheets for enhanced photocatalytic CO_2 reduction. *Trans. Tianjin Univ.* **2021**, *27*, 338–347.

[72] Li, Y. Y.; Fan, J. S.; Tan, R. Q.; Yao, H. C.; Peng, Y.; Liu, Q. C.; Li, Z. J. Selective photocatalytic reduction of CO_2 to CH_4 modulated by chloride modification on Bi_2WO_6 nanosheets. *ACS Appl. Mater. Interfaces* **2020**, *12*, 54507–54516.

[73] Jiang, Y.; Chen, H. Y.; Li, J. Y.; Liao, J. F.; Zhang, H. H.; Wang, X. D.; Kuang, D. B. Z-scheme 2D/2D heterojunction of $CsPbBr_3/Bi_2WO_6$ for improved photocatalytic CO_2 reduction. *Adv. Funct. Mater.* **2020**, *30*, 2004293.

[74] Zheng, Y.; Zhou, T. F.; Zhao, X. D.; Pang, W. K.; Gao, H.; Li, S. A.; Zhou, Z.; Liu, H. K.; Guo, Z. P. Atomic interface engineering and electric-field effect in ultrathin Bi_2MoO_6 nanosheets for superior lithium ion storage. *Adv. Mater.* **2017**, *29*, 1700396.

[75] Li, S. G.; Bai, L. Q.; Ji, N.; Yu, S. X.; Lin, S.; Tian, N.; Huang, H. W. Ferroelectric polarization and thin-layered structure synergistically promoting CO_2 photoreduction of Bi_2MoO_6. *J. Mater. Chem. A* **2020**, *8*, 9268–9277.

[76] Liu, L. Z.; Huang, H. W.; Chen, F.; Yu, H. J.; Tian, N.; Zhang, Y. H.; Zhang, T. R. Cooperation of oxygen vacancies and 2D ultrathin structure promoting CO_2 photoreduction performance of $Bi_4Ti_3O_{12}$. *Sci. Bull.* **2020**, *65*, 934–943.

[77] Liu, L. Z.; Huang, H. W.; Chen, Z. S.; Yu, H. J.; Wang, K. Y.; Huang, J. D.; Yu, H.; Zhang, Y. H. Synergistic polarization engineering on bulk and surface for boosting CO_2 photoreduction. *Angew. Chem., Int. Ed.* **2021**, *60*, 18303–18308.

[78] Wang, X. Y.; Wang, Y. S.; Gao, M. C.; Shen, J. N.; Pu, X. P.; Zhang, Z. Z.; Lin, H. X.; Wang, X. X. $BiVO_4/Bi_4Ti_3O_{12}$ heterojunction enabling efficient photocatalytic reduction of CO_2 with H_2O to CH_3OH and CO. *Appl. Catal. B: Environ.* **2020**, *270*, 118876.

[79] Huang, H. W.; Tu, S. C.; Zeng, C.; Zhang, T. R.; Reshak, A. H.; Zhang, Y. H. Macroscopic polarization enhancement promoting photo- and piezoelectric-induced charge separation and molecular oxygen activation. *Angew. Chem., Int. Ed.* **2017**, *56*, 11860–11864.

[80] Chen, F.; Huang, H. W.; Ye, L. Q.; Zhang, T. R.; Zhang, Y. H.; Han, X. P.; Ma, T. Y. Thickness-dependent facet junction control of layered $BiOIO_3$ single crystals for highly efficient CO_2 photoreduction. *Adv. Funct. Mater.* **2018**, *28*, 1804284.

[81] Chen, F.; Ma, Z. Y.; Ye, L. Q.; Ma, T. Y.; Zhang, T. R.; Zhang, Y. H.; Huang, H. W. Macroscopic spontaneous polarization and surface oxygen vacancies collaboratively boosting CO_2 photoreduction on $BiOIO_3$ single crystals. *Adv. Mater.* **2020**, *32*, 1908350.

[82] Zou, J. S.; Wu, J. Experimental study on the photocatalytic reduction of CO_2 by $Fe_2O_3/BiOIO_3$ composite photocatalyst. *IOP Conf. Ser.: Earth Environ. Sci.* **2021**, *770*, 012033.

[83] Xu, Y.; You, Y.; Huang, H. W.; Guo, Y. X.; Zhang, Y. H. Bi_4NbO_8Cl {001} nanosheets coupled with g-C_3N_4 as 2D/2D heterojunction for photocatalytic degradation and CO_2 reduction. *J. Hazard. Mater.* **2020**, *381*, 121159.

[84] Guo, L. N.; You, Y.; Huang, H. W.; Tian, N.; Ma, T. Y.; Zhang, Y. H. Z-scheme g-$C_3N_4/Bi_2O_2[BO_2(OH)]$ heterojunction for enhanced photocatalytic CO_2 reduction. *J. Colloid Interface Sci.* **2020**, *568*, 139–147.

[85] Ye, L. Q.; Jin, X. L.; Liu, C.; Ding, C. H.; Xie, H. Q.; Chu, K. H.; Wong, P. K. Thickness-ultrathin and bismuth-rich strategies for BiOBr to enhance photoreduction of CO_2 into solar fuels. *Appl. Catal. B: Environ.* **2016**, *187*, 281–290.

[86] Lu, M. F.; Li, Q. Q.; Zhang, C. L.; Fan, X. X.; Li, L.; Dong, Y. M.; Chen, G. Q.; Shi, H. F. Remarkable photocatalytic activity enhancement of CO_2 conversion over 2D/2D g-$C_3N_4/BiVO_4$ Z-scheme heterojunction promoted by efficient interfacial charge transfer. *Carbon* **2020**, *160*, 342–352.

[87] Oliveira, J. A.; Torres, J. A.; Gonçalves, R. V.; Ribeiro, C.; Nogueira, F. G. E.; Ruotolo, L. A. M. Photocatalytic CO_2 reduction over Nb_2O_5/basic bismuth nitrate nanocomposites. *Mater. Res. Bull.* **2021**, *133*, 111073.

[88] Xie, Z. K.; Xu, Y. Y.; Li, D.; Meng, S. C.; Chen, M.; Jiang, D. L. Covalently bonded Bi_2O_3 nanosheet/Bi_2WO_6 network heterostructures for efficient photocatalytic CO_2 reduction. *ACS Appl. Energy Mater.* **2020**, *3*, 12194–12203.

[89] Miao, Y. F.; Guo, R. T.; Gu, J. W.; Liu, Y. Z.; Wu, G. L.; Duan, C. P.; Pan, W. G. Z-scheme $Bi/Bi_2O_2CO_3$/layered double-hydroxide nanosheet heterojunctions for photocatalytic CO_2 reduction under visible light. *ACS Appl. Nano Mater.* **2021**, *4*, 4902–4911.

[90] Yan, J. Y.; Wang, C. H.; Ma, H.; Li, Y. Y.; Liu, Y. C.; Suzuki, N.; Terashima, C.; Fujishima, A.; Zhang, X. T. Photothermal synergic enhancement of direct Z-scheme behavior of $Bi_4TaO_8Cl/W_{18}O_{49}$ heterostructure for CO_2 reduction. *Appl. Catal. B: Environ.* **2020**, *268*, 118401.

[91] Kong, X. Y.; Tan, W. L.; Ng, B. J.; Chai, S. P.; Mohamed, A. R. Harnessing Vis-NIR broad spectrum for photocatalytic CO_2 reduction over carbon quantum dots-decorated ultrathin Bi_2WO_6 nanosheets. *Nano Res.* **2017**, *10*, 1720–1731.

[92] Oshima, T.; Ichibha, T.; Qin, K. S.; Muraoka, K.; Vequizo, J. J. M.; Hibino, K.; Kuriki, R.; Yamashita, S.; Hongo, K.; Uchiyama, T. et al. Undoped layered perovskite oxynitride $Li_2LaTa_2O_6N$ for photocatalytic CO_2 reduction with visible light. *Angew. Chem., Int. Ed.* **2018**, *57*, 8154–8158.

[93] Huang, H. H.; Liu, X. Q.; Li, F.; He, Q. Y.; Ji, H. B.; Yu, C. L. *In situ* construction of a 2D $CoTiO_3$/g-C_3N_4 photocatalyst with an S-scheme heterojunction and its excellent performance for CO_2 reduction. *Sustainable Energy Fuels* **2022**, *6*, 4903–4915.

[94] Lin, N. S.; Lin, Y.; Qian, X. J.; Wang, X. X.; Su, W. Y. Construction of a 2D/2D WO_3/$LaTiO_2N$ direct Z-scheme photocatalyst for enhanced CO_2 reduction performance under visible light. *ACS Sustain. Chem. Eng.* **2021**, *9*, 13686–13694.

[95] Tu, S. C.; Zhang, Y. H.; Reshak, A. H.; Auluck, S.; Ye, L. Q.; Han, X. P.; Ma, T. Y.; Huang, H. W. Ferroelectric polarization promoted bulk charge separation for highly efficient CO_2 photoreduction of $SrBi_4Ti_4O_{15}$. *Nano Energy* **2019**, *56*, 840–850.

[96] Kwak, B. S.; Do, J. Y.; Park, N. K.; Kang, M. Surface modification of layered perovskite Sr_2TiO_4 for improved CO_2 photoreduction with H_2O to CH_4. *Sci. Rep.* **2017**, *7*, 16370.

[97] Wang, Y. H.; Liu, M.; Chen, W.; Mao, L. Q.; Shangguan, W. F. Ag loaded on layered perovskite $H_2SrTa_2O_7$ to enhance the selectivity of photocatalytic CO_2 reduction with H_2O. *J. Alloys Compd.* **2019**, *786*, 149–154.

[98] Vu, N. N.; Nguyen, C. C.; Kaliaguine, S.; Do, T. O. Reduced Cu/Pt-$HCa_2Ta_3O_{10}$ perovskite nanosheets for sunlight-driven conversion of CO_2 into valuable fuels. *Adv. Sustain. Syst.* **2017**, *1*, 1700048.

[99] Pan, L. K.; Mei, H.; Zhu, G. Q.; Li, S. P.; Xie, X. Q.; Gong, S. W.; Liu, H. X.; Jin, Z. P.; Gao, J. Z.; Cheng, L. F. et al. Bi selectively doped $SrTiO_{3-x}$ nanosheets enhance photocatalytic CO_2 reduction under visible light. *J. Colloid Interface Sci.* **2022**, *611*, 137–148.

[100] Ouyang, T. W.; Fan, W. Y.; Guo, J. Q.; Zheng, Y. N.; Yin, X. H.; Shen, Y. L. DFT study on Ag loaded 2H-MoS_2 for understanding the mechanism of improved photocatalytic reduction of CO_2. *Phys. Chem. Chem. Phys.* **2020**, *22*, 10305–10313.

[101] Xu, F. Y.; Zhu, B. C.; Cheng, B.; Yu, J. G.; Xu, J. 1D/2D TiO_2/MoS_2 hybrid nanostructures for enhanced photocatalytic CO_2 reduction. *Adv. Opt. Mater.* **2018**, *6*, 1800911.

[102] Jia, P. Y.; Guo, R. T.; Pan, W. G.; Huang, C. Y.; Tang, J. Y.; Liu, X. Y.; Qin, H.; Xu, Q. Y. The MoS_2/TiO_2 heterojunction composites with enhanced activity for CO_2 photocatalytic reduction under visible light irradiation. *Colloids Surf. A: Physicochem. Eng. Aspects* **2019**, *570*, 306–316.

[103] Kumari, S.; Gusain, R.; Kumar, A.; Manwar, N.; Jain, S. L.; Khatri, O. P. Direct growth of nanostructural MoS_2 over the h-BN nanoplatelets: An efficient heterostructure for visible light photoreduction of CO_2 to methanol. *J. CO_2 Util.* **2020**, *42*, 101345.

[104] Wang, X. D.; He, J.; Mao, L.; Cai, X. Y.; Sun, C. Z.; Zhu, M. S. $CsPbBr_3$ perovskite nanocrystals anchoring on monolayer MoS_2 nanosheets for efficient photocatalytic CO_2 reduction. *Chem. Eng. J.* **2021**, *416*, 128077.

[105] Zhao, Y. X.; Cai, W.; Shi, Y. P.; Tang, J. Y.; Gong, Y. H.; Chen, M. D.; Zhong, Q. Construction of Nano-Fe_2O_3-decorated flower-like MoS_2 with Fe–S bonds for efficient photoreduction of CO_2 under visible-light irradiation. *ACS Sustain. Chem. Eng.* **2020**, *8*, 12603–12611.

[106] Shown, I.; Samireddi, S.; Chang, Y. C.; Putikam, R.; Chang, P. H.; Sabbah, A.; Fu, F. Y.; Chen, W. F.; Wu, C. I.; Yu, T. Y. et al. Carbon-doped SnS_2 nanostructure as a high-efficiency solar fuel catalyst under visible light. *Nat. Commun.* **2018**, *9*, 169.

[107] She, H. D.; Zhou, H.; Li, L. S.; Zhao, Z. W.; Jiang, M.; Huang, J. W.; Wang, L.; Wang, Q. Z. Construction of a two-dimensional composite derived from TiO_2 and SnS_2 for enhanced photocatalytic reduction of CO_2 into CH_4. *ACS Sustain. Chem. Eng.* **2019**, *7*, 650–659.

[108] Wang, X. D.; Huang, Y. H.; Liao, J. F.; Jiang, Y.; Zhou, L.; Zhang, X. Y.; Chen, H. Y.; Kuang, D. B. *In situ* construction of a Cs_2SnI_6 perovskite nanocrystal/SnS_2 nanosheet heterojunction with boosted interfacial charge transfer. *J. Am. Chem. Soc.* **2019**, *141*, 13434–13441.

[109] Yin, S. K.; Sun, L. L.; Zhou, Y. J.; Li, X.; Li, J. Z.; Song, X. H.; Huo, P. W.; Wang, H. Q.; Yan, Y. S. Enhanced electron–hole separation in SnS_2/Au/g-C_3N_4 embedded structure for efficient CO_2 photoreduction. *Chem. Eng. J.* **2021**, *406*, 126776.

[110] Li, G. H.; Sun, Y. Y.; Sun, S. M.; Chen, W. L.; Zheng, J. C.; Chen, F.; Sun, Z. F.; Sun, W. The effects of morphologies on photoreduction of carbon dioxide to gaseous fuel over tin disulfide under visible light irradiation. *Adv. Powder Technol.* **2020**, *31*, 2505–2512.

[111] Sun, Y. Y.; Li, G. H.; Xu, J.; Sun, Z. F. Visible-light photocatalytic reduction of carbon dioxide over SnS_2. *Mater. Lett.* **2016**, *174*, 238–241.

[112] Qiu, C. H.; Bai, S.; Cao, W. J.; Tan, L.; Liu, J. Y.; Zhao, Y. F.; Song, Y. F. Tunable syngas synthesis from photocatalytic CO_2 reduction under visible-light irradiation by interfacial engineering. *Trans. Tianjin Univ.* **2020**, *26*, 352–361.

[113] Li, J.; Xu, X. H.; Huang, B. B.; Lou, Z. Z.; Li, B. J. Light-induced *in situ* formation of a nonmetallic plasmonic MoS_2/MoO_{3-x} heterostructure with efficient charge transfer for CO_2 reduction and SERS detection. *ACS Appl. Mater. Interfaces* **2021**, *13*, 10047–10053.

[114] Gao, G.; Zhu, Z.; Zheng, J.; Liu, Z.; Wang, Q.; Yan, Y. S. Ultrathin magnetic Mg-Al LDH photocatalyst for enhanced CO_2 reduction: Fabrication and mechanism. *J. Colloid Interface Sci.* **2019**, *555*, 1–10.

[115] Bai, S.; Wang, Z. L.; Tan, L.; Waterhouse, G. I. N.; Zhao, Y. F.; Song, Y. F. 600 nm irradiation-induced efficient photocatalytic CO_2 reduction by ultrathin layered double hydroxide nanosheets. *Ind. Eng. Chem. Res.* **2020**, *59*, 5848–5857.

[116] Zhang, T. T.; Shang, H. S.; Zhang, B.; Yan, D. P.; Xiang, X. Ag/ultrathin-layered double hydroxide nanosheets induced by a self-redox strategy for highly selective CO_2 reduction. *ACS Appl. Mater. Interfaces* **2021**, *13*, 16536–16544.

[117] Wang, K. X.; Miao, C. L.; Liu, Y. N.; Cai, L. Y.; Jones, W.; Fan, J. X.; Li, D. Q.; Feng, J. T. Vacancy enriched ultrathin TiMgAl-layered double hydroxide/graphene oxides composites as highly efficient visible-light catalysts for CO_2 reduction. *Appl. Catal. B: Environ.* **2020**, *270*, 118878.

[118] Wang, X.; Wang, Z. l.; Bai, Y.; Tan, L.; Xu, Y. Q.; Hao, X. J.; Wang, J. K.; Mahadi, A. H.; Zhao, Y. F.; Zheng, L. R. et al. Tuning the selectivity of photoreduction of CO_2 to syngas over Pd/layered double hydroxide nanosheets under visible light up to 600 nm. *J. Energy Chem.* **2020**, *46*, 1–7.

[119] Tan, L.; Xu, S. M.; Wang, Z. L.; Xu, Y. Q.; Wang, X.; Hao, X. J.; Bai, S.; Ning, C. J.; Wang, Y.; Zhang, W. K. et al. Highly selective photoreduction of CO_2 with suppressing H_2 evolution over monolayer layered double hydroxide under irradiation above 600 nm. *Angew. Chem.* **2019**, *131*, 11986–11993.

[120] Bai, S.; Li, T.; Wang, H. J.; Tan, L.; Zhao, Y. F.; Song, Y. F. Scale-up synthesis of monolayer layered double hydroxide nanosheets via separate nucleation and aging steps method for efficient CO_2 photoreduction. *Chem. Eng. J.* **2021**, *419*, 129390.

[121] Hao, X. J.; Tan, L.; Xu, Y. Q.; Wang, Z. L.; Wang, X.; Bai, S.; Ning, C. J.; Zhao, J. W.; Zhao, Y. F.; Song, Y. F. Engineering active Ni sites in ternary layered double hydroxide nanosheets for a highly selective photoreduction of CO_2 to CH_4 under irradiation above 500 nm. *Ind. Eng. Chem. Res.* **2020**, *59*, 3008–3015.

[122] Xiong, X. Y.; Zhao, Y. F.; Shi, R.; Yin, W. J.; Zhao, Y. X.; Waterhouse, G. I. N.; Zhang, T. R. Selective photocatalytic CO_2 reduction over Zn-based layered double hydroxides containing tri or tetravalent metals. *Sci. Bull.* **2020**, *65*, 987–994.

[123] Tan, L.; Peter, K.; Ren, J.; Du, B. Y.; Hao, X. J.; Zhao, Y. F.; Song, Y. F. Photocatalytic syngas synthesis from CO_2 and H_2O using ultrafine CeO_2-decorated layered double hydroxide nanosheets under visible-light up to 600 nm. *Front. Chem. Sci. Eng.* **2020**, *15*, 99–108.

[124] Chen, W. Y.; Han, B.; Xie, Y. L.; Liang, S. J.; Deng, H.; Lin, Z. Ultrathin Co-Co LDHs nanosheets assembled vertically on MXene: 3D nanoarrays for boosted visible-light-driven CO_2 reduction. *Chem. Eng. J.* **2020**, *391*, 123519.

[125] Zhao, S.; Pan, D.; Liang, Q.; Zhou, M.; Yao, C.; Xu, S.; Li, Z. Y. Ultrathin NiAl-layered double hydroxides grown on 2D $Ti_3C_2T_x$

MXene to construct core–shell heterostructures for enhanced photocatalytic CO_2 reduction. *J. Phys. Chem. C* **2021**, *125*, 10207–10218.

[126] Ali Khan, A.; Tahir, M. Construction of an S-scheme heterojunction with oxygen-vacancy-rich trimetallic CoAlLa-LDH anchored on titania-sandwiched Ti_3C_2 multilayers for boosting photocatalytic CO_2 reduction under visible light. *Ind. Eng. Chem. Res.* **2021**, *60*, 16201–16223.

[127] Xu, J.; Liu, X. W.; Zhou, Z. J.; Deng, L. D.; Liu, L.; Xu, M. H. Platinum nanoparticles with low content and high dispersion over exfoliated layered double hydroxide for photocatalytic CO_2 reduction. *Energy Fuels* **2021**, *35*, 10820–10831.

[128] Jo, W. K.; Kumar, S.; Tonda, S. N-doped C dot/CoAl-layered double hydroxide/g-C_3N_4 hybrid composites for efficient and selective solar-driven conversion of CO_2 into CH_4. *Compos. Part B: Eng.* **2019**, *176*, 107212.

[129] Wang, K. F.; Zhang, L.; Su, Y.; Shao, D. K.; Zeng, S. W.; Wang, W. Z. Photoreduction of carbon dioxide of atmospheric concentration to methane with water over CoAl-layered double hydroxide nanosheets. *J. Mater. Chem. A* **2018**, *6*, 8366–8373.

[130] Kipkorir, P.; Tan, L.; Ren, J.; Zhao, Y. F.; Song, Y. F. Intercalation effect in NiAl-layered double hydroxide nanosheets for CO_2 reduction under visible light. *Chem. Res. Chin. Univ.* **2020**, *36*, 127–133.

[131] Ji, X. Y.; Guo, R. T.; Tang, J. Y.; Miao, Y. F.; Lin, Z. D.; Hong, L. F.; Yuan, Y.; Li, Z. S.; Pan, W. P. Construction of full solar-spectrum-driven $Cu_{2-x}S$/Ni-Al-LDH heterostructures for efficient photocatalytic CO_2 reduction. *ACS Appl. Energy Mater.* **2022**, *5*, 2862–2872.

[132] Wu, G.; Shen, H. C.; Li, J. M.; Guo, J. Q.; Yin, X. H.; Mu, M. M. Syntheses of ZnTi-LDH sensitized by tetra(4-carboxyphenyl) porphyrin for accerlating photocatalytic reduction of carbon dioxide. *J. Solid State Chem.* **2022**, *309*, 122955.

[133] Ou, S. Y.; Zhou, M.; Chen, W.; Zhang, Y. Y.; Liu, Y. L. COF-5/CoAl-LDH nanocomposite heterojunction for enhanced visible-light-driven CO_2 reduction. *ChemSusChem* **2022**, *15*, e202200184.

[134] Zhao, X. Y.; Zhao, X. P.; Ullah, I.; Gao, L. N.; Zhang, J. Z.; Lu, J. The *in-situ* growth NiFe-layered double hydroxides/g-C_3N_4 nanocomposite 2D/2D heterojunction for enhanced photocatalytic CO_2 reduction performance. *Catal. Lett.* **2021**, *151*, 1683–1692.

[135] Hu, J. M.; Ding, J.; Zhong, Q. Ultrathin 2D Ti_3C_2 MXene Co-catalyst anchored on porous g-C_3N_4 for enhanced photocatalytic CO_2 reduction under visible-light irradiation. *J. Colloid Interface Sci.* **2021**, *582*, 647–657.

[136] Cao, S. W.; Shen, B. J.; Tong, T.; Fu, J. W.; Yu, J. G. 2D/2D heterojunction of ultrathin MXene/Bi_2WO_6 nanosheets for improved photocatalytic CO_2 reduction. *Adv. Funct. Mater.* **2018**, *28*, 1800136.

[137] Chen, L. Y.; Huang, K. L.; Xie, Q. R.; Lam, S. M.; Sin, J. C.; Su, T. M.; Ji, H. B.; Qin, Z. Z. The enhancement of photocatalytic CO_2 reduction by the *in situ* growth of TiO_2 on Ti_3C_2 MXene. *Catal. Sci. Technol.* **2021**, *11*, 1602–1614.

[138] Yang, Y. L.; Zhang, D. N.; Fan, J. J.; Liao, Y. L.; Xiang, Q. J. Construction of an ultrathin S-scheme heterojunction based on few-layer g-C_3N_4 and monolayer $Ti_3C_2T_x$ MXene for photocatalytic CO_2 reduction. *Sol. RRL* **2021**, *5*, 2000351.

[139] Yang, C.; Tan, Q. Y.; Li, Q.; Zhou, J.; Fan, J. J.; Li, B.; Sun, J.; Lv, K. L. 2D/2D Ti_3C_2 MXene/g-C_3N_4 nanosheets heterojunction for high efficient CO_2 reduction photocatalyst:Dual effects of urea. *Appl. Catal. B: Environ.* **2020**, *268*, 118738.

[140] Wang, H. Q.; Tang, Q. J.; Wu, Z. B. Construction of few-layer Ti_3C_2 MXene and boron-doped g-C_3N_4 for enhanced photocatalytic CO_2 reduction. *ACS Sustain. Chem. Eng.* **2021**, *9*, 8425–8434.

[141] Chen, C.; Hu, J. D.; Yang, X. G.; Yang, T. Y.; Qu, J. F.; Guo, C. X.; Li, C. M. Ambient-stable black phosphorus-based 2D/2D S-scheme heterojunction for efficient photocatalytic CO_2 reduction to syngas. *ACS Appl. Mater. Interfaces* **2021**, *13*, 20162–20173.

[142] Zhou, G. L.; Yang, J. M.; Zhu, X. W.; Li, Q. D.; Yu, Q.; El-Alami, W.; Wang, C. T.; She, Y. B.; Qian, J. C.; Xu, H. et al. Cryo-induced closely bonded heterostructure for effective CO_2 conversion: The case of ultrathin BP nanosheets/ g-C_3N_4. *J. Energy Chem.* **2020**, *49*, 89–95.

[143] Xu, Y. M.; Zhang, W. N.; Zhou, G. F.; Jin, M. L.; Li, X. S. *In-situ* growth of metal phosphide-black phosphorus heterojunction for highly selective and efficient photocatalytic carbon dioxide conversion. *J. Colloid Interface Sci.* **2022**, *616*, 641–648.

[144] Liu, W. B.; Li, X. K.; Wang, C. M.; Pan, H. H.; Liu, W. P.; Wang, K.; Zeng, Q. D.; Wang, R. M.; Jiang, J. Z. A scalable general synthetic approach toward ultrathin imine-linked two-dimensional covalent organic framework nanosheets for photocatalytic CO_2 reduction. *J. Am. Chem. Soc.* **2019**, *141*, 17431–17440.

[145] Yang, S. Z.; Hu, W. H.; Zhang, X.; He, P. L.; Pattengale, B.; Liu, C. M.; Cendejas, M.; Hermans, I.; Zhang, X. Y.; Zhang, J. R. et al. 2D covalent organic frameworks as intrinsic photocatalysts for visible light-driven CO_2 reduction. *J. Am. Chem. Soc.* **2018**, *140*, 14614–14618.

[146] Qamar, S.; Lei, F. C.; Liang, L.; Gao, S.; Liu, K. T.; Sun, Y. F.; Ni, W. X.; Xie, Y. Ultrathin TiO_2 flakes optimizing solar light driven CO_2 reduction. *Nano Energy* **2016**, *26*, 692–698.

[147] Shi, W. N.; Guo, X. W.; Cui, C. X.; Jiang, K.; Li, Z. J.; Qu, L. B.; Wang, J. C. Controllable synthesis of Cu_2O decorated WO_3 nanosheets with dominant (001) facets for photocatalytic CO_2 reduction under visible-light irradiation. *Appl. Catal. B: Environ.* **2019**, *243*, 236–242.

[148] Chen, W. Y.; Han, B.; Tian, C.; Liu, X. M.; Liang, S. J.; Deng, H.; Lin, Z. MOFs-derived ultrathin holey Co_3O_4 nanosheets for enhanced visible light CO_2 reduction. *Appl. Catal. B: Environ.* **2019**, *244*, 996–1003.

[149] Xin, C. Y.; Hu, M. C.; Wang, K.; Wang, X. T. Significant enhancement of photocatalytic reduction of CO_2 with H_2O over ZnO by the formation of basic zinc carbonate. *Langmuir* **2017**, *33*, 6667–6676.

[150] J Jana, P.; de la Peña O'Shea, V. A.; Montero, C. M.; Gálvez, P.; Pizarro, P.; Coronado, J. M.; Serrano, D. P. Mixed $NaNb_xTa_{1-x}O_3$ perovskites as photocatalysts for H_2 production. *Green Chem.* **2015**, *17*, 1735–1743.

[151] You, H. L.; Wu, Z.; Wang, L.; Jia, Y. M.; Li, S.; Zou, J. Highly efficient pyrocatalysis of pyroelectric $NaNbO_3$ shape-controllable nanoparticles for room-temperature dye decomposition. *Chemosphere* **2018**, *199*, 531–537.

[152] Shi, R.; Waterhouse, G. I. N.; Zhang, T. R. Recent progress in photocatalytic CO_2 reduction over perovskite oxides. *Sol. RRL* **2017**, *1*, 1700126.

[153] Xu, X. X.; Wang, X. Perovskite nano-heterojunctions: Synthesis, structures, properties, challenges, and prospects. *Small Struct.* **2020**, *1*, 2000009.

[154] Shao, X.; Xin, W. Y.; Yin, X. H. Hydrothermal synthesis of ZnO quantum dot/KNb_3O_8 nanosheet photocatalysts for reducing carbon dioxide to methanol. *Beilstein J. Nanotechnol.* **2017**, *8*, 2264–2270.

[155] Kumar, D. P.; Rangappa, A. P.; Do, K. H.; Hong, Y.; Gopannagari, M.; Reddy, K. A. J.; Bhavani, P.; Reddy, D. A.; Kim, T. K. Noble metal free few-layered perovskite-based Ba_2NbFeO_6 nanostructures on exfoliated g-C_3N_4 layers as highly efficient catalysts for enhanced solar fuel production. *Appl. Surf. Sci.* **2022**, *572*, 151406.

[156] Mao, L. L.; Ke, W. J.; Pedesseau, L.; Wu, Y. L.; Katan, C.; Even, J.; Wasielewski, M. R.; Stoumpos, C. C.; Kanatzidis, M. G. Hybrid dion-jacobson 2D lead iodide perovskites. *J. Am. Chem. Soc.* **2018**, *140*, 3775–3783.

[157] Chen, W.; Wang, Y. H.; Shangguan, W. Metal (oxide) modified (M = Pd, Ag, Au and Cu) $H_2SrTa_2O_7$ for photocatalytic CO_2 reduction with H_2O: The effect of cocatalysts on promoting activity toward CO and H_2 evolution. *Int. J. Hydrogen Energy* **2019**, *44*, 4123–4132.

[158] Iizuka, K.; Wato, T.; Miseki, Y.; Saito, K.; Kudo, A. Photocatalytic reduction of carbon dioxide over Ag cocatalyst-loaded $ALa_4Ti_4O_{15}$ (A = Ca, Sr, and Ba) using water as a reducing reagent. *J. Am. Chem. Soc.* **2011**, *133*, 20863–20868.

[159] Wang, Z.; Teramura, K.; Hosokawa, S.; Tanaka, T. Photocatalytic conversion of CO_2 in water over Ag-modified $La_2Ti_2O_7$. *Appl. Catal. B: Environ.* **2015**, *163*, 241–247.

[160] Qu, Y. J.; Kwok, C. T.; Shao, Y. F.; Shi, X. Q.; Kawazoe, Y.; Pan,

H. Pentagonal transition-metal (group X) chalcogenide monolayers: Intrinsic semiconductors for photocatalysis. *Int. J. Hydrogen Energy* **2021**, *46*, 9371–9379.

[161] Lin, J. H.; Zhang, Y. Y.; Zhou, W.; Pantelides, S. T. Structural flexibility and alloying in ultrathin transition-metal chalcogenide nanowires. *ACS Nano* **2016**, *10*, 2782–2790.

[162] Choudhary, N.; Islam, A.; Kim, J. H.; Ko, T. J.; Schropp, A.; Hurtado, L.; Weitzman, D.; Zhai, L.; Jung, Y. Two-dimensional transition metal dichalcogenide hybrid materials for energy applications. *Nano Today* **2018**, *19*, 16–40.

[163] Wu, J. J.; Lee, G. J. Advanced nanomaterials for water splitting and hydrogen generation. In *Nanomaterials for Green Energy*; Bhanvase, B. A.; Pawade, V. B.; Dhoble, S. J.; Sonawane, S. H.; Ashokkumar, M., Eds.; Elsevier: Amsterdam, 2018; pp 145–167.

[164] Hasani, A.; Tekalgne, M.; Van Le, Q.; Jang, H. W.; Kim, S. Y. Two-dimensional materials as catalysts for solar fuels: Hydrogen evolution reaction and CO_2 reduction. *J. Mater. Chem. A* **2019**, *7*, 430–454.

[165] Liu, R.; Wang, F. K.; Liu, L. X.; He, X. Y.; Chen, J. Z.; Li, Y.; Zhai, T. Y. Band alignment engineering in two-dimensional transition metal dichalcogenide-based heterostructures for photodetectors. *Small Struct.* **2021**, *2*, 2000136.

[166] Zhang, Z. F.; Qian, Q. K.; Li, B. K.; Chen, K. J. Interface engineering of monolayer MoS_2/GaN hybrid heterostructure: Modified band alignment for photocatalytic water splitting application by nitridation treatment. *ACS Appl. Mater. Interfaces* **2018**, *10*, 17419–17426.

[167] Chu, H. P.; Lei, W. Y.; Liu, X. J.; Li, J. L.; Zheng, W.; Zhu, G.; Li, C.; Pan, L. K.; Sun, C. Q. Synergetic effect of TiO_2 as co-catalyst for enhanced visible light photocatalytic reduction of Cr(VI) on $MoSe_2$. *Appl. Catal. A: Gen.* **2016**, *521*, 19–25.

[168] Sun, S. M.; Li, X. M.; Wang, W. Z.; Zhang, L.; Sun, X. Photocatalytic robust solar energy reduction of dinitrogen to ammonia on ultrathin MoS_2. *Appl. Catal. B* **2017**, *200*, 323–329.

[169] Wang, J. J.; Lin, S.; Tian, N.; Ma, T. Y.; Zhang, Y. H.; Huang, H. W. Nanostructured metal sulfides: Classification, modification strategy, and solar-driven CO_2 reduction application. *Adv. Funct. Mater.* **2021**, *31*, 2008008.

[170] Khan, B.; Raziq, F.; Faheem, M. B.; Farooq, M. U.; Hussain, S.; Ali, F.; Ullah, A.; Mavlonov, A.; Zhao, Y.; Liu, Z. R. et al. Electronic and nanostructure engineering of bifunctional MoS_2 towards exceptional visible-light photocatalytic CO_2 reduction and pollutant degradation. *J. Hazard. Mater.* **2020**, *381*, 120972.

[171] Tu, W. G.; Li, Y. C.; Kuai, L. B.; Zhou, Y.; Xu, Q. F.; Li, H. J.; Wang, X. Y.; Xiao, M.; Zou, Z. G. Construction of unique two-dimensional MoS_2-TiO_2 hybrid nanojunctions: MoS_2 as a promising cost-effective cocatalyst toward improved photocatalytic reduction of CO_2 to methanol. *Nanoscale* **2017**, *9*, 9065–9070.

[172] Zhang, R.; Jian, W.; Yang, Z. D.; Bai, F. Q. Insights into the photocatalytic mechanism of the C_4N/MoS_2 heterostructure: A first-principle study. *Chin. Chem. Lett.* **2020**, *31*, 2319–2324.

[173] Dai, W. L.; Yu, J. J.; Luo, S. L.; Hu, X.; Yang, L. X.; Zhang, S. Q.; Li, B.; Luo, X. B.; Zou, J. P. WS_2 quantum dots seeding in Bi_2S_3 nanotubes:A novel Vis-NIR light sensitive photocatalyst with low-resistance junction interface for CO_2 reduction. *Chem. Eng. J.* **2020**, *389*, 123430.

[174] Wang, Q.; O'Hare, D. Recent advances in the synthesis and application of layered double hydroxide (LDH) nanosheets. *Chem. Rev.* **2012**, *112*, 4124–4155.

[175] Arif, M.; Yasin, G.; Luo, L.; Ye, W.; Mushtaq, M. A.; Fang, X. Y.; Xiang, X.; Ji, S. F.; Yan, D. P. Hierarchical hollow nanotubes of NiFeV-layered double hydroxides@CoVP heterostructures towards efficient, pH-universal electrocatalytical nitrogen reduction reaction to ammonia. *Appl. Catal. B: Environ.* **2020**, *265*, 118559.

[176] Arif, M.; Yasin, G.; Shakeel, M.; Mushtaq, M. A.; Ye, W.; Fang, X. Y.; Ji, S. F.; Yan, D. P. Hierarchical CoFe-layered double hydroxide and g-C_3N_4 heterostructures with enhanced bifunctional photo/electrocatalytic activity towards overall water splitting. *Mater. Chem. Front.* **2019**, *3*, 520–531.

[177] Mohapatra, L.; Parida, K. A review on the recent progress, challenges and perspective of layered double hydroxides as promising photocatalysts. *J. Mater. Chem. A* **2016**, *4*, 10744–10766.

[178] Zhao, Y. F.; Jia, X. D.; Waterhouse, G. I. N.; Wu, L. Z.; Tung, C. H.; O'Hare, D.; Zhang, T. R. Layered double hydroxide nanostructured photocatalysts for renewable energy production. *Adv. Energy Mater.* **2016**, *6*, 1501974.

[179] Cui, X. F.; Wang, J.; Liu, B.; Ling, S.; Long, R.; Xiong, Y. J. Turning Au nanoclusters catalytically active for visible-light-driven CO_2 reduction through bridging ligands. *J. Am. Chem. Soc.* **2018**, *140*, 16514–16520.

[180] Zhong, Q.; Li, Y.; Zhang, G. K. Two-dimensional MXene-based and MXene-derived photocatalysts: Recent developments and perspectives. *Chem. Eng. J.* **2021**, *409*, 128099.

[181] Huang, P. F.; Zhang, S. L.; Ying, H. J.; Zhang, Z.; Han, W. Q. Few-layered Ti_3C_2 MXene anchoring bimetallic selenide $NiCo_2Se_4$ nanoparticles for superior Sodium-ion batteries. *Chem. Eng. J.* **2021**, *417*, 129161.

[182] Cai, C. Y.; Zhou, W. B.; Fu, Y. Bioinspired MXene nacre with mechanical robustness for highly flexible all-solid-state photothermo-supercapacitor. *Chem. Eng. J.* **2021**, *418*, 129275.

[183] Li, X. L.; Zhu, J. F.; Liang, W. Y.; Zhitomirsky, I. MXene ($Ti_3C_2T_x$) anodes for asymmetric supercapacitors with high active mass loading. *Mater. Chem. Phys.* **2021**, *268*, 124748.

[184] Shi, Q. R.; Zhang, X. Y.; Yang, Y.; Huang, J. J.; Fu, X. L.; Wang, T. Y.; Liu, X. D.; Sun, A. W.; Ge, J. H.; Shen, J. Y. et al. 3D hierarchical architecture collaborating with 2D/2D interface interaction in NiAl-LDH/Ti_3C_2 nanocomposite for efficient and selective photoconversion of CO_2. *J. Energy Chem.* **2021**, *59*, 9–18.

[185] Que, M. D.; Cai, W. H.; Zhao, Y.; Yang, Y. W.; Zhang, B. Y.; Yun, S.; Chen, J.; Zhu, G. 2D/2D schottky heterojunction of *in-situ* growth $FAPbBr_3$/Ti_3C_2 composites for enhancing photocatalytic CO_2 reduction. *J. Colloid. Interface Sci.* **2022**, *610*, 538–545.

[186] Zhang, J. Z.; Shi, J. J.; Tao, S.; Wu, L.; Lu, J. Cu_2O/Ti_3C_2 MXene heterojunction photocatalysts for improved CO_2 photocatalytic reduction performance. *Appl. Surf. Sci.* **2021**, *542*, 148685.

[187] Baboukani, A. R.; Khakpour, I.; Drozd, V.; Wang, C. L. Liquid-based exfoliation of black phosphorus into phosphorene and its application for energy storage devices. *Small Struct.* **2021**, *2*, 2000148.

[188] He, Z. Z.; Goulas, J.; Parker, E.; Sun, Y. Q.; Zhou, X. D.; Fei, L. Review on covalent organic frameworks and derivatives for electrochemical and photocatalytic CO_2 reduction. *Catal. Today*, in press, https://doi.org/10.1016/j.cattod.2022.04.021.

[189] Xu, N. F.; Diao, Y. X.; Qin, X. H.; Xu, Z. T.; Ke, H. Z.; Zhu, X. J. Donor–acceptor covalent organic frameworks of nickel(II) porphyrin for selective and efficient CO_2 reduction into CO. *Dalton Trans.* **2020**, *49*, 15587–15591.

[190] Wang, S. Z.; Xu, X. Y.; Yue, Y.; Yu, K. S.; Shui, Q. J.; Huang, N.; Chen, H. Z. Semiconductive covalent organic frameworks: Structural design, synthesis, and application. *Small Struct.* **2020**, *1*, 2000021.

[191] Wang, S. B.; Han, X.; Zhang, Y. H.; Tian, N.; Ma, T. Y.; Huang, H. W. Inside-and-out semiconductor engineering for CO_2 photoreduction: From recent advances to new trends. *Small Struct.* **2021**, *2*, 2000061.

[192] Zhao, Y. X.; Zhang, S.; Shi, R.; Waterhouse, G. I. N.; Tang, J. W.; Zhang, T. R. Two-dimensional photocatalyst design: A critical review of recent experimental and computational advances. *Mater. Today* **2020**, *34*, 78–91.

[193] Chen, S. C.; Wang, H.; Kang, Z. X.; Jin, S.; Zhang, X. D.; Zheng, X. S.; Qi, Z. M.; Zhu, J. F.; Pan, B. C.; Xie, Y. Oxygen vacancy associated single-electron transfer for photofixation of CO_2 to long-chain chemicals. *Nat. Commun.* **2019**, *10*, 788.

[194] Yu, H. J.; Chen, F.; Li, X. W.; Huang, H. W.; Zhang, Q. Y.; Su, S. Q.; Wang, K. Y.; Mao, E. Y.; Mei, B.; Mul, G. et al. Synergy of ferroelectric polarization and oxygen vacancy to promote CO_2 photoreduction. *Nat. Commun.* **2021**, *12*, 4594.